ABSTRACT

Title of dissertation: MAGNETIC AND ACOUSTIC INVESTIGATIONS OF TURBULENT SPHERICAL COUETTE FLOW

Matthew M. Adams, Doctor of Philosophy, 2016

Dissertation directed by: Professor Daniel Lathrop
Department of Physics

This dissertation describes experiments in spherical Couette devices, using both gas and liquid sodium. The experimental geometry is motivated by the Earth's outer core, the seat of the geodynamo, and consists of an outer spherical shell and an inner sphere, both of which can be rotated independently to drive a shear flow in the fluid lying between them. In the case of experiments with liquid sodium, we apply DC axial magnetic fields, with a dominant dipole or quadrupole component, to the system. We measure the magnetic field induced by the flow of liquid sodium using an external array of Hall effect magnetic field probes, as well as two probes inserted into the fluid volume. This gives information about possible velocity patterns present, and we extend previous work categorizing flow states, noting further information that can be extracted from the induced field measurements. The limitations due to a lack of direct velocity measurements prompted us to work on developing the technique of using acoustic modes to measure zonal flows. Using gas as the working fluid in our 60 cm diameter spherical Couette experiment, we identified

acoustic modes of the container, and obtained excellent agreement with theoretical predictions. For the case of uniform rotation of the system, we compared the acoustic mode frequency splittings with theoretical predictions for solid body flow, and obtained excellent agreement. This gave us confidence in extending this work to the case of differential rotation, with a turbulent flow state. Using the measured splittings for this case, our colleagues performed an inversion to infer the pattern of zonal velocities within the flow, the first such inversion in a rotating laboratory experiment. This technique holds promise for use in liquid sodium experiments, for which zonal flow measurements have historically been challenging.

MAGNETIC AND ACOUSTIC INVESTIGATIONS OF TURBULENT SPHERICAL COUETTE FLOW

by

Matthew Michael Adams

Dissertation submitted to the Faculty of the Graduate School of the
University of Maryland, College Park in partial fulfillment
of the requirements for the degree of
Doctor of Philosophy
2016

Advisory Committee:
Professor Daniel P. Lathrop, Chair/Advisor
Professor Thomas M. Antonsen
Professor James F. Drake
Professor James H. Duncan
Professor Vedran Lekic

© Copyright by
Matthew Michael Adams
2016

Dedication

To my family

Acknowledgments

First and foremost I must acknowledge my advisor, Dan Lathrop, and the lab mates past and present with whom I have had the pleasure and privilege of working, including Nolan Balew, Barbara Brawn-Cinani, Minh Doan, Enrico Fonda, Kristy (née Gaff) Johnson, Onur Kara, Chirag Kalelkar, Doug Kelley, Qin Liu, Don Martin, Peter Megson, David Meichle, Myung Park, Matt Paoletti, Ruben Rojas, Cecilia Rorai, Daniel Serrano, Itamar Shani, Doug Stone, Santiago Triana, and Dan "Axl" Zimmerman. In particular, Doug Kelley, Axl, and Santiago were academic big brothers for me. Doug taught me how to run my experiment, the so-called 60 cm device, and has been generous with his time in answering various questions that popped up even after he had gone on to other positions. Axl has helped me innumerable times with electronics and in troubleshooting various experimental problems, both with the 60 cm experiment, and later with the experiment he helped design and build, the 3 m device. I consulted with him often after he had left the lab as well. Santiago helped me with control systems, coding, and some of my later work on acoustics. Don Martin has been a great resource for all things mechnanical (and safety!) related. Nolan Balew has cheerfully helped me with various machine shop and experiment-wrangling tasks. Daniel Serrano helped with various writing tasks, including editing this manuscript. I'd also like to thank Thomas Antonsen, James Drake, and James Duncan, who served on my dissertation committee. Dan Lathrop has provided me with great scientific guidance over the years, from experiment troubleshooting to data analysis to talk preparation, in addition to funding and

support. His love of science and of brainstorming experiments is infectious, and I'm grateful that I've gotten to be a part of his crew.

The magnetic data presented in this thesis was all done in collaboration with Doug Stone and Minh Doan. It was a pleasure running the 3 m experiment with Doug and Minh. Doug has also been generous in helping me with writing and talk preparation, and letting me bounce ideas off him. Minh designed and built an experimental apparatus used in obtaining some of the data presented in this thesis. The work on acoustics presented in this thesis was done in collaboration with seismologist Ved Lekic and his master's student Anthony Mautino. Collaborating with them has been a pleasure, and I've learned a lot over the course of our work. I must also acknowledge our colleague Henri-Claude Nataf, who invited me to visit his lab in Grenoble, France, and who has been an invaluable help over the years as part of our "extended lab".

I am deeply grateful for the loving support of my family, both during my graduate career, and in all the years leading up to it. In particular my parents have always supported my academic work and my interest in science. When I was young my mom encouraged my curiosity about the world, trying to answer my endless series of questions, and if she didn't know the answer or didn't have time to answer at that moment, assuring me that it was good to be asking these questions. My father has engaged with me in fun, rambling talks on various science topics over the years. My sisters Emily and Paige have also been a great support over the years.

I have also received lots of help from the wider IREAP community. On the administrative side, Dottie Brosius has provided lots of assistance over the years,

including providing the LaTeXtemplate for this manuscript. Nancy Boone provided incredibly fast and responsive purchase order services, helping to keep the lab running smoothly. In the machine shop, another crucial resource in my graduate career, J. Pyle and then Bill Schuster were always at the ready with advice, tools, and assistance in getting things made. Nolan Balew has provided invaluable assistance as well, and Stephen Henderson has shared many machining tips and tricks with me over the years. John Rodgers has provided invaluable electronics advice, as well as most helpful equipment loans. Ed Condon has helped keep my laptops behaving, in addition to helping to troubleshoot, and replace as needed, computer hardware installed on our experiments.

I am grateful for the financial support of the National Science Foundation. Finally, I give thanks to God for the opportunity to learn and work at a great place like the Lathrop lab and the University of Maryland.

Table of Contents

List of Tables viii

List of Figures ix

List of Abbreviations xi

1 Introduction 1
- 1.1 Motivation and Review . . . 5
  - 1.1.1 Geophysics . . . 5
  - 1.1.2 Astrophysics . . . 11
  - 1.1.3 Helioseismology . . . 14
- 1.2 Contribution of the Author . . . 19

2 Theoretical Background and Review of Past Work 21
- 2.1 Hydrodynamics . . . 22
  - 2.1.1 Equations of Motion . . . 22
  - 2.1.2 Dimensionless Parameters: Hydrodynamics . . . 26
  - 2.1.3 Past Work: Theory and Simulations . . . 32
  - 2.1.4 Past Work: Experiments . . . 35
- 2.2 Hydromagnetics . . . 38
  - 2.2.1 Equations of Motion . . . 39
  - 2.2.2 Dimensionless Parameters: Hydromagnetics . . . 42
  - 2.2.3 Past Work: Theory and Simulations . . . 47
  - 2.2.4 Past Work: Magnetized Spherical Couette Flow and Dynamo Experiments . . . 53
- 2.3 Analysis Background . . . 66
  - 2.3.1 Spherical Harmonics . . . 66
  - 2.3.2 Acoustic Modes of Full Sphere and Spherical Shell . . . 72
  - 2.3.3 Acoustic Velocimetry . . . 76
  - 2.3.4 Previous Laboratory Results . . . 78

3 Experimental Apparatus 80
3.1 The 60 cm Experiment . . . 81
3.1.1 Overview . . . 81
3.1.2 Mechanical Set-up . . . 81
3.1.3 Acoustic Instrumentation . . . 84
3.2 The 3 m Experiments . . . 89
3.2.1 Mechanical Set-up . . . 89
3.2.2 Magnets . . . 94
3.2.3 Torque Measurements . . . 94
3.2.4 Magnetic Measurements . . . 95
3.2.5 Gauss Coefficient Projection and Selection Rules . . . 96
3.2.6 Pressure Measurements . . . 98

4 Magnetic Studies 101
4.1 Overview of Results in the 3 m Experiment . . . 101
4.2 Inferred Velocity Patterns . . . 103
4.3 Characterization of States at different Ro . . . 109
4.4 Internal Field Measurements . . . 114

5 Acoustic Studies 132
5.1 Computed Modes . . . 132
5.2 Observed Modes: Stationary Case . . . 134
5.3 Observed Modes: Solid Body Rotation . . . 142
5.4 Observed Modes: Differential Rotation . . . 144
5.5 Inversions and Implications . . . 145
5.6 Prospects for Acoustics in the 3 m Liquid Sodium Experiment . . . 156

6 Conclusions and Future Directions 166
6.1 Magnetic Results . . . 166
6.2 Acoustic Results . . . 167
6.3 Future Directions . . . 167

A Mechanical Drawings 172

Bibliography 177

List of Tables

2.1 Categories of Differential Equations 26
2.2 Sound Speeds 29
2.3 Dimensionless Parameters 46

3.1 Microphone Positions 85
3.2 Speaker Positions 85
3.3 Hall Probe Locations 97
3.4 Selection Rules 99

4.1 Selection Rules Relevant for 3 m Experiment 104
4.2 Experimentally Measured Induced Large Magnetic Fields in 3 m for Various *Ro* 111
4.3 Spectral Peaks of Gauss Coefficients in 3 m for Various Positive *Ro* . 127
4.4 Spectral Peaks of Gauss Coefficients in 3 m for Various Negative *Ro* . 128

5.1 Identified Acoustic Modes 138
5.2 Solid Body Rotation: Comparison of Predictions and Observations . . 144
5.3 Acoustic Modes used in Inversions 154
5.4 Quality Factors of Acoustic Modes 162

List of Figures

1.1 Diagram of Spherical Couette Flow 6

2.1 General circulation patterns for spherical Couette flow 33

3.1 Sketch of 60 cm Set-up 83
3.2 Sketch of 60 cm Rotating Instrumentation 86
3.3 60 cm Microphone Circuit 87
3.4 Photo of 60 cm Acoustic Set-up 88
3.5 60 cm Speaker Circuit 88
3.6 Rendering of 3 m Experiment 91
3.7 Schematic and Photos of the 3 m Experiment 92
3.8 Instrumentation for 3 m Experiment 93

4.1 Normalized Torque vs. Ro^{-1} in 3 m Experiment 102
4.2 Gauss Coefficient Field Pattern Illustrations 105
4.3 Internal Field Measurements from 3 m: ω Effect 108
4.4 Average Power of Spin-Over Mode vs. Ro 110
4.5 PSD of S_1^0 induced magnetic field: Dipole Applied Field 115
4.6 PSD of S_1^1 induced magnetic field: Dipole Applied Field 116
4.7 PSD of S_2^1 induced magnetic field: Dipole Applied Field 117
4.8 PSD of S_3^0 induced magnetic field: Dipole Applied Field 118
4.9 PSD of S_3^1 induced magnetic field: Dipole Applied Field 119
4.10 PSD of S_1^0 induced magnetic field: Quadrupole Applied Field 120
4.11 PSD of S_1^1 induced magnetic field: Quadrupole Applied Field 121
4.12 PSD of S_2^2 induced magnetic field: Quadrupole Applied Field 122
4.13 PSD of Main Induced Magnetic Fields: $Ro = -1$, Dipole Applied Field 123
4.14 PSD of Main Induced Magnetic Fields: $Ro = -1$, Quadrupole Applied Field 124
4.15 PSD of Main Induced Magnetic Fields: $Ro = -2$, Dipole Applied Field 125
4.16 PSD of Main Induced Magnetic Fields: $Ro = -2$, Quadrupole Applied Field 126
4.17 PSD of Internal Azimuthal Field for Various Ro 130
4.18 PSD of Internal Cylindrical Radial Field for Various Ro 131

5.1 Pressure Pattern of (2,3,2) Acoustic Mode 134
5.2 Kernel of (2,3,2) Acoustic Mode 135
5.3 Stationary Acoustic Data: $(0, 3, m)$ Modes 139
5.4 Stationary Acoustic Data: $(0, 4, m)$ Modes 140
5.5 Peaks of $(0, 1, m)$ Modes vs. Ro 146
5.6 Peak of $(1, 0, 0)$ vs. Ro 147
5.7 Peaks of $(0, 4, 0)$ and $(1, 1, 0)$ vs. Ro 148
5.8 Time Variation of Splitting of $(0, 1, 1)$ Mode 149
5.9 Acoustic Spectra for I=-24Hz, O=6Hz 150
5.10 Zoomed Acoustic Spectra for I=-24Hz, O=6Hz 151
5.11 Spectrogram of Selected Modes for I<0Hz, O=6Hz 152
5.12 Spectrogram of Selected Modes for I>0Hz, O=6Hz 153
5.13 Inversion of Acoustic Mode Splittings for Zonal Flow: f_i=-4Hz 155
5.14 Fit of Inversion for Zonal Flow: f_i=-4Hz 156
5.15 Inversion of Acoustic Mode Splittings for Zonal Flow: f_i=-22Hz . . . 157
5.16 Fit of Inversion Splittings for Zonal Flow: f_i=-22Hz 158
5.17 3 m Pressure Spectra: No Chirp 163
5.18 3 m Pressure Spectra: Inner-Only Rotation 164
5.19 3 m Pressure Spectra: Inner-Only Rotation (Zoomed View) 165

List of Abbreviations

b	spherical harmonic normalization radius, radius of outer spherical boundary
B_0	applied, external magnetic field
c	speed of sound
DTS	Derviche Tourneur Sodium experiment (located in Grenoble, France)
E	Ekman number
$\mathbf{E}$	electric field
EMF	Electromotive force
g_l^{mc}, g_l^{ms}	Gauss coefficients
k	wavenumber
K_{nlm}	acoustic mode sensitivity kernel
l	spherical harmonic degree
L	characteristic length scale
m	spherical harmonic order; equivalently, azimuthal wavenumber
MAC	Magnetic Archimedes Coriolis (waves)
MDE	Madison Dynamo Experiment
n	acoustic mode radial node number
p	pressure
P	reduced pressure (includes centrifugal force)
$P_l^m(\cos\theta)$	Schmidt semi-normalized Legendre functions
Pm	magnetic Prandtl number
r	radial spherical coordinate; see θ and ϕ
r_i	inner sphere radius
r_o	outer spherical boundary radius (same as b)
$\mathbf{r}$	coordinate vector
Re	Reynolds number
Rm	magnetic Reynolds number
Ro	Rossby number
S	Lundquist number
$\mathbf{s}_l^{mc}, \mathbf{s}_l^{ms}$	poloidal vector spherical harmonics (velocity field)
$\mathbf{S}_l^{mc}, \mathbf{S}_l^{ms}$	poloidal vector spherical harmonics (magnetic field)
$\mathbf{s}_\alpha, \mathbf{t}_\alpha$	vector spherical harmonic components of the velocity field
$\mathbf{S}_\beta, \mathbf{T}_\beta$	vector spherical harmonic components of the applied magnetic field
$\mathbf{S}_\gamma, \mathbf{T}_\gamma$	vector spherical harmonic components of the induced magnetic field
t	time

$\mathbf{T}_l^{mc}, \mathbf{T}_l^{ms}$	toroidal vector spherical harmonics
$\mathbf{u}$	velocity field
U	characteristic velocity scale
UDV	ultrasound Doppler velocimetry
VKS	Von Karman Sodium (experiment)
$Y_l^{mc}(\theta, \phi)$, $Y_l^{ms}(\theta, \phi)$	scalar spherical harmonics
Γ	radius ratio
η	magnetic diffusivity
θ	colatitude (polar spherical coordinate); see r and ϕ
μ	dynamic viscosity or magnetic permeability
μ_0	magnetic permeability of free space
ν	kinematic viscosity
ρ	density
σ	electrical conductivity
ϕ	azimuthal angle in spherical coordinates; see r and θ
Φ	scalar magnetic potential
ω_{nlm}	acoustic mode frequency
Ω_i	rotation rate of inner sphere
Ω_o	rotation rate of outer spherical shell
$\Omega(r, \theta)$	zonal (azimuthal) flow profile
$\mathbf{\Omega}$	rotation vector of rotating frame (measured in inertial frame)

Chapter 1: Introduction

Large-scale magnetic fields are common in the universe, and are found in planets, stars, accretion disks, and galaxies.[1] Many of these fields are thought to be the result of self-sustaining dynamo action, whereby motions of a conductive fluid in the presence of a magnetic field give rise to induced currents that in turn generate magnetic fields that reinforce the original field [1, 2]. Starting from an arbitrarily small field, the flow of a conductive fluid, driven by some energy source, can result in a persistent large-scale magnetic field that can also show a variety of dynamical changes including polarity reversals. In our own solar system, the Sun, a majority of the planets (Mercury, Earth, Jupiter, Saturn, Uranus, Neptune [2]), and at least some moons (e.g. the Jovian moon Ganymede [3]) exhibit dynamos, while Earth's Moon [4] and Mars [5] show signs of past dynamo action. Farther out, most stars generally have magnetic fields that are thought to arise via dynamo action, and the galaxy itself has a magnetic field that may also be the result of this mechanism [2].

The prevalence of such large-scale fields implies that this mechanism of dynamo action is robust, generally having three ingredients: a large volume of conductive fluid, an energy source to drive the dynamo, and overall rotation to help organize

[1] Much of the material of this chapter, as well as some of the material in chapter 2, originally appeared in Adams, Matthew M., et al. "Liquid sodium models of the Earth's core.", *Progress in Earth and Planetary Science* 2.1, (2015):1.

the flow [6]. The first requirement can be fulfilled by the large liquid metal cores of planets, including Earth with its liquid iron outer core, and Jupiter with its liquid metallic hydrogen core, as well as its moon Ganymede [7], by the plasma found in stars including the Sun, and by conductive aqueous solutions, such as those found in Uranus and Neptune [2]. The second requirement, needed to sustain the magnetic fields against the inevitable Ohmic dissipation resulting from the finite conductivity of the fluid, can be met by a variety of sources, including convection driven by thermal or compositional gradients, as well as precessional and tidal forcings in planetary bodies. The third ingredient, rotation, while not necessary in all cases, is often helpful in organizing the feedback between the flow and the magnetic field. Given that the conservation of angular momentum results in most stars and planetary bodies having a significant amount of overall rotation, rotational effects will often be present even if they are not required for the dynamos to operate [6]. Also, a paradigm of dynamo action is the so-called "stretch-twist-fold" mechanism. In this picture, the flow first stretches a loop of magnetic field, and then twists it and folds it back on itself, thus reinforcing it, first presented in [8] as a dynamo mechanism. System rotation can be one of the ingredients giving the flow field a topology that leads to something like the "stretch-twist-fold" mechanism. In addition, for rapidly rotating systems such as planetary bodies, the interaction of magnetic fields with convection can result in the possibility of distinct weak- and strong-field regimes [2], possibly of relevance to the dynamics of the geodynamo and of other planetary dynamos.

While nature apparently has no problem generating dynamos (with some no-

table exceptions, like Venus, which is discussed below in section 1.1.1), they have proven more elusive in laboratory settings. Thus far, all fluid dynamos realized in a lab have either involved imposing a specific flow pattern via an arrangement of pipes and baffles (as in the experiments in Riga [9–11] and Karlsruhe [12]) or have had ferromagnetic boundaries as a necessary ingredient (as in the von Kármán sodium (VKS) experiment [13, 14]. Significant research in numerical dynamos has been performed, including simulations of the geodynamo that exhibit a dipolar structure and occasional polarity reversals [15, 16], but these geodynamo simulations use one or more unrealistic diffusive parameters in modeling planetary or stellar dynamos.

Both the computational and the experimental difficulties in modeling an Earth-like (or other planetary or stellar) dynamo can be understood in terms of dimensionless parameters. Such parameters are generally constructed by making non-dimensional the applicable equations of motion, such as the Navier-Stokes equation (see sections 2.1.1 and 2.2.1 below). They may be understood as quantifying the relative importance or strength of various forces. Very large or very small dimensionless parameters indicate that a wide range of length and time scales may be important. A particularly noteworthy example of this is turbulence, whereby a fluid exhibits complicated dynamics on a wide range of length and time scales, which must all be resolved if the flow is to be directly simulated by numerical computations. Similarly, for an experimental device to be a good analog of a planetary core, it must match as many of the relevant dimensionless parameters as possible. Both simulations and laboratory experiments have intrinsic limitations that prevent them from achieving some of the relevant dimensionless parameters (see Table 2.2.2 below).

Although both simulations and experiments fall short of the parameter regimes found in planetary and stellar dynamos, experiments can get closer than simulations in certain cases. In particular, turbulent flows are readily achieved in the laboratory that are not amenable to direct numerical simulations. On the other hand, simulations have the advantage of having measurement access to all properties of a fluid flow, unlike experiments which are generally constrained to a limited number of local measurements and perhaps a few global measurements. Simulations can also arbitrarily vary material properties, where again experiments are limited by the available working fluids. Thus, dynamo studies can be furthered through a combination of observational, experimental, and computational efforts.

In this thesis we detail experiments designed and built to address some of the challenges in understanding the interaction of turbulent flow with magnetic fields, and the possibility of dynamo action. In addition we describe efforts to implement acoustic modal velocimetry, a laboratory application of the technique developed for helioseismology, in laboratory experiments using air, and the prospects for implementing this in liquid sodium devices. In the laboratory we use so-called spherical Couette devices, consisting of an outer spherical shell and an inner sphere that share an axis but can be rotated independently to drive a shear flow in the working fluid between them (see diagram in Figure 1.1). This experimental work can also be of use in guiding and benchmarking simulations. In the rest of this chapter, we review some of the observations and relevant natural science that provides a motivation for the experiments, and for the technique of acoustic modal velocimetry. Then, in Chapter 2, we provide the necessary theoretical background in fluid dynamics,

hydromagnetics and dynamo theory, and helioseismology, as well as a review of past work (theoretical, numerical, and experimental) in these areas. In Chapter 3 we provide information about the experimental apparatus and instrumentation used. In Chapter 4 we discuss the results of hydromagnetic experiments, primarily those performed in rotating 3 m diameter spherical shell experiment, the so-called 3 m experiment. In Chapter 5 we discuss the results of acoustic experiments, primarily in another, 60 cm diameter spherical shell experiment, but also including information about the status of acoustic experiments in the 3 m experiment. Finally, in Chapter 6 we discuss some conclusions and indicate possible directions

1.1 Motivation and Review

While the geomagnetic field is the specific inspiration for the experiments described here, ultimately the motivation for this work is a greater understanding of the natural world. The study of conducting fluids combines aspects of fluid dynamics and electromagnetism, and such fluids are ubiquitous in the universe. In the following sections we discuss some of these natural phenomena and how they inform the experimental design.

1.1.1 Geophysics

Closest to home, the Earth's magnetic field is generated by the turbulent flow of liquid iron in Earth's outer core. The geometry of both the 3 m and the 60 cm experiments is based on that of the core of the Earth, with the outer shell

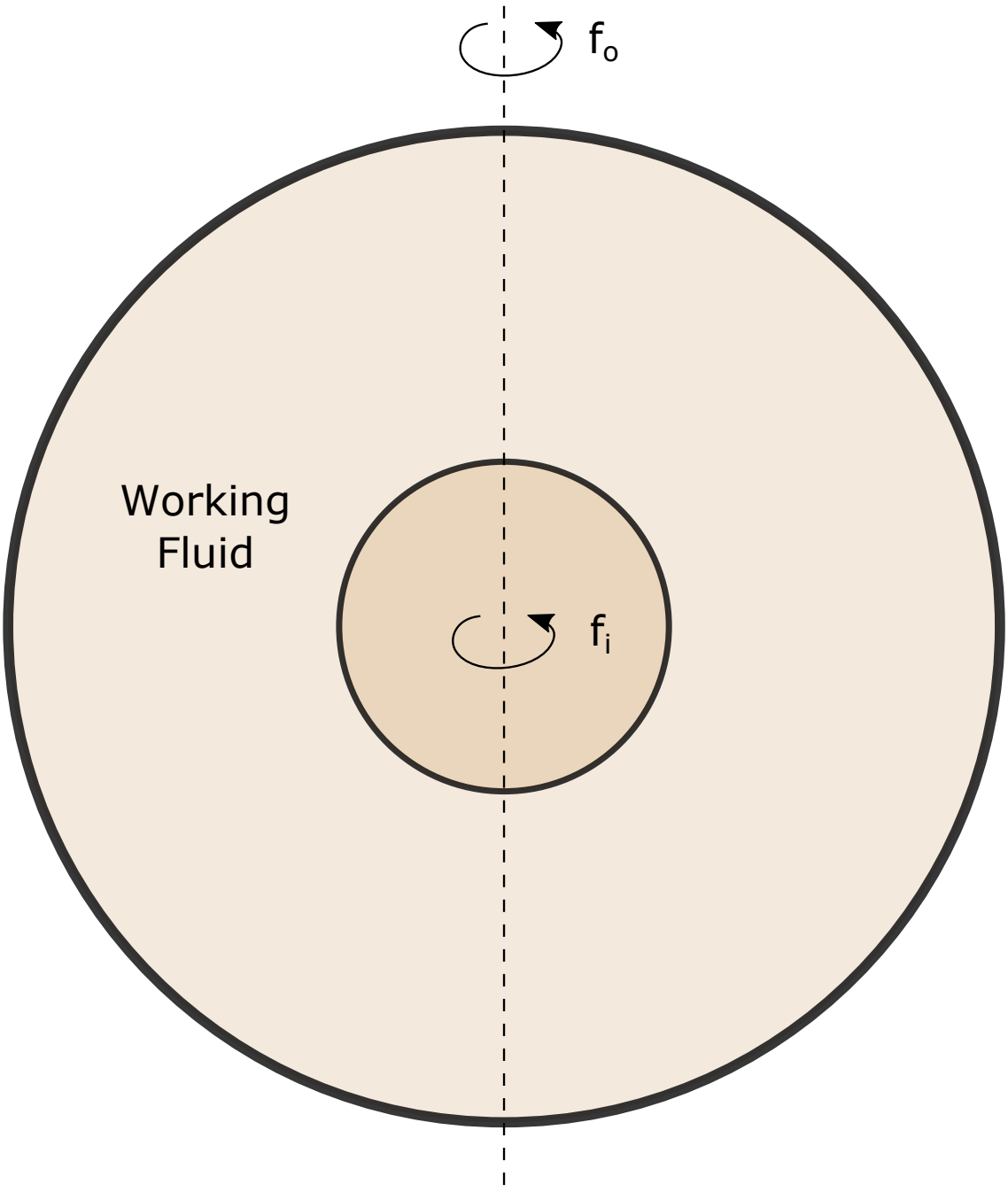

Figure 1.1: Diagram of Spherical Couette Flow. The working fluid is located between an outer spherical shell and an inner sphere; flow is driven by differential rotation of the inner and outer spheres, which share an axis. For experimental devices, the inner sphere must be supported by a shaft arrangement.

representing the mantle, and the inner sphere corresponding to the solid inner core. The magnetic field of the Earth impacts humans both in the field of navigation (via compass) and by protecting the Earth from the solar wind. If the Earth's magnetic field was to disappear suddenly, compasses would of course no longer work, and animals that rely on it for nagivation would also face difficulties. The main effect on humans however would be on technological devices that are sensitive to the radiation and magnetic fields due to the solar wind and solar storms, namely satellites and the power grid. Without the Earth's magnetic field, satellites would be more quickly degraded due to increased radiation levels in low Earth orbit, and could be knocked out entirely by solar flares. The rate of glitches in the electronics onboard satellites increases over the so-called South Atlantic Anomaly, where the geomagnetic field is significantly weaker (and indeed extrapolating down to the core-mantle boundary (CMB), there is a patch of reversed magnetic flux there).

The first major technological use of the geomagnetic field was the compass. At the most basic level of navigation, one can use the fact that compasses point north. This uses the fact that the Earth's field is primarily dipolar, with the south magnetic pole approximately co-located with the north pole of Earth's rotation axis. Once the age of exploration started, with ships navigating across oceans and even all around the world, more detailed knowledge of the magnetic field was needed for navigational purposes, with the primary measurement being the so-called declination of the magnetic field, that is the deviation of the horizontal component of the magnetic field from true north, as a function of longitude and latitude. The latter can be determined relatively straightforwardly with astronomical measurements,

while the determination of the former is more challenging but was also the subject of much effort during this time. Measurements of the overall strength of the field as well as the inclination of the field (the amount by which the overall local magnetic field vector is deflected from horizontal) were also taken during this time. The field inclination, declination, and overall strength together fully determine the local magnetic field vector. Gauss was the first to attempt a global model of the geomagnetic field using local measurements, performing a least squares fit of a vector spherical harmonic expansion to local field measurements [17], with the coefficients of the (truncated) expansion being called Gauss coefficients as a result.

In addition to the more complicated structure of the Earth's magnetic field revealed by such measurements, another aspect that became apparent over time was its dynamic nature. That is, the local magnetic field (inclination, declination, and overall strength) varies over time. Over the period of historical geomagnetic records, the field strength has decreased by about 10 percent, along with various smaller scale changes. There also appears to be a slight westward drift of the magnetic field structures relative to Earth's crust.

The magnetic field of the Earth has also undergone greater changes in the more distant past, the most dramatic of these being field reversals. In a field reversal, the Earth's field weakens, with the dipole component especially weakening or even disappearing, before reappearing with its orientation reversed; for instance, before the most recent field reversal about 780,000 years ago compasses would have pointed approximately south. The Earth's field has reversed approximately once every 450,000 years, though the timing is not regular and the process itself seems to

be chaotic. In addition to the irregular history of reversals, another phenomenon of interest is the occurrence of so-called superchrons, long periods on the order of tens of millions of years during which there were no reversals. While the orientation of the Earth's field is recorded anywhere rock containing ferromagnetic material is heated above the corresponding Curie temperature and then cooled, the most dramatic example of this is seen in the ocean floors. At the mid-oceanic ridges, new oceanic crust is constantly being created, and thus as the rock cools it records the current magnetic field orientation, and is slowly carried away from the ridge as the sea floor continues to spread. Surveys of the sea floor have determined that the remanent magnetization of the rocks lies in strips running parallel to the mid-ocean ridges, with the remanent magnetization either parallel or anti-parallel with the current field orientation. Thus, the magnetic field record provided key evidence for sea-floor spreading and plate tectonics. The sea floor magnetic records also provide fairly straightforward evidence of the reversals in Earth's magnetic field going back more than 100 million years. Continental rocks also bear the imprint of the reversals, including ones going back much further (the ocean doesn't provide anything past that since the oldest oceanic crust is only about 180 million years old; all older oceanic crust having been subducted), but its interpretation is more involved. The evidence from continental rocks is important in establishing that the Earth has had a dynamo for billions of years, and also provides a key constraint on continental positions in the past (giving the paleolatitude, under the assumption of an approximately axial dipole dominated–field).

In addition to the interest in its magnetic field as a general geological diag-

nostic tool, the Earth's field is also one of the major properties that can be used in comparing it to other planets, to help in probing the properties of other planets' interiors. As noted above, in addition to the Earth, the planets Mercury, Jupiter, Saturn, Uranus, and Neptune have dynamos, and Mars did in the past. Venus does not currently have a magnetic field, and it is unknown if it had one in the past, though it has been suggested that some of the highlands of Venus may contain magnetite that has remained below its Curie temperature and could thus provide a record of any previous magnetic field [18]. It is speculated that the reason Venus lacks a magnetic field is due to it being in a different thermal regime from the Earth: while the Earth loses heat at a relatively constant rate with plate tectonics driven by mantle convection, which in turn cools the outer core of the Earth and provides an energy source for the geodynamo, Venus appears to have occasional massive resurfacing events that release large amounts of heat, followed by a period where the crust is stagnant and heat is only lost via conduction out of the crust at a low rate [19]. This current state, with perhaps a stagnant mantle and core, could result in too little energy being available to drive a dynamo. Thus the presence or absence of a magnetic field can be used to infer information about the interior of a planet that might otherwise be unavailable.

The comparative planetology aspect also comes up in the topic of planetary habitability, including in the study of exoplanets. The presence of a magnetic field is believed to be an important element of planetary habitability, and the early shutdown of the Martian dynamo is postulated to have played a role in assuring Mars became the relatively inhospitable planet it is today. While Mars at one

point did have a dynamo, this shut down early in its history, presumably due to a loss of a driving mechanism as it cooled much more rapidly than the Earth [20]. There is some evidence that Mars was at one time warmer, perhaps with a thicker atmosphere and liquid water existing (at least occasionally) on the surface. The shutdown of the dynamo meant that Mars was left with just patches of magnetic field due to remanent magnetization of its crust, much weaker than the global-scale field possible with a dynamo. This in turn meant a much reduced protection of the Martian atmosphere from the solar wind, resulting in the erosion of the Martian atmosphere to its present state [20].

1.1.2 Astrophysics

While the Earth's core is the primary motivation for the geometry of the experiments described in this thesis, these experimental investigations can also inform a broader array of studies of conducting fluids. In addition to planets (touched on in the previous section), magnetic fields are found in most if not all stars, as well as accretion disks (both those leading to stellar system formation, and those around compact objects like white dwarfs, neutron stars, and black holes), and in the interstellar and intergalactic medium.

A primary motivation of dynamo studies is to understand how various astrophysical bodies, including the Earth and the Sun, generate their magnetic fields. Historical observations of sunspots and global models of Earth's magnetic field are available for the past few hundred years, giving a sense of the dynamics of both

bodies in that time period. [21] [22] In the satellite era, much more refined measurements are available for both bodies, though these data are limited to a timespan of decades. These include satellite measurements of Earth's field [23] as well as X-ray observations of the Sun, giving more detailed information about magnetic activity in its corona [24]. Spacecraft have also provided measurements of other solar system bodies.

The solar observational data in particular provide a portrait of a dynamic magnetic field. Sunspots (the sites of intense magnetic fields) undergo regular variations in number and spatial distribution during the 11-year solar cycle (or 22 years to return to the same polarities). Moreover, the sunspot number has shown significant variations during historical times, including the Maunder minimum when very few sunspots were observed for an extended period. On shorter time scales, magnetic fields influence the evolution of the solar atmosphere, including playing a key role in coronal mass ejections (CMEs), which can in turn affect the magnetosphere of the Earth, as ejected material and its associated magnetic fields interacts with Earth's magnetic field.

In addition to the observations of the magnetic fields of these bodies, other investigations, observational as well as experimental and computational, have greatly improved the theoretical understanding of both the Sun and the Earth. In particular, seismological studies of the Earth and helioseismological studies of the Sun have provided knowledge of the structure of their interiors, which can then be combined with experimental and numerical investigations of material properties. This in turn allows improved estimation of relevant dimensionless parameters.

Besides the dynamo process itself, the interaction of magnetic fields with conductive fluids is of interest for the new degrees of freedom it offers. One notable example of this is the magnetorotational instability, in which a shear flow that is Rayleigh stable is destabilized by a magnetic field [25]. This potentially allows for much greater angular momentum transport than would be expected without the magnetic field, and plays a major role in current theories of accretion in astrophysical systems. Accretion disks are believed to be an integral step in the formation of stars and planetary systems, whereby clouds of gas and dust collapse to form a star and any planets and other objects that orbit it. In addition, accretion disks can form in binary systems, where matter from a star accretes onto a compact companion (a white dwarf, neutron star, or black hole), and in active galactic nuclei (AGN) where matter accretes onto a supermassive black hole. Conservation of angular momentum is central to the reason for disk formation: any given protostellar cloud, which by some perturbation or other has begun the process of gravitational collapse, will in general have some net angular momentum; similar remarks apply to the case of binary systems and AGNs. While the kinetic energy released during gravitational collapse is converted into heat which in turn can be radiated away, allowing the collapse to continue, the angular momentum cannot be similarly radiated away. Thus a disk forms, with the protostar at the center, and with the disk's axis in the direction of the original cloud's net angular momentum. Particles in the disk will be in approximately Keplerian orbits about the center of mass of the system, and so the angular velocity of the particles decreases with distance from the system center. Thus there is shear present in the system, although the system is stable according

to the Rayleigh criterion. According to classical hydrodynamic theory, with realistic parameters put in for models of accretion disks, such systems should not be able to shed angular momentum at rates consistent with the rate of accretion observed for such systems [26]. This apparent paradox is resolved by the realization that magnetic fields are essentially always present in such systems, and such disks are generally hot enough to be at least partially ionized, and thus conductive. Thus, in addition to hydrodynamic effects, which here appear unable to achieve the necessary rate of angular momentum transport, there are hydromagnetic effects, the relevant one here being the so-called magnetorotational instability (MRI).

1.1.3 Helioseismology

While the previous two sections provided some background on motivations based on natural science, some of the experiments described in this thesis have the intermediate motivation of developing an experimental technique that allows inferences of fluid flow velocities using acoustic modes. This technique is based on a similar approach used in the field of helioseismology. In this section we provide some background both of the techniques used in helioseismology, and motivation for why a similar technique is of interest in our experiments.

An important consideration for our experiments is the working fluid used, which in turn informs the experimental design (see chapter 3 and the choice of instrumentation). Liquid sodium has been used in all the hydromagnetic experiments carried out in Dan Lathrop's laboratory at the University of Maryland. This

choice of working fluid is motivated by the conductivity of liquid sodium, which is higher than any other practical liquid available. With this choice comes a number of challenges, but one of the greatest experimentally is common to all liquid conductors, namely the opacity of the fluid. Determining the flow patterns in a liquid sodium experiment is challenging; unlike in water experiments one cannot use optical tracking of tracer particles to extract a detailed map of the velocity field. Other, indirect techniques must be used. By applying a magnetic field and measuring the field induced by the flow, one can put constraints on the possible flow patterns present in the fluid (though generally more than one flow pattern can give rise to the same induced field for a given applied field, so ambiguity remains; see section 2.3.1). This approach works since magnetic fields can penetrate the liquid sodium, and the modifications caused by the flow are informative. In addition to magnetic fields, pressure or sound waves pass easily through liquid sodium, and besides pressure measurements (giving a relatively global measure of the fluid state), ultrasound doppler velocimetry (UDV) has been used to determine the parallel component of velocity along a chord through the fluid volume.

Both inversion of the induced magnetic field and UDV have limitations. Using the global pattern of the applied and induced magnetic fields (represented as an expansion in vector spherical harmonics) and some selection rules [27], it is possible to infer the global velocity patterns that could be present, but as noted above the inversion is not unique. UDV measurements, again as noted above, give only local measurements of one velocity component, and thus many measurement devices, or repeated experiments with the ultrasound device in different locations and

pointing in different directions, are required to get the global velocity pattern. In addition UDV measurements require tracer particles, and while naturally present oxide particles often serve this purpose, their exact properties and locations within the flow are not easily controlled. Adapting the techniques of helioseismology to laboratory experiments offers a way to potentially combine aspects of both these techniques, with acoustic waves being used to probe the flow (like UDV) but using global modes that give a picture of the global flow pattern (as in the magnetic field inversion technique).

As its name implies, helioseismology is a field of study focused on the sun, using techniques analogous to those used in seismological studies of the Earth. The basic idea is that acoustic (i.e. pressure) waves can propagate through the sun, and so it has resonant modes. Since the sun is nearly spherically symmetric, the structure of these modes is amenable to analytical approximation. If there is any acoustic excitation of the sun, the resonant modes can be excited. On the Earth the excitation is by earthquakes (a natural phenomenon), as well as man-made explosions. While we are not currently capable of inputting acoustic energy into the sun, fortunately the vigorous turbulent flow in the star's convective zone is sufficient to excite many modes.

Because the sun has global acoustic modes, and these are excited by turbulent flows in the convective zone (driven ultimately by the nuclear fusion taking place in the sun's core). It is natural to consider how we might go about observing these modes. Since acoustic modes cannot propagate through vacuum, the acoustic energy in the sun is trapped in it. Some modes are only partially trapped, and

thus lose energy in the form of running waves in the solar atmosphere, and so are expected to be strongly damped. [28] Energy leaking in this way also drives some of the dynamics of the solar atmosphere. [29] While the pressures at the sun's surface cannot be measured directly, the modes do cause spatially coherent displacements across the sun's surface with a characteristic frequency. The spatial pattern and frequency of this displacement field can be extracted from observations of the sun by measuring doppler shifts of the h-alpha line (and others), caused by the up and down motion of the solar plasma that is emitting this light.

Using such measurements, helioseismologists have now identified more than a thousand such modes. Since the sun is approximately spherically symmetric, these modes can be identified by the number of radial nodes n present in them, along with their spherical harmonic degree l and order m. For a perfectly spherically symmetric system, all the modes in a given (n, l) family would have the same frequency, since the different m-values require picking an axis of rotation, and in this case such a choice is arbitrary. If a specific axis is selected (in the sun's case, it's rotation axis), the modes with different m-values in a given (n, l) family can split (with the number of modes given by $2l + 1$, with m running from $-l$ to $+l$). Thus, rotation splits the frequencies of the various modes in each of the (n, l) multiplets, with the amount of splitting giving information about the rotational depth profile of the sun. Since the sensitivity of a given mode to rotation (or more generally, azimuthal flow) will depend on its structure, by using many different modes a picture of the azimuthal flow as a function of radius and polar angle can be built up. Also, it is important to note that any deviations from spherical symmetry (like the presence of a shaft

in the 60 cm experiment) may also introduce splitting of multiplets, though modes with the same absolute value of m will not be split by this mechanism. Finally, exchange of energy among the modes induced by the flow, which is called coupling, may also cause splittings.

By using the frequencies of various modes, helioseismologists have improved models of the internal structure of the sun, in turn providing independent checks of models of physical processes in the solar interior. The amount of splitting of modes in a given (n, l) family with different m numbers has in turn been used along with a model for the sun's structure to infer the zonal flow rotation profile in the sun (that is, the azimuthal velocity v_ϕ of solar plasma as a function of radius r and polar angle θ), with reliable inversions extending from the solar surface down to below the transition from the solar convection zone to the radiative zone, around $r = 0.7R_{sun}$. In particular, this approach yielded the surprising discovery that the surface differential rotation (with the equatorial region rotating faster than the polar regions) extends all the way through the solar convection zone, with this differential rotation being accommodated to the uniform rotation of the solar radiative zone in a relatively thin (in radius) zone of high shear, called the tachocline. [30] This region is speculated to play a role in the solar dynamo. [31]

One of the goals of the work described in this thesis is to implement these helioseismology techniques in liquid sodium experiments, to further our understanding of turbulent hydromagnetic flow, including flows possibly relevant to dynamo processes in the Earth, the Sun, and other astrophysical bodies.

1.2 Contribution of the Author

The author modified the top inner bearing and seal assembly, as well as the inner shaft, of the 60 cm experiment, and designed and constructed (with welding done by Don Martin) a reaction torque sensor used to measure the torque needed to drive the inner sphere at its rotation rate. The author installed the microphones and speakers used in performing acoustic experiments in air and nitrogen gas in the 60 cm experiment, and designed and constructed the associated rotating electronics used to power these instruments and acquire the relevant data. The author led the acoustic experimental campaigns in the 60 cm experiment, and served as a co-pilot or as the lead on several experimental campaigns in the 3 m experiment. The author converted the LabView code used in data acquisition for the 60 cm experiment to Matlab, and converted the analysis code originally written in C to Matlab, in addition to writing a number of other analysis scripts in Matlab. The author replaced the LabView control code with C code, used to control the motors and magnets used in the 60 cm experiment, and adapted from similar code written for the 3 m experiment by Santiago Triana. The author collaborated with Dan Lathrop, Ved Lekic, and Anthony Mautino on the analysis of the acoustic mode results in 60 cm, including the identification of acoustic modes and matching same with theoretical predictions, and the extraction of mode splittings from the data. This includes the identification of more than 20 modes, and simultaneous splitting measurements for more than 10 modes, at a variety of different inner and outer rotation rates. The author led the writing of a review paper focusing on liquid

sodium experiments: Adams, Matthew M., et al. "Liquid sodium models of the Earth's core.", *Progress in Earth and Planetary Science* 2.1, (2015):1. The magnetic experiments with the 3 m device included a number of runs, primarily led by Doug Stone, at full speed, and the author performed some of the analysis of this data, including some work on estimating flow states using magnetic results. The author collaborated in ongoing efforts to attempt to identify acoustic modes in the 3 m experiment.

Chapter 2: Theoretical Background and Review of Past Work

In this chapter we provide some theoretical background for the thesis, as well as a review of past work. For many systems of interest, including the experiments that are the focus of this work, the equations of motion in the relevant parameter range do not have known analytical solutions, and direct numerical simulation is not feasible; nevertheless, the equations of motion can be used to guide investigations. One example of this is the widespread use of dimensionless parameters, formed generally by making the equations of motion dimensionless; the magnitude of these parameters (in particular, whether they are much less than one, close to one, or much greater than one) can then be used to divide parameter space into various regimes where different behavior may be expected.

We start with a consideration of hydrodynamics, that is fluid flow without any influence of magnetic fields. In this case the equations of motion are the Navier-Stokes equation, and the continuity equation. In particular, we consider spherical Couette flow (see Figure 1.1), and touch on issues relating to turbulence. Since we are considering rotating systems, we use the Navier-Stokes equations written in a rotating frame. Next we consider hydromagnetic systems, where the Navier-Stokes equation is modified by the addition of the Lorentz force, and another equation, the

so-called induction equation, governs the evolution of the magnetic field. Finally, we close with a review of the basic theory of the splitting of acoustic modes by fluid flow, used in helioseismology and applied in the air experiments discussed in chapter 5 (with ongoing work to apply the technique in liquid sodium).

2.1 Hydrodynamics

Fluids exhibit a wide variety of properties and behaviors; here we will focus on the equations of motion applicable to viscous Newtonian fluids (which includes both water and sodium). After presenting these equations and describing the terms appearing in them, and commenting on some of their properties, we proceed to make them dimensionless. This results in the definition of several dimensionless parameters, and we review their meaning and indicate how they are used to guide investigations in fluid dynamics. We then provide a review of past work — analytical, numerical, and experimental — in hydrodynamic systems of interest.

2.1.1 Equations of Motion

The equations of motion for the case of hydrodynamics are the equation of mass conservation:

$$\frac{\partial \rho}{\partial t} + \nabla \cdot (\rho \mathbf{u}) = 0 \tag{2.1}$$

and the Navier-Stokes equation, in this case for a Newtownian viscous fluid:

$$\rho(\frac{\partial \mathbf{u}}{\partial t} + \mathbf{u} \cdot \nabla \mathbf{u}) = -\nabla p + \mu \nabla^2 \mathbf{u} + \mathbf{F} \tag{2.2}$$

essentially $\mathbf{F} = m\mathbf{a}$ for a fluid. The left hand side represents the acceleration of a fluid parcel, and since it is embedded in a continuous medium (the fluid), in addition to a simple time derivative of the fluid parcel's velocity, there is the so-called *convective acceleration*, taking into account changes in the fluid parcel's velocity due to it being advected by the flow. For instance, in steady flow down a pipe, the fluid speeds up in regions where the pipe narrows; for a steady state flow, though, none of the parameters of the system are varying in time, and thus the change in speed of a fluid parcel entering this region of higher velocity is not due to a time-dependence in the system but to the fact that the parcel has been carried by the flow ("advected") to a different region of the flow. These two accelerations are multiplied by the density of the fluid ρ, thus making it analogous to the $m\mathbf{a}$ of Newton's Second Law of Motion. On the right-hand side of the equation, then, is the analog of $\mathbf{F}$. The first term, the gradient of the pressure p, represents the force on a fluid parcel due to the surrounding fluid, normal to the (imaginary) interface between them. The next term represents viscous dissipation, that is, the resistance to fluid parcels sliding past one another, and thus gives the force on a fluid parcel due to the surrounding fluid in directions tangent to the interface between them; μ is the dynamic viscosity of the fluid, a measure of how much elements of the fluid resist sliding past one another. Finally, the last term on the force side of the equation is $\mathbf{F}$, representing all external forces acting on the fluid. This could include body forces, such as gravity, as well as boundary forcings (such as those due to an impeller). Dividing this equation through by the density ρ, and denoting the

kinematic viscosity by ν, with $\nu = \mu/\rho$, we have

$$\frac{\partial \mathbf{u}}{\partial t} + \mathbf{u} \cdot \nabla \mathbf{u} = -\frac{1}{\rho}\nabla p + \nu \nabla^2 \mathbf{u} + \frac{\mathbf{F}}{\rho} \tag{2.3}$$

For the cases of interest here (at low Mach number), the fluid can be assumed to be incompressible, so ρ is a constant, and the equation of continuity simplifies to

$$\nabla \cdot \mathbf{u} = 0 \tag{2.4}$$

Also, since the systems we will be considering are rotating, it is convenient to work in a rotating frame, with (constant) rotation vector $\mathbf{\Omega}$, so that the Navier-Stokes equation becomes

$$\frac{\partial \mathbf{u}}{\partial t} + \mathbf{u} \cdot \nabla \mathbf{u} = -\frac{1}{\rho}\nabla p + \nu \nabla^2 \mathbf{u} + \frac{\mathbf{F_R}}{\rho} - 2\mathbf{\Omega} \times \mathbf{u} - \mathbf{\Omega} \times \mathbf{\Omega} \times \mathbf{r} \tag{2.5}$$

where $\mathbf{F_R}$ is the external force as seen in the rotating frame, and $\mathbf{r}$ is the position vector of the fluid parcel. In shifting to the rotating frame, two new terms have appeared in the equation: the Coriolis force $-2\mathbf{\Omega} \times \mathbf{u}$ and the centrifugal force $-\mathbf{\Omega} \times \mathbf{\Omega} \times \mathbf{r}$. The centrifugal force can also be written in the form $-\frac{1}{2}\nabla(\mathbf{\Omega} \times \mathbf{r})^2$, so defining the *reduced pressure* $P = p - \frac{1}{2}\rho(\mathbf{\Omega} \times \mathbf{r})^2$, we can combine the centrifugal force with the pressure force. Then we have

$$\frac{\partial \mathbf{u}}{\partial t} + \mathbf{u} \cdot \nabla \mathbf{u} = -\frac{1}{\rho}\nabla P + \nu \nabla^2 \mathbf{u} + \frac{\mathbf{F_R}}{\rho} - 2\mathbf{\Omega} \times \mathbf{u} \tag{2.6}$$

This is a challenging system of equations to solve. In fact, while solutions are known when various approximations and simplifications are made in the above equations, for the general case there are no known solutions that exist for all time. Finding such a solution is the task required to obtain one of the so-called Millennium Prizes offered by the Clay Mathematical Institute, or alternatively showing that such solutions do not exist (though this is viewed as unlikely).

One way of describing the difficulty is to divide up differential equations into a number of groups based on their properties. The first division is that between ordinary and partial differential equations (see Table 2.1). Ordinary differential equations (ODEs) are generally easier to solve than partial differential equations (PDEs), since in PDEs the variables are a function of multiple variables (for physical problems, generally time and space), and thus have the scope for more complicated dynamics. In solving PDEs, one major strategy is to turn them into an ODE (or a set of ODEs).

Another important distinction is between linear and nonlinear differential equations. Solutions to linear ODEs have many nice properties (such as obeying superposition) that make the solution of such equations relatively straightforward, compared to nonlinear equations. Nonlinear differential equations often have no known analytical solutions, and for nonlinear systems a common approach is to linearize about some point of interest to gain some insight into the dynamics of the system. The general Navier-Stokes equation is an example of a nonlinear PDE, and thus is one of the most challenging to solve. One manifestation of this difficulty is seen in physical systems as the phenomenon of turbulence. Turbulence refers to the

Differential Equations	Linear	Non-Linear
Ordinary	Harmonic Oscillator	Verhulst (Logistic) Equation
Partial	Heat Equation	Navier-Stokes, General Relativity

Table 2.1: Categories of Differential Equations, with Examples.

fluctuations on a wide range of spatial and temporal scales seen in fluid flow.

2.1.2 Dimensionless Parameters: Hydrodynamics

As noted above, for hydrodynamics we use the continuity equation (eq. 2.1) and the Navier-Stokes equation (eq. 2.6) written in the rotating frame. It is convenient to make these equations dimensionless, for then the relative importance can be judged based on the magnitude of their prefactors. The continuity equation simply indicates that the velocity field is divergence-free, and since it only has one term, does not result in any dimensionless parameters upon dividing through by a velocity scale. In making this approximation (of an incompressible fluid), however, we do assume that the relevant velocity scale of the system, U, is much smaller than the speed of sound in the fluid, c_s. The sound speeds of the relevant working fluids are listed in Table 2.1.2. Since typical fluid flow speeds in the experiments will be on the order of tens of meters per second, this is a good approximation for the water and sodium experiments, while some compressibility effects may start to become apparent in the air experiments.

Turning now to the Navier-Stokes equation, we first consider the non-rotating case, and moreover for simplicity we drop the forcing term. Then we have the

following equation:

$$\frac{\partial \mathbf{u}}{\partial t} + \mathbf{u} \cdot \nabla \mathbf{u} = -\frac{1}{\rho}\nabla p + \nu \nabla^2 \mathbf{u} \tag{2.7}$$

We note that this equation involves both the fluid velocity and pressure, and has time and spatial derivatives. Thus the units used involve length, time, and mass. Picking a velocity scale U and a length scale L, we can construct a time scale L/U, and for a pressure scale we pick ρU^2. Then we can define the following dimensionless variables and operators:

$$\mathbf{u}' = \frac{\mathbf{u}}{U}, t' = \frac{Ut}{L}, \nabla' = L\nabla, p' = \frac{p}{\rho U^2} \tag{2.8}$$

and writing the original variables in terms of the dimensionless ones (and the scales we have selected), we have

$$\mathbf{u} = U\mathbf{u}', t = \frac{Lt'}{U}, \nabla = \frac{\nabla'}{L}, p = \rho U^2 p'. \tag{2.9}$$

Substituting these expressions into equation 2.7, we have

$$\frac{U^2}{L}\frac{\partial \mathbf{u}'}{\partial t'} + \frac{U^2}{L}(\mathbf{u}' \cdot \nabla')\mathbf{u}' = -\frac{U^2}{L}\nabla' p' + \frac{\nu U}{L^2}\nabla'^2 \mathbf{u}' \tag{2.10}$$

and multiplying through by L/U^2, defining the Reynolds number $Re = UL/\nu$, and dropping the primes on the dimensionless variables and operators, we have

$$\frac{\partial \mathbf{u}}{\partial t} + (\mathbf{u} \cdot \nabla)\mathbf{u} = -\nabla P + \frac{1}{Re}\nabla^2 \mathbf{u} \tag{2.11}$$

After carrying out this exercise, then, we have one dimensionless parameter, the so-called Reynolds number, Re. As can be seen from the above, it is constructed from a characteristic velocity scale U, length scale L, and the kinematic viscosity ν of the system under consideration, $Re = UL/\nu$, and its reciprocal is the prefactor of the term representing viscous dissipation in the Navier-Stokes equation. Specifically, this term represents the tendency of viscosity to smooth out velocity variations in the flow. Thus, when Re is small, the viscosity will dominate the equation and the flow will be laminar. When Re is large, on the other hand, the viscous term will be relatively small compared to the other terms in the equation, and large velocity fluctuations (including eddies and vortices) will be able to persist for a long time before viscosity causes them to decay (and may not decay away if there is persistent forcing of the fluid).

The Reynolds number is often used as a guide for when to expect the development of turbulence. Even in flows that are linearly stable at all Reynolds numbers, nonlinear instabilities (seeded by finite-sized perturbations, which are often present in experimental and natural systems) may develop at sufficiently high Reynolds number. Such is the case, for instance, with pipe flow. The Reynolds number can be interpreted as a ratio of the strength of advection of fluid momentum to its diffusion by viscosity. Thus, at large Reynolds numbers, any eddies or other structures in the fluid tend to be advected by the flow with very little viscous dissipation.

Next we consider the case of the Navier-Stokes equation in a rotating frame. Now in addition to the velocity scale U and length scale L, we have a natural time scale given by Ω^{-1}, where Ω is the rotation rate of the rotating frame of reference

Fluid	Sound speed (m/s)
Air (at 25C)	343
Water (at 20C)	1482
Liquid Sodium (at 110C)	2520

Table 2.2: Sound Speed in Working Fluids.

in an inertial frame, $\Omega = |\mathbf{\Omega}|$. While we have suppressed the appearance of any external forcing $\mathbf{F}$ in the Navier-Stokes equation, ultimately this forcing is what sets the typical velocity scale in the experiment (e.g., for the case of the experiments considered here, we drive a shear flow, and thus velocity scale would be related to the differential rotation of the inner and outer boundaries of the fluid volume). Another velocity scale is given by ΩL, and there is now more than one way to construct a pressure scale for the system. Following Zimmerman [32], we choose $\rho\Omega LU$, and making the rotating version of the Navier-Stokes equation dimensionless, we have, after some rearrangement, the following dimensionless equation:

$$\frac{\partial \mathbf{u}}{\partial t} + Ro(\mathbf{u}\cdot\nabla)\mathbf{u} = -\nabla P + \frac{Ro}{Re}\nabla^2\mathbf{u} - 2\Omega\times\mathbf{u}, \tag{2.12}$$

where we have defined a new dimensionless parameter, the Rossby number $Ro = U/(\Omega L)$. This quantifies the ratio of the velocity scale of the flows in the rotating frame with the velocity scale of the overall system rotation. An alternative dimensionless group that can be used to quantify the strength of the system rotation is the so-called Ekman number, $E = \nu/(\Omega L^2)$, which gives the ratio of viscous forces to Coriolis forces. Given these definitions, we have $E = Ro/Re$, so we can also write

equation 2.12 as

$$\frac{\partial \mathbf{u}}{\partial t} + Ro(\mathbf{u} \cdot \nabla)\mathbf{u} = -\nabla P + E\nabla^2 \mathbf{u} - 2\Omega \times \mathbf{u}. \tag{2.13}$$

In this case, then, two of the three dimensionless groups E, Ro, and Re are sufficient to make the rotating Navier-Stokes equation dimensionless. As can be seen, there is some freedom in constructing dimensionless parameters, with multiple possibilities. This is quantified by the Buckhingham Π theorem, which states that for a system described by n parameters, with m different fundamental units used, $n - m$ dimensionless parameters are needed to specify it. If $n > m$, then there will be multiple ways of constructing such a set, since multiple expressions will share the same unit and can thus be substituted for each other in making dimensionless groups. For instance, applying the theorem to the hydrodynamic case for our experiments, we note that they are characterized by the material parameters ρ and ν of the fluid, the geometrical factors r_i and r_o, the radii of the inner and outer spheres, respectively, and by the experimental parameters (the "control knobs" we have which we can vary in experiments) Ω_i and Ω_o, the rotating rates of the inner and outer spheres. So for hydrodynamic experiments we have 6 parameters, which use 3 fundamental units: length, time, and mass, and thus the system is specified by 3 dimensionless groups. As noted above, two of Ro, E, and Re can be used, and in this case take into account variations in Ω_i and Ω_o. Thus the exploration of the (Ω_i,Ω_o) space can also be characterized as exploring the (Ro,E) or (Ro,Re) space. For the third group (which of course is not unique), one choice is to use the radius

ratio of the experimental vessel, $\Gamma = r_i/r_o$. Also, we note that the only parameter containing the unit of mass is the density, ρ. So, the density does not appear in any of the dimensionless groups, since there is no other unit that can cancel out the mass unit in it. One way of interpreting this is as a sign that it is natural to use the kinematic viscosity ν, rather than the dynamic viscosity μ. If we had used μ instead of ν, then wherever ν appears in dimensionless groups (like Re and E), we would have instead had μ/ρ, since these are the only terms containing mass units and thus must always go together in dimensionless groups to ensure there isn't a remaining unit of mass. For the experiments described below, we will use $Ro = (\Omega_i - \Omega_o)/\Omega_o$, thus choosing $U = (\Omega_i - \Omega_o)L$ and $\Omega = \Omega_o$ in the definition of Ro. For E we use $L = r_o$ and $\Omega = \Omega_o$. For the air experiments described below in section 5.4 with the outer rotating at 6 Hz, this gives $E = 4.6 \times 10^{-6}$.

There is a hierarchy in Reynolds number among observations, experiments, and simulations (see Table 2.2.2). The larger the Reynolds number, the greater the range of scales that are important to the dynamics of the system. Thus, numerical simulations become prohibitively expensive much above a Re of 10^4, though higher values can be reached by making various assumptions and approximations. Meanwhile, experiments can reach Reynolds numbers of around 10^6, with some of the largest experiments reaching 10^8. Astrophysical systems, on the other hand, such as accretion disks, may be characterized by Re of around 10^{12} or more. Thus, both experiments and observations can provide knowledge about systems at Re inaccessible numerically, and some natural systems are characterized by dimensionless parameters (including Re) that are inaccessible to both simulations and experiments.

2.1.3 Past Work: Theory and Simulations

For the case of hydrodynamic spherical Couette flow, generally three limits can be distinguished (see Figure 2.1.3) the case of outer stationary (the limit $|\mathrm{Ro}| \to \infty$) and the case of rapid outer rotation with either the inner sphere sub-rotating (Ro $\to -0$) or with it super-rotating (Ro $\to +0$). For the outer stationary case, a jet of fluid comes off the inner sphere, setting up a poloidal return flow. In the latter two cases, the bulk of the fluid spins with the outer sphere, while the volume of fluid inside the tangent cylinder spins under the influence of both the inner and outer spheres, and the velocity jump across the tangent cylinder is accomodated by a thin shear layer. This so-called Stewartson layer was first predicted by Stewartson [33], who analytically studied the case of spherical Couette with strong overall rotation and infinitesimal differential rotation. For strong forcing, both the equatorial jet (infinite Ro) and the Stewartson layer ($|Ro| \ll 1$) develop instabilities, which require numerical studies to elucidate.

When the differential rotation becomes sufficiently large, instabilities develop in the Stewartson layer of an overall rapidly rotating system. They were studied numerically by Hollerbach [34] for a radius ratio of $r_i/r_o = 1/3$. In this study, the primary concern was the dependence of the instabilities on the sign of Ro. This work was partly motivated by a discrepancy in the experimental results obtained by Hide and Titman [35] and Früh and Read [36] regarding the effect of changing the sign of Ro; the original analysis of Busse [37] had predicted that the system should be symmetric about Ro = 0. Hollerbach (2003) found that Ro > 0 (inner super-

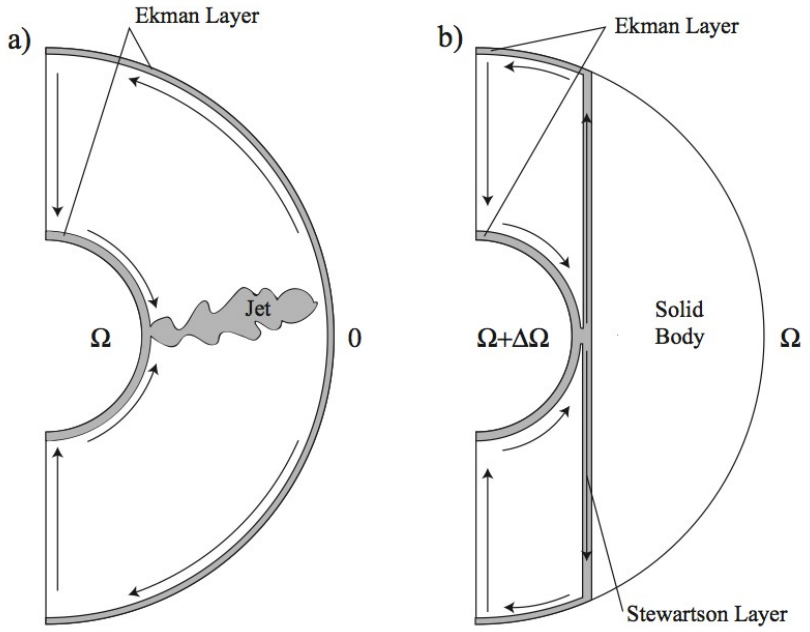

Figure 2.1: General circulation patterns for spherical Couette flow. Flow patterns for the case of outer sphere stationary (a) and rapidly rotating (b). For (a), the super-rotating inner sphere pumps fluid out into the bulk in the form of an equatorial jet with a poloidal return flow. For (b), the fluid outside the tangent cylinder spins in solid body rotation with the outer sphere, while the fluid inside the tangent cylinder spins at a rate intermediate between the two spheres with Ekman pumping along the boundaries of the tangent cylinder. The velocity jump across the boundary of the tangent cylinder is accommodated by the Stewartson layer, which is a region of high shear. From [32].

rotating) results in non-axisymmetric instabilities of the axisymmetric base state that have progressively larger azimuthal wavenumbers m for lower E (i.e. faster overall rotation). However, the instability has azimuthal wavenumber $m = 1$ for most of the range of E considered (down to 10^{-5}) for $\mathrm{Ro} < 0$ (inner sub-rotating). Thus the sign of Ro for values near zero is significant, while the limits of infinite Ro are the same for both positive and negative values. In a later study [38], Hollerbach et al. investigated stronger differential rotation both numerically and experimentally for the case $\mathrm{Ro} > 0$. They found that for sufficiently strong differential rotation a series of mode transitions back to smaller azimuthal wavenumbers occurs.

Another interesting regime is found near $\mathrm{Ro} = -2$, in which the spheres are counter-rotating with the same angular frequencies. In this regime (with the relative sizes of the spheres also possibly playing a role), the bulk of the fluid is at rest in an inertial frame, and thus while the flow can be strongly driven, the influence of rotation is small (see e.g. [39]).

Wicht [40] performed an extensive study of wide-gap spherical Couette flow (with Earth-like radius ratio $r_i/r_o = 0.35$) across a wide range of parameter space. The study varied both outer sphere rotation (i.e. E) and the amount of differential rotation (i.e. Ro) over a wide range. Specifically, the study covered the following range of parameters: $10^2 \leq |\mathrm{Ro/E}| \leq 10^5$ and $10^4 \geq \mathrm{E} \geq 10^{-6}$ (where the length scale used is $L = r_o - r_i$ in the definition of E). The results are consistent with previous numerical and experimental studies where the parameters overlap. For slow overall rotation, an equatorial jet formed that eventually developed instabilites as the inner sphere rotation rate (i.e. Ro) was increased and the Coriolis force

did not have a significant effect on the flow. For fast overall rotation (i.e. low Ekman number), a Stewartson layer is formed and develops various instabilities as differential rotation is increased. In addition, inertial waves are found, which are possibly driven by instabilities in the Stewartson layer, as posited by Rieutord et al. [41]

2.1.4 Past Work: Experiments

Previous studies have also investigated the spherical Couette system experimentally. In addition to systems using water (where no hydromagnetic effects would be present), liquid sodium systems can also shed light on the hydrodynamics of spherical Couette. When applied fields are weak, liquid sodium systems behave approximately like water systems operated at the same dimensionless parameters (Re, Ro, etc.). Thus, a good portion of the phenomena seen in liquid sodium experiments are in fact hydrodynamic, rather than hydromagnetic, with perhaps slight modifications due to the applied field. Of course, when applied fields are strong, this hydrodynamic limit no longer applies, and a system exhibiting dynamo action is also not in the hydrodynamic regime. Here we review some of the results in water experiments, as well as the hydrodynamic phenomena seen in weak-field liquid sodium experiments.

At the University of Maryland, a series of liquid sodium devices have been constructed. A device with a 30 cm diameter stationary outer spherical shell had flows driven by impellers, propellers, or an inner sphere. [42] A larger device was originally

constructed as a rotating convection experiment, with a cooled inner sphere 20 cm in diameter and a heated outer spherical shell 60 cm in diameter driving flows in liquid sodium, with the centrifugal force due to the overall system rotation standing in for gravity. [43] As mentioned above, the high thermal conductivity of sodium makes it difficult to achieve vigorous flows with a thermal gradient, so this device was modified to have a differentially rotating inner sphere. [44–46] Finally, the 3 m device is a spherical Couette device (3 m diameter outer sphere, 1 m diameter inner sphere) that was initially run as a water experiment but is now operating with liquid sodium (see e.g. Zimmerman 2010 and Zimmerman et al. 2014).

While the water experiments in the 3 m device were initially for mechanical debugging purposes in preparation for the sodium experiments, they provided some new results concerning non-magnetic spherical Couette flow. In these experiments, the two variables are the rotation rates of the inner and outer sphere. Using dimensionless parameters, this parameter space can be characterized by Ro and Re. In water, the primary measurements were the torque required to drive the inner sphere (from a reaction flange torque sensor), pressure measurements, and wall-shear and ultrasound Doppler velocimetry (UDV) measurements. It was found that Ro determines the state of the flow, while varying Re just scales the velocities and torques seen. For some Ro numbers, moreover, it was found that the system exhibited bistability, switching between two distinct states as determined by the torque required to drive the inner sphere at its rotation rate. [47] The torque was significantly higher in the so-called high torque state as compared to the low torque state.

This state was also investigated in liquid sodium with the 60 cm device (see

section 3.1 for more details of the apparatus). For these experiments an array of Hall probes measured the magnetic field outside the outer sphere, while the motor drives provided coarse-grained torque measurements. A relatively weak applied field allowed the velocity profile in the device to be inferred from induced field measurements. To do this, first the induced field is modeled as a sum of vector spherical harmonics up to degree and order 4. These Gauss coefficients are found via a least squares fit to the field measurements. Selection rules can then be used to determine the possible patterns of fluid flow in the device, since the applied field geometry is known (see e.g. [48]). From the magnetic field measurements, the presence of an inertial wave was identified, consistent with results in the 3 m device. In addition, the power in another Gauss coefficient correlated well with the low-torque state, and has been interpreted as the result of interaction of the Earth's field (which is not shielded out in the device) with a Rossby wave. This wave is nearly 2D, and given its geometry would not be expected to cause any induction at all when acted on by a uniform, axially-aligned field like the one applied in the experiment.

While the results from the 60 cm device are generally compatible with those from 3 m, a significant difference is found in the values of Ro for which the bistable states occur. This may be due to geometric differences between the two devices: the 60 cm device has a relatively thicker shaft which spins with the outer sphere, as opposed to the shaft in 3 m that spins with the inner sphere. Thus, at least in this case, analogous states can be found despite significant geometric differences in the devices, with the 60 cm device requiring a larger Ro, and thus faster relative inner

rotation, which intuitively might be thought of as being necessary to overcome the effect of the large shaft rotating with the outer sphere. [32]

In addition to regions of bistability, the 3 m water experiments also revealed the presence of precession-driven flows. [49] When the inner and outer spheres are locked together and spun up to some constant rotation rate, one might expect the flow to come to a state of solid body rotation with the spheres. However, the laboratory is not an inertial frame since the Earth is rotating. Thus, the axis of the experiment is precessing, completing one revolution a day. This precession of the experiment's rotation axis drives the spin-over mode, which can be understood as the fluid spinning in a state of solid-body rotation but with an axis that lags that of the experiment itself. Effectively, the fluid retains some "memory" of the previous orientations of the rotation axis. The structure and strength of the observed flows were consistent with the presence of a spin-over mode driven by precession. Since many planetary bodies, including the Earth, exhibit significant amounts of precession of their rotation axes, analogous flows can be expected in their liquid cores. Precessional forcing has been proposed as an energy source for dynamos, including the geodynamo. [50]

2.2 Hydromagnetics

In studying the dynamics of conductive fluid, including their interactions with magnetic fields, both the Navier-Stokes equations and Maxwell equations are used. As is the case for hydrodynamical systems, dimensionless parameters are often used

in describing hydromagnetic systems, to facilitate comparisons between theoretical, computational, experimental, and observational results. These dimensionless parameters are constructed by scaling the units of the equations of motion by appropriate factors for the system under study in order to nondimensionalize the equations; the relevant dimensionless parameters then appear as prefactors of the terms of the equation. While these parameters are in general not unique, a small number of interchangeable numbers are used in the community.

2.2.1 Equations of Motion

For the case of a conducting fluid in the presence of a magnetic field, we now have to include electrodynamic effects. The Navier-Stokes equation is modified by the addition of the Lorentz force $\mathbf{f_L}$ given by

$$\mathbf{f_L} = q(\mathbf{E} + \mathbf{u} \times \mathbf{B}) \tag{2.14}$$

where q is charge, $\mathbf{E}$ is the electric field, $\mathbf{u}$ is velocity, and $\mathbf{B}$ is magnetic field. Considering specifically a parcel of conducting fluid with charge density ρ_e, we can write for the specific Lorentz force $\mathbf{F_L}$

$$\mathbf{F_L} = \rho_e \mathbf{E} + \mathbf{J} \times \mathbf{B} \tag{2.15}$$

where $\mathbf{J}$ is the current in the fluid element. For the case of non-relativistic systems (as is the case for our liquid metal experiments), the electric field can be neglected,

as the time scale for charge imbalances to relax in the fluid (that is, for electrons to rearrange themselves to reduce any electric fields due to static concentrations of charge) is much shorter than any of the other relevant time scales. Thus, for the case of magnetohydrodynamics (MHD) in liquid metals, the two primary variables of interest are the fluid velocity $\mathbf{u}$ and the magnetic field $\mathbf{B}$. As noted above, the Navier-Stokes equation must be modified in this case to include the Lorentz force, which we wish to write in terms of the magnetic field and the fluid velocity. Using Ampere's law, we have that

$$\nabla \times \mathbf{B} = \mu(\mathbf{J} + \epsilon_0 \frac{\partial \mathbf{E}}{\partial t}) \tag{2.16}$$

and we note that for the case of non-relativistic MHD the displacement current can be neglected, so that the above becomes

$$\nabla \times \mathbf{B} = \mu \mathbf{J} \tag{2.17}$$

and we can write the Lorentz force as

$$\mathbf{F_L} = \frac{1}{\mu_0}(\nabla \times \mathbf{B}) \times \mathbf{B} \tag{2.18}$$

and putting this into the Navier-Stokes equation (written in the rotating frame), we have

$$\frac{\partial \mathbf{u}}{\partial t} + \mathbf{u} \cdot \nabla \mathbf{u} = -\frac{1}{\rho}\nabla P + \nu \nabla^2 \mathbf{u} + \frac{\mathbf{F_R}}{\rho} - 2\mathbf{\Omega} \times \mathbf{u} + \frac{1}{\rho \mu_0}(\nabla \times \mathbf{B}) \times \mathbf{B} \tag{2.19}$$

Also, we note that, like water, liquid sodium is approximately incompressible, so we can again take $\mathbf{u}$ to be divergence-free. To fully specify the system, we need an equation governing the evolution of the magnetic field, $\mathbf{B}$. We start with Faraday's law,

$$\nabla \times \mathbf{E} = -\frac{\partial \mathbf{B}}{\partial t} \tag{2.20}$$

giving the rate of change of $\mathbf{B}$. We note that the electric field here is the full electric field, and not just that due to static charges. Using Ohm's law,

$$\mathbf{J} = \sigma(\mathbf{E} + \mathbf{u} \times \mathbf{B}) \tag{2.21}$$

we can substitute for $\mathbf{E}$ in Faraday's law to find

$$\frac{\partial \mathbf{B}}{\partial t} = -\nabla \times (\frac{1}{\mu_0}\mathbf{J} - \mathbf{u} \times \mathbf{B}) \tag{2.22}$$

and as above we use Ampere's law to eliminate $\mathbf{J}$ to find

$$\frac{\partial \mathbf{B}}{\partial t} = \nabla \times (\mathbf{u} \times \mathbf{B} - \frac{1}{\mu_0}\nabla \times \mathbf{B}) \tag{2.23}$$

and using the vector identity

$$\nabla \times \nabla \times \mathbf{A} = \nabla(\nabla \cdot \mathbf{A}) - \nabla^2 \mathbf{A} \tag{2.24}$$

and the fact that $\mathbf{B}$ is divergence-free, i.e. $\nabla \cdot \mathbf{B} = 0$, and defining $\eta = 1/(\mu_0 \sigma)$, the

"magnetic diffusivity", we have

$$\frac{\partial \mathbf{B}}{\partial t} = \nabla \times (\mathbf{u} \times \mathbf{B}) + \eta \nabla^2 \mathbf{B}, \tag{2.25}$$

the so-called induction equation. This equation gives the evolution of the magnetic field of the system, as a function of the current field $\mathbf{B}$ and the fluid velocity $\mathbf{u}$. The first term on the right-hand side gives the changes in the magnetic field due to its advection by the fluid flow, and is the possible source of increasing magnetic field, including dynamo action. The second term, on the other hand, represents the tendency of the finite resistance of the fluid flow to smooth out variations in magnetic field and damp it, by dissipating the currents in the fluid flow. This equation couples $\mathbf{u}$ and $\mathbf{B}$, as does the Navier-Stokes equation with the Lorentz force term added, and we have a coupled, non-linear system of equations.

2.2.2 Dimensionless Parameters: Hydromagnetics

With the addition of magnetic fields to the dynamics of the physical system, and thus to the equations describing them, a number of new dimensionless groups can be formed. First we note that the only new variable that has been introduced is $\mathbf{B}$, so we can use the same definitions of dimensionless variables and operators as above, with the addition of a dimenionsionless magnetic field variable, $\mathbf{B}' = \mathbf{B}/B_0$, where we have normalized by B_0, the magnitude of the applied field. This is convenient since for all of the hydromagnetic experimental results we will be discussing later, there will be an applied field. Of course for the case of dynamo

action, there is no applied field, and then some other scale must be chosen for the field, like the typical strength of the field. Turning to the relevant equations, we first make the induction equation dimensionless, and after substitution we find

$$\Omega B_0 \frac{\partial \mathbf{B}'}{\partial t'} = \frac{U B_0}{L} \nabla' \times (\mathbf{u}' \times \mathbf{B}') + \frac{\eta B_0}{L^2} \nabla'^2 \mathbf{B}' \tag{2.26}$$

and after simplifying we have

$$\frac{\partial \mathbf{B}'}{\partial t'} = \frac{U}{\Omega L} \nabla' \times (\mathbf{u}' \times \mathbf{B}') + \frac{\eta}{\Omega L^2} \nabla'^2 \mathbf{B}' \tag{2.27}$$

and we note that we have already defined the Rossby number $Ro = U/(\Omega L)$, and the prefactor of the diffusive term is reminiscent of the Ekman number, $E = \nu/(\Omega L^2)$, but with the kinematic viscosity (a kind of "momentum diffusivity") replaced by the magnetic diffusivity. Thus we introduce the magnetic Prandtl number, $Pm = \nu/\eta$, the ratio of these two diffusivities and a material property of the fluid, and so we have (dropping the primes on dimensionless variables)

$$\frac{\partial \mathbf{B}}{\partial t} = Ro \nabla \times (\mathbf{u} \times \mathbf{B}) + \frac{E}{Pm} \nabla^2 \mathbf{B} \tag{2.28}$$

We now have four independent dimensionless groups, including those from the hydrodynamic case above: Ro, E, Γ, and Pm. We note that Re is another possible group, which can be written in terms of Ro and E, and that we have retained the geometrical factor Γ. The new dimensionless group, Pm, defined in terms of two material properties of the fluid, takes into account the fact that the electromagnetic

properties of the fluid are now important, in addition to its viscosity. For liquid metals, including liquid sodium and the liquid iron of Earth's core, $Pm \sim 10^{-5}$. We note that B_0 doesn't appear in this group; $\mathbf{B}$ appears once in each term in the induction equation, so any scaling factors for it drop out. To get a dimensionless group including B_0, we must turn to the hydromagnetic Navier-Stokes equation. Again putting in the dimensionless parameters, and dividing through by a factor of ΩU, we have (again dropping primes)

$$\frac{\partial \mathbf{u}}{\partial t} + \frac{U}{\Omega L}(\mathbf{u} \cdot \nabla)\mathbf{u} = -\nabla P + \frac{\nu}{\Omega L^2}\nabla^2 \mathbf{u} - 2\boldsymbol{\Omega} \times \mathbf{u} + \frac{B_0^2}{\rho \mu_0 \Omega L U}(\nabla \times \mathbf{B}) \times \mathbf{B} \quad (2.29)$$

and we see that we now have a dimensionless group containing B_0. There are many different possible choices for the new group; here we use the Lundquist number, given by $S = B_0 L/(\eta\sqrt{\rho\mu_0})$, which gives the ratio of the typical time scale of magnetic waves (specifically, Alfven waves) to the typical decay constant of them. The larger the value of S, the more persistent are magnetic waves in the system. Using S along with the other defined dimensionless groups, the Navier-Stokes equation becomes

$$\frac{\partial \mathbf{u}}{\partial t} + Ro(\mathbf{u} \cdot \nabla)\mathbf{u} = -\nabla P + E\nabla^2 \mathbf{u} - 2\boldsymbol{\Omega} \times \mathbf{u} + \frac{S^2 E^2}{Pm^2 Ro}(\nabla \times \mathbf{B}) \times \mathbf{B} \quad (2.30)$$

As noted above, dimensionless parameters allow comparison of observational, experimental, and computational results. The definitions and values of some dimensionless parameters relevant to the experiments and simulations to be discussed can be found in Table 2.2.2. Of particular interest in dynamo studies are the Reynolds

number, $\mathrm{Re} = UL/\nu$, and the magnetic Reynolds number, $\mathrm{Rm} = UL/\eta$. Here U and L represent velocity and length scales of the flow, while ν and η are the kinematic viscosity and magnetic diffusivity, respectively. The Reynolds number characterizes the presence and strength of turbulence in the flow. Above some critical value for Re, a flow will transition from laminar flow to turbulence, and above this value a larger Re implies stronger turbulence. Re can also be viewed as a ratio between inertial forces (causing advection and vortex stretching in the flow) and viscous forces (smoothing out variations in velocity). Similarly the magnetic Reynolds number, Rm, can be viewed as the ratio between advection of the magnetic field, tending to strengthen it via stretching of magnetic field lines, and dissipation of the field via diffusion due to resistive losses. The higher the Rm of a flow, the more likely dynamo action is to occur. For a given flow that is capable of dynamo action, a self-sustaining field will arise if Rm exceeds some critical value. In general this critical value is unknown, however, so experiments simply try to maximize it, and the estimated values for astronomical bodies provide some guidance as to what values may be necessary in a given configuration. Also, since rotation is often an important ingredient in both planetary dynamos and in experiments, the Ekman number $\mathrm{E} = \nu/(\Omega L^2)$ is relevant. This parameter quantifies the relative strength of viscous and rotational effects, and also sets the size of the Ekman boundary layer, which scales as $\mathrm{E}^{1/2}$.

Experiments and simulations can reach Rm values comparable to those of magnetized planetary bodies, consistent with the fact that dynamos have been realized in both experiments and simulations. While experiments can also reach realistic

Parameter	Symbol	Definition	Experiments	Simulations	Earth's Outer Core
Magnetic Prandtl number	Pm	ν/η	$< 10^{-5}$	$> 10^{-3}$	10^{-5}
Reynolds number	Re	UL/ν	$< 10^{8}$	$< 10^{6}$	10^{8}
Magnetic Reynolds number	Rm	UL/η	$< 10^{3}$	$< 10^{4}$	300-1000
Rossby number	Ro	$\Delta\Omega/\Omega$	$> 10^{-5}$	$> 10^{-5}$	10^{-5}
Ekman number	E	$\nu/\Omega L^2$	$> 10^{-8}$	$> 10^{-6}$	10^{-14}

Table 2.3: Dimensionless Parameters. Typical values for experiments and simulations, along with estimated values for the Earth's core. Values for Earth's core from [6].

values of Re, simulations cannot resolve the wide range of length and time scales needed to capture such turbulent flows, and thus simulations generally introduce unrealistically large viscosities in order to suppress turbulence and render the flow amenable to simulation (see Table 2.2.2). Finally, in the case of the Ekman number, astrophysical bodies often exhibit values well beyond the range of both experiments and simulations (though again experiments can go to lower values than simulations and thus get closer to values typical of planetary and stellar bodies).

Another set of dimensionless parameters involves the strength of the magnetic field. In studies of kinematic dynamos, where the background magnetic field is generally assumed to be negligible, such parameters will not be relevant. However, such parameters are important for characterizing dynamo systems once a magnetic field has been established. They may also be relevant to the description of subcritical

dynamos, for which an initial finite field strength is required for dynamo action to occur, though no external field is required to sustain the dynamo action once it is established. Since to date dynamos have only been achieved under a limited number of laboratory settings, systems that have relatively strong external applied fields are also often used to study hydromagnetic processes. Dimensionless parameters relevant to such studies include the Elsasser number and the interaction parameter. The Elsasser number $\Lambda = B_0^2/(\Omega\mu_0\rho\eta)$ measures the ratio of Lorentz to Coriolis forces; here μ_0 is the permeability of free space, ρ is the fluid density, B_0 is the applied magnetic field, and the other symbols are as above. It thus quantifies the relative importance of the magnetic field and overall system rotation in influencing the fluid flow. The interaction parameter $\mathrm{N} = \sigma L B_0^2/\rho U$, where σ is the conductivity of the fluid, provides the ratio of Lorentz forces to inertial forces in the system. For small N, Lorentz forces do not appreciably affect the flow, while for large N the Lorentz forces can significantly modify the flow.

2.2.3 Past Work: Theory and Simulations

Numerical simulations complement the observational and experimental work detailed above, providing flexibility in parameters as well as detailed information about the entire system. Motivated by observational and experimental results, simulations have shed light on various processes that may be at work in those systems. They have, in turn, also motivated new experimental studies. Much work has been done in numerical studies relevant to the observations and experiments described

above, including simulations of models of the geodynamo and direct numerical simulations of spherical Couette flow. This includes work on both hydrodynamic and hydromagnetic phenomena in spherical Couette, as well as studies of dynamo action in this and related geometries. [51] We first review hydrodynamic studies of spherical Couette flow, in which no magnetic field is present, before moving on to the magnetized case. Finally we close this section with a discussion of some dynamo studies, and their relevance for experiments.

For the case of hydromagnetic phenomena, a number of studies have addressed various aspects of magnetic spherical Couette flow. Starting with weak fields, the introduction of magnetic fields generally modifies the Stewartson layer (in the case of rapid overall rotation) or the equatorial jet (in the case of outer stationary or slow outer rotation); as the applied field gets stronger, it can eventually dominate rotational effects, with field lines structuring the flow. As in the non-magnetic case, the axisymmetric base state was studied analytically [52], as well as numerically [53–57]. A discussion of a number of recent results can be found in Chp. 7 of Rüdiger et al. (2013) and in Wei et al. (2012). For the case of an applied field that is axisymmetric about the rotation axis of the spheres, the fluid is divided into regions magnetically coupled to either one or both of the spheres (see e.g. Hollerbach and Skinner (2001)). As in the hydrodynamic case, jets and free shear layers can appear to accommodate the adjustment of the fluid rotation rate between these various regions.

When rotation is strong, the presence of a magnetic field can alter the Stewartson layer. In strong magnetic fields, free shear layers called Shercliff layers tend

to form along magnetic field lines, and Ekman layers are modified by the magnetic field to become what are called Hartmann layers (see e.g. Rüdiger et al. 2013). Starchenko (1998) performed an asymptotic study of magnetic spherical Couette with an axial applied field, finding that a Shercliff layer formed at the tangent cylinder. He also considered a dipolar applied field, which can be made sufficiently strong to produce two rigidly rotating regions, with the shear layer between them following the field lines that are tangent to the outer sphere at its equator. Here both spheres were insulating.

In the case of conducting spheres, a similar set-up can result in super-rotation. Starchenko (1997) and Dormy et al. (1998, 2002) numerically found a super-rotating jet (the fluid rotates faster than the inner sphere) in the case of a stationary outer sphere with a conducting inner boundary and an imposed dipolar field, while insulating boundaries gave results consistent with previous asymptotic findings. Hollerbach [58] studied how varying the imposed field geometry and the boundary conditions (insulating or conducting) could give rise to super- or counter- rotating jets.

Hollerbach and Skinner [56] found that for the case of a stationary outer sphere and a strong axial field that stronger magnetic field stabilizes flow: the shear layer goes unstable to nonaxisymmetric disturbances at higher and higher Re. Wei and Hollerbach [59] also considered spherical Couette flow with outer stationary and with overall rotation, with or without an axial magnetic field, and studied the stability of Stewartson (without an applied field, but with overall rotation) and Shercliff (with an applied field) layers. They found that the instabilities of the Shercliff layer were symmetric about the solid body case (that is, inner sphere sub- and super-rotation

behaved in the same way), while as noted above the Stewartson layer instabilities are asymmetric about this case. By considering the mixed case (overall rotation with an applied field), they showed that these two different cases are smoothly connected. For a useful overview of this work see also [51].

Gissinger et al. [60] investigated instabilites of magnetized spherical Couette flow for a variety of Ro, imposed fields, and magnetic boundary conditions. They found that an applied field can suppress hydrodynamic instabilities of the Stewartson layer or of the equatorial jet, but can also introduce new instabilities, associated either with disruption of the axisymmetry of the meridional return flow or with the Shercliff layer going unstable to nonaxisymmetric modes. Figueroa et al. [61] studied spherical Couette flow in a dipolar field (motivated by the DTS experiment), finding that fluctuations in the magnetic field had most of their energy located near the inner sphere (where the dipolar field is strongest), but are due to velocity fluctuations that originate in the outer boundary layer. These velocity fluctuations originate in two coupled instabilities: a high-latitude Bödewadt-type boundary layer instability and a secondary non-axisymmetric instability of a centripetal jet near the equator of the outer sphere. Bödewadt-type boundary layers form between rigidly rotating flows and a stationary (or more slowly rotating) boundary, resulting in inflow along the boundary and outflow into the fluid bulk along the axis of rotation. This is an example of an active boundary layer, where the boundary flow set up by the motion of the bulk fluid has a significant back-reaction on the bulk flow. [62] Generally, the introduction of magnetic fields provides new ways to both stabilize and destabilize the equatorial jets and Stewartson layers found in the non-magnetic

case. In addition, applied magnetic fields can lead to the formation of flow structures with no analog in the hydrodynamic case, and these structures can in turn develop their own instabilities.

There have also been numerical investigations of dynamo action in spherical Couette flow. One type of simulation is the kinematic dynamo, which ignores the back reaction of the magnetic field on the flow. In these simulations, the flow of a conducting fluid in spherical Couette is calculated first. Then this flow pattern is used in the magnetic induction equation to determine if there are any growing magnetic fields, which is a sign of dynamo action.

In the kinematic dynamo, a larger aspect ratio (r_o/r_i) and conducting boundary layers favor dynamo action (Wei et al. 2012). The similar case of the kinematic dynamo in a full-sphere (i.e. no inner sphere), but with boundary conditions that mimic the tangent cylinder flow of spherical Couette (polar caps that rotate at a different rate from the rest of the spherical boundary), was studied by Schaeffer and Cardin. [63] Using a quasi-geostrophic model allowed them to reach very low Ekman number (10^{-8}), and they considered the case of low Pm (resulting in a scale separation between the magnetic and velocity fields, and making the results relevant to liquid metal experiments and planetary cores). The kinematic dynamo found was interpreted as an $\alpha - \omega$ type, with differential rotation providing the ω effect and Rossby waves (which are instabilities of the internal shear layer) providing the α effect.

In addition to kinematic dynamos, nonlinear dynamos have also been studied, in which the back reaction of the magnetic field generated by dynamo action onto

the fluid flow is included. Guervilly and Cardin [39] found that dynamo action was achieved in spherical Couette flow when non-axisymmetric hydrodynamical instabilities were excited and Rm was sufficiently high. For the case of outer stationary, the critical Rm was of the order of a few thousand, with its value increasing with increasing Re. Specifically, the critical value of Pm was found to be 1. With outer rotation, the critical Pm was reduced by a factor of two (indicating overall rotation is more favorable for dynamo action), and for intermediate values of rotation (E = 10^{-3}), a favorable window for dynamo action was found, with a critical Rm of 300. The authors speculate that this may be due to an enhanced shear layer around the inner core, which however becomes unstable at lower E, eliminating this favorable regime for faster rotation. They also looked at the effect of ferromagnetic boundary conditions, finding minimal impact on the dynamo threshold though the strength of the saturated magnetic field above the dynamo threshold was enhanced in the ferromagnetic regions. These studies can offer hints regarding what set-ups may favor dynamo action, including that inner conducting boundaries and large aspect ratios may be more favorable to dynamo action (Wei et al. 2012).

The phenomena of intermittency near the onset of dynamo action has been investigated numerically by Raynaud and Dormy. [64] They found intermittency in the magnetic field near the dynamo threshold for a variety of boundary conditions (both spheres insulating, inner sphere conducting, and both ferromagnetic), with the intermittency eventually going away when the system is sufficiently above the dynamo threshold. This work may offer some guidance in the analysis of states observed in 3 m with bursts of magnetic field enhancement.

Finally, a comparison of smooth and rough inner boundaries for kinematic spherical Couette dynamos was made by Finke and Tilgner. [65] They considered the case of outer stationary, with $r_i/r_o = 1/3$, and compared the case of flow driven by a smooth inner sphere with no-slip boundary conditions and the case of flow driven by a volume force near the inner sphere (to simulate a rough inner sphere surface). The case of a rough inner sphere results in a reduction of the critical inner rotation rate for dynamo action by a factor of 10. This case also results in a thicker boundary layer and equatorial jet, which also make dynamo action somewhat more favorable. This work is of particular interest in future plans for roughening the inner sphere of 3 m via the attachment of baffles, thus increasing the coupling of the inner sphere with the bulk fluid and increasing the strength of the equatorial jet off the inner sphere and associated poloidal flows.

2.2.4 Past Work: Magnetized Spherical Couette Flow and Dynamo Experiments

In this section we describe some of the previous work done on magnetized spherical Couette, as well as dynamo experiments.

In trying to understand the geodynamo in particular, a class of experimental and numerical studies have focused on spherical Couette flow (see Chp. 7 of Rüdiger et al. 2013 for an excellent overview). [66] This consists of flow in the space between an outer bounding spherical shell and a concentric inner sphere of smaller diameter. Flow is driven by differential rotation between the inner and outer spheres. The

system can be characterized by the difference in inner and outer rotation rates $\Delta\Omega$ and, if the outer sphere is rotating, by the overall system rotation Ω (i.e. the outer sphere rotation rate). Such systems are geophysically relevant, having a similar geometry to the Earth's core, especially if they approximately match the inner-to-outer core radius ratio of 0.35. While not capturing all aspects of the geodynamo, such systems are relatively simple models of dynamo action, providing a straightforward way to achieve the differential rotation that is a key ingredient of many dynamo mechanisms (see e.g. Wei et al. 2012).

A significant difference between flow in Earth's core and such a set-up is the driving of the flow. Earth's core flows (including any differential rotation contributing to dynamo action) are believed to be driven primarily by a combination of compositional and thermal convection, with rotational, and possibly precessional, effects playing a significant role. In spherical Couette flows, on the other hand, a shear flow is driven by differential rotation imposed at the boundaries. Thus the angular momentum transport between the two spheres, rather than heat and chemical transport, is the driver of the flow.

While thermal convection can be used to drive flows in experimental devices, these flows tend to be less vigorous than shear flows, as measured by the achievable Re and Rm. Moreover, if hydromagnetic phenomena are to be investigated, the working fluid must be a conductor, and a good electrical conductor is desirable to achieve a large Rm. Thus experiments generally make use of a liquid metal, like sodium or gallium. In fact, liquid sodium is the best liquid conductor usable in such experiments, but with high electrical conductivity comes high thermal conductivity.

Thus when a thermal gradient is used to drive flows in liquid sodium, the induced flows are relatively weak, resulting in a low Re and thus, since Rm = RePm, a relatively low Rm (at least compared to shear-driven sodium flows). For instance, the rotating convection experiment described in Shew and Lathrop (2005) achieved an Re of ~ 40000 based on zonal flows in the liquid sodium; later, it was reconfigured to be a mechanically driven spherical Couette device, achieving Re of $\sim 10^6$ (Kelley 2009). Spherical-Couette devices using liquid sodium can thus achieve turbulent hydromagnetic flows with significant rotational effects in an Earth-like geometry. A similar experimental set-up is that of a spherical vessel of fluid with flow driven by impellers; while less Earth-like, the impellers allow more vigorous flow to be driven as compared to the smooth-walled boundaries of spherical Couette devices.

A number of liquid sodium devices have been implemented with a spherical geometry. The Madison dynamo experiment (MDE) is an example of an impeller-driven flow [67] while the Derviche Tourneur Sodium (DTS) experiment in Grenoble is a spherical Couette device with a ferromagnetic inner sphere [68, 69]. At the University of Maryland a series of liquid sodium devices have been constructed, including three spherical vessels ranging in size from 30 cm to 3 m. The two current sodium experiments are both spherical Couette devices, 60 cm and 3 m in diameter, and magnetic fields can be applied to the fluid volume using external coils.

In spherical geometries, we note that both magnetic and velocity fields are commonly described using vector spherical harmonics to decompose the fields into poloidal and toroidal components [27]. This can always be done for magnetic fields which are always divergence-free, and can also be done for the velocity field of an

incompressible flow - such as that found in liquid metal experiments. The toroidal component of the magnetic field has no radial component, and does not extend out of the conductor; thus for measurements outside the Earth's core (or outside the fluid volume of an experiment), only the poloidal component of the field can be measured, which can be written as the gradient of a scalar field (assuming no other current sources). Models of Earth's field outside its core are often expanded in terms of spherical harmonics, with the coefficients in the expansion (one for each harmonic, identified by degree l and order m) referred to as Gauss coefficients (after Gauss, the first to represent Earth's field in this manner [17]. Moreover, descriptions of the dynamo mechanism are often conceptualized in terms of the conversion of poloidal field into toroidal field (the ω effect) and of toroidal field into poloidal field (the α effect) via fluid flow.

Below we first review some of the results from previous successful dynamo experiments (all in non-spherical geometry), along with some results from MDE, which while not a dynamo shares many characteristics with the VKS experiment (the only successful dynamo in an open geometry). Then we review some results from the DTS experiment, a liquid sodium device modeled on Earth's core and having a strong imposed dipolar field. This section closes with discussion of the Maryland spherical Couette experiments.

While the Maryland devices and DTS are modeled on Earth's core, MDE follows in the tradition of the Riga and Karlsruhe dynamos in being based on a kinematic dynamo (Riga: the Ponomarenko flow [70]; Karslruhe: G.O Roberts flow [71]). While the mean flow of the device approximately models a laminar kinematic

dynamo, turbulent fluctuations are always present as well. In the Riga and Karlsruhe dynamos, turbulent fluctuations were limited in size by the diameter of the pipes used in constraining the flow, thus separating the scale of the turbulent eddies from the system size over which the dynamo acts. MDE, on the other hand, has an open geometry like VKS and the Maryland devices where turbulent fluctuations can be present up to the system size. Such a geometry is more astrophysically relevant, since natural bodies generally have unconstrained flows in simply-connected regions more akin to those of MDE or VKS than the Riga or Karlsruhe dynamos [67]. The lack of scale separation also means, however, that the predictions of laminar kinematic dynamo theory, while still a potentially helpful guide, are no longer reliable.

The Madison dynamo experiment (MDE) has a very similar driving set-up to that of the VKS experiment, but in a spherical rather than cylindrical container. The experiment consists of a 1m diameter spherical shell filled with liquid sodium, driven by two impellers. The impellers have a common axis, mounted on shafts entering the container from the two poles of the experiment. Two sets of coil pairs, one coaxial with the impellers, and one perpendicular to the axis, can be used to apply a magnetic field of dipolar or quadrupolar symmetry, either parallel to the impeller rotation axis or perpendicular to it. Unlike the VKS experiment, MDE does not achieve dynamo action, including when using ferromagnetic impellers [72]. While no dynamo was seen, a variety of phenomena involving the interaction of turbulent flow with magnetic fields have been observed and quantified.

As noted above, the set-up of MDE was in part motivated by a kinematic dynamo for the spherical geometry. This flow consists of counter-rotating toroidal

flows in the two hemispheres (driven by the counter-rotating impellers), as well as poloidal rolls consisting of outflow from the equatorial regions between the impellers towards the poles (again driven by the impellers) and a return flow along the outer boundary (Nornberg et al. 2006). This double-vortex flow results in a kinematic dynamo in the laminar case [73], with feedback resulting in a transverse dipole (i.e. a dipole oriented perpendicular to the axis defined by the impeller shafts). Using liquid sodium, with the resulting small Pm, however, means that the actual experiment will be highly turbulent, with Re $\sim 10^7$ and turbulent fluctuations up to $\sim$20% of the mean [74].

While the mean flow of MDE is expected to approximate that of the laminar kinematic dynamo, these turbulent fluctuations in the experiment can have a number of effects. Nornberg et al. [67] follow a mean-field approach in separating the magnetic and velocity fields into their mean and fluctuating components and focusing on the mean field and the net effect of the fluctuating components on it (see e.g. [75]). The expected dynamics are a combination of those due to the mean, axisymmetric flow (approximating the laminar kinematic dynamo) and the net effect of the fluctuations in the velocity and magnetic fields (due to turbulence). Correlated fluctuations in the magnetic and velocity fields can result in coherent generation of magnetic field (referred to as the α effect, first experimentally observed by Steenbeck et al. [76]). Tangling of the magnetic field lines by turbulent eddies can result in an increase in dissipation of magnetic field in the system, which can be viewed as a turbulent enhancement of the system's magnetic diffusivity (termed the β effect). Finally, gradients in the amount of turbulence can result in flux expulsion from

regions of higher turbulence (the γ effect).

In the parameter regimes studied, the MDE experiment does not achieve dynamo action, but by applying magnetic fields in a number of different geometries, the effects of turbulent fluctuations have been investigated. For the case of an axial applied field, in addition to the expected induced field due to the mean flow (axisymmetric $l = 3$ and $l = 5$ modes), an axial dipole is also seen [74]. This cannot be due to the interaction of the axisymmetric mean flow with the axisymmetric applied field (by well-known symmetry arguments, see [77]), so it is argued that it must be due to a turbulent EMF which breaks the symmetry of the system.

In addition to the liquid sodium experiment, the Madison group has an identical-scale water experiment, which when run at an appropriate temperature (40°C), approximately matches the kinematic properties of liquid sodium (see e.g. [67]). In the water experiment Laser Doppler velocimetry (LDV) measurements of the velocity were taken (which are not possible in opaque liquid sodium), allowing the mean flow field in the sodium experiment to be predicted. By comparing the induced magnetic field in the liquid sodium to the field expected by the action of this mean flow field on the applied magnetic field, Spence et al. [78] infer the presence of electrical currents in the experiment due to the turbulent EMF. This current in turn produces poloidal (which is primarily dipolar) and toroidal field that is opposed to the primary field induced by the mean flow; the system exhibits turbulent diamagnetism. Kaplan et al. [79] report on the results of installing equatorial baffles in MDE, resulting in a reduction of the global β effect in the experiment. Further improvement in reducing the turbulent resistivity were reported in [80], though the system was still below the

threshold for a dynamo.

In addition to these relatively steady effects, intermittent bursts of magnetic field have also been observed in MDE (Nornberg et al. 2006a). When an axial magnetic field is applied to the experiment, a fluctuating amount of energy is observed in the transverse dipole, which is the least-damped magnetic eigenmode predicted by laminar kinematic dynamo theory. The orientation of the dipole within the equatorial plane of the experiment is random, so on average the induced magnetic field is axisymmetric. Also, the distribution of the strength of magnetic fluctuations diverges from a Gaussian distribution due to these large bursts, serving as another indication that the bursts are not simply due to noise in the system. The strength of the Lorentz forces due to the bursting field is at most comparable to those due to the applied field, so the interaction parameter remains low ($N \sim 0.01$), and the effect of these forces is minimal.

The authors propose several possible explanations for these bursts. Turbulent velocity fluctuations could lead to a locally higher Rm, resulting in it temporarily exceeding the critical Rm for this least-damped eigenmode. Alternatively, the turbulent fluctuations could alter the overall shape of the flow, making it more favorable to this eigenmode, effectively reducing its critical Rm below the experiment's Rm (again, temporarily). In either case, the mode would start growing, and there would be a burst of magnetic field in the form of a transverse dipole, which would decay away once the favorable turbulent fluctuations had dissipated. Another possibility is that if at small scales the kinetic helicity of eddies becomes strong enough, the current produced by their interaction with the applied field could result in the

bursts. In summary, the authors argue that for a turbulent dynamo the transition from non-dynamo to dynamo states will be marked not by a smooth transition from a decaying to a growing magnetic eigenmode (as in laminar kinematic dynamos), but rather by intermittent bursts of magnetic field.

The DTS experiment was designed to study the magnetostrophic regime relevant to the Earth's core (see e.g. [81]). In this regime, the Coriolis and Lorentz forces dominate viscous forces. Such a regime is characteristic of rapidly-rotating systems with strong magnetic fields. The DTS experiment has a 42 cm outer diameter sphere, while the 14.8 cm inner sphere has a copper surface with an internal permanent magnet, so that a dipolar field is applied to the liquid sodium that fills the gap between the inner sphere and the outer spherical shell. The dipole is oriented along the axis of rotation of the spheres. The inner and outer spheres can be rotated independently, driving a variety of flows that are significantly modified from the hydrodynamic case by the presence of the relatively strong field of the inner sphere.

In terms of dimensionless parameters, such a system has a small Ekman number (so rotational effects dominate viscous ones) and an Elsasser number $\Lambda \sim$O(1), so that the Coriolis and Lorentz forces are of comparable strength. Although laboratory experiments cannot reach Ekman numbers comparable to those found in planets and stars, they are capable of reaching regimes of rapid rotation that are computationally inaccessible. Since a dynamo has not yet been demonstrated in the spherical geometry, however, in order to reach an Elsasser number of order $\sim$ O(1), some other magnetic field must be applied to the fluid. In the case of DTS, the

inner sphere is ferromagnetic, applying a dipolar field of fixed strength. Given this geometry, a variety of force balances are present in the experiment, ranging from a magnetically-dominated one near the inner sphere, to a rotationally dominated one near the outer sphere (see e.g. [68]). For instance, magneto-coriolis waves have also been observed, where both rotational effects (via the Coriolis force) and magnetic effects result in the fluid supporting novel wave modes [82]. A similar phenomenon, magnetic Archimedes Coriolis (MAC) waves — where buoyancy effects, in addition to rotational and magnetic ones, are important — may play a significant role in the dynamics of Earth's core. [83, 84]

Another such flow involves the super-rotation of the flow as compared to the inner sphere, so that the flow velocity exceeds that of both system boundaries. [85] Super-rotation was first found in numerical simulations [53, 86], and was later found in the DTS experiment [68, 69, 85]. In [68] and [69], the azimuthal angular velocities of the flow were inferred from electric potential measurements at the surface of the outer sphere, and interpreted as revealing a strong super-rotation of the liquid sodium in the equatorial region.

While super-rotation was found, consistent with the previous numerical predictions, there were also notable differences between the numerical model and the experimental results. In particular, the experimental variation of the electric potential with latitude did not match that of the numerical simulation, and oscillatory motion near the equator of the outer sphere, seen using ultrasound Doppler velocimetry (UDV), did not match up with the steady result in numerics. The oscillations were interpreted as due to an instability of the super-rotating region.

Intuitively, this phenomenon can be understood in terms of the electric currents in the system and the geometry of the applied field lines (see discussion of simulation results below, and [58]). Generally the electric currents follow the field lines, thus generating no Lorentz force on the fluid. In boundary layers the electric currents cross field lines, generating Lorentz forces that balance the viscous forces. Near the equator of the experiment, however, given the dipole geometry of the applied field, if large enough currents are flowing they are forced to cross the magnetic field lines here. The Lorentz forces that result allow the inner sphere to act like a magnetic propeller, grabbing on to the fluid and forcing it to spin with it rather than with the outer sphere.

These forces can become so large that they overcompensate for the viscous forces due to the differential rotation of the inner with the outer sphere, and result in the acceleration of the fluid in this region to angular velocities that exceed that of the inner sphere. In Brito et al. (2011), UDV measurements confirmed the presence of super-rotating jets in DTS for the case of a stationary outer sphere. They also show that the electric potential measurements are somewhat difficult to interpret and are not always a good guide to the azimuthal velocities. The phenomenon of super-rotation is an interesting and unusual hydromagnetic phenomenon; numerical models match well features of the experiment that depend only on dimensionless parameters that do not include diffusivities [85]. Thus comparison of experimental results with numerical models allows elucidation of the limits of linear models; a similar explanation (involving the lack of strong dependence on diffusivities) has been proposed to explain why Earth-like geodynamo models do surprisingly well. [87]

Another experimental result from DTS is of particular interest for dynamo studies. Cabanes et al. [88] report on measurements of the α and β effects, and note that the β effect due to small-scale turbulent fluctuations is negative in the interior of the experiment, and positive closer to the outer sphere. Thus, the turbulent fluctuations near the inner sphere reduce the effective magnetic diffusivity, implying that turbulence could be a contributing factor to dynamo action, as opposed to a hindrance (as it has often seemed in past experiments). Indeed, the authors speculate that if the magnitude of this negative β effect were to grow large enough, it could promote dynamo action. As reported in another paper [89], the ω effect is present in the rotationally dominated outer region, which is another possible ingredient of dynamo action.

In previous work [90] with the 3 m experiment, at least twelve distinct non-dynamo states have been identified, with the states depending on Ro as in the case of the water experiments (as expected for non-magnetic states). In addition, a power peak at a specific Ro has been identified. For the case of magnetized flow, a dipolar magnetic field is applied with a large electromagnet located around the experiment's equator (or, in more recent work, with an array of two magnets - see section3.2.2). The strength of the applied magnetic field serves as another parameter that can be varied, in addition to varying Ro and Re, providing a large parameter space to explore. Of course, if a self-sustaining dynamo (a prime motivation for the experiment) were to be obtained, no applied field would be necessary (beyond some initial seed field, such as an ambient field or one due to random fluctuations).

A useful conceptual framework for evaluating the prospects for dynamo action

in the 3 m device is the α-ω dynamo (Parker 1955). In this model, differential rotation converts poloidal field into (more intense) toriodal field (the ω effect), and then toroidal field is converted back into poloidal field via the so-called α effect, thus strengthening the original field and closing the dynamo feedback loop. During magnetized experiments in 3 m, the dipolar field applied by the external magnet provides a seed poloidal field. Any toroidal field present in the experiment is the result of the ω effect due to differential rotation in the fluid acting on the applied field. This toroidal field does not extend outside the experiment, however, and so can only be measured by a probe within the fluid volume. In order to have a diagnostic of the toroidal field, some measurements of magnetic field inside the flow have been taken at a single point using an inserted Hall probe (in addition to the external field measurements made by an array of Hall probes just outside the experiment). From these measurements it is seen that the azimuthal field is significantly stronger than the local applied field, which has radial and vertical components. This is interpreted as a sign of the ω effect operating in the experiment, converting poloidal magnetic field (in this the dipolar applied field) into toroidal (i.e. azimuthal) magnetic field. While the strong differential rotation of the flow for some Ro supplies significant ω effect, so far no states have been found with strong enough α effect to give self-sustaining dynamo action. Finally, looking at global magnetic field measurements, steady dipole gain of up to $\sim 20\%$ has been observed in the experiment, with bursts of amplifaction of up to $\sim 40\%$ though these states require an external applied field, and thus are not dynamo states. [90]

2.3 Analysis Background

In this section we look at the theoretical background for two of the main techniques used in extracting information from our instruments. For the magnetic data, where we have an array of Hall probes around the exterior of the experiments (see Chapter 3 for more details), we use Gauss coefficients to characterize the global magnetic field patterns, and in turn infer information about the possible global velocity patterns present. For the air experiments in the 60 cm experiment (and hopefully in the future the sodium experiments), we use the splittings of acoustic modes of the experimental cavity to infer information about the global pattern of zonal flow.

2.3.1 Spherical Harmonics

Three experiments in the University of Maryland Geodynamo lab have used the approach of fitting the induced field in an experiment in a spherical shell to vector spherical harmonics in order to obtain a global model of the field. This is motivated by the use of Gauss coefficients in studies of Earth's magnetic field. The basic idea is to have an array of probes around the experiment measuring the induced field in the system (by calibrating out any contribution due to the applied field) and then to do a least squares fit of a (truncated) expansion of vector spherical harmonics to these measurements. In this way a series of point measurements of one component of the magnetic field can be used to infer the global pattern of the field; a limitation of this approach is that we are not sensitive to small scale structures. Since the

measurements are taken outside the fluid volume, there will be some filtering due to the more rapid fall-off with distance of higher order magnetic moments, so such higher-order structures will also have less of an effect on the probe measurements. The 30 cm and 60 cm experiments used arrays of identical design (the one for 60 cm being scaled up appropriately), containing 30 Hall probes mounted around the experiments in the laboratory frame; the initial array for the 3 m experiment contained 31 Hall probes, mounted to the exterior surface of the vessel (and thus in the rotating frame). See Chapter 3 for more details regarding the experimental set-ups. Below, we provide an overview of the use of spherical harmonics and Gauss coefficients in representing magnetic measurements, following a similar discussion in section 2.3 of Kelley 2009 [91].

The basic idea in using the vector spherical harmonics is to represent the induced magnetic field as the gradient of a potential; this is a valid representation provided the measured field is due to currents interior to the experiment and not exterior to the array. Provided external fields (like those due to the magnets in producing the applied field, as well as the Earth's field and fields due to building structures) have been calibrated out, the magnetic field seen outside the experiment (where the array is located), obeys

$$\nabla \times \mathbf{B} = \mu \mathbf{J} + \epsilon_0 \frac{\partial \mathbf{E}}{\partial t} = 0 \tag{2.31}$$

where we have used the fact that in the region of the array there are no currents present, and have used the MHD approximation in neglecting the displacement

current. Since the curl of $\mathbf{B}$ is zero in this region, we can write it as the gradient of a potential,

$$\mathbf{B} = -\nabla\Phi \tag{2.32}$$

and taking the divergence of both sides, and using the fact that $\mathbf{B}$ is divergence-free, we have

$$\nabla^2\Phi = 0 \tag{2.33}$$

i.e. Laplace's equation. The solution of Laplace's equation in a spherical geometry are the scalar spherical harmonics. Expanding Φ in terms of the spherical harmonics, we have

$$\Phi(\mathbf{r}) = \sum_{l=0}^{\infty}\sum_{m=-l}^{l}(A_l r^l + B_l r^{-(l+1)})(a_m \cos m\phi + b_m \sin m\phi)P_l^m(\cos\theta). \tag{2.34}$$

where we have broken out the ϕ dependence of the scalar spherical harmonics, in order to make explicit the cosine and sine terms, with $Y_l^{mc} = \cos m\phi P_l^m(\cos\theta)$ and $Y_l^{ms} = \sin m\phi P_l^m(\cos\theta)$. Here the P_l^m are the generalized, Schmidt semi-normalized Legendre function (see [91] for further details). Next, we note that the field must go to zero at infinity (since we're representing only the field due to currents inside the experiment, all other fields assumed to have been calibrated out), so that we must have all A_l equal to zero. Also, we must have $B_0 = 0$, since it corresponds to a magnetic potential that falls off like $1/r$, and thus corresponds to a magnetic field that falls off like $1/r^2$ from its source, which corresponds to a magnetic monopole, the presence of which would violate the requirement that B be divergence-free.

Putting in these results and combining terms we have

$$\Phi(\mathbf{r}) = b\sum_{l=1}^{\infty}\sum_{m=-l}^{l}(g_l^{mc}\cos m\phi + g_l^{ms}\sin m\phi)(\frac{r}{b})^{-(l+1)}P_l^m(\cos\theta), \tag{2.35}$$

where the terms g_l^{mc} and g_l^{ms} are the so-called Gauss coefficients, b is the radius of the fluid volume (outside of which we assume there are no currents, which would act as sources of magnetic field), and we have used the Thus we have a representation for the magnetic potential, and thus (by taking the gradient) the field, outside the experiment, using scalar spherical harmonics.

The values of the coefficients g_l^{mc} and g_l^{ms} indicate how much contribution to the local magnetic field is due to their corresponding spherical harmonic, and so by using n measurements of magnetic field, we can fit up to n coefficients (in a least squares sense). Of course, better results are obtained by having more measurements of the magnetic field, and for 3 m we obtain 31 (or later, 33) measurements of the field, and use this to fit to 24 Gauss coefficients, corresponding to l running from 1 to 4 and m running from $-l$ to $+l$ for each value of l.

In addition to giving us a sense of the global field geometry, that is, whether it is mainly dipolar, quadrupolar, or higher order, the use of Gauss coefficients can aid in the identification of the geometry of waves and, through the use of selection rules, allow us to infer what velocity patterns could be present in the flow. In the case of waves, one previous result found with the 60 cm experiment, as noted above (see section 2.2.4), was the presence of strongly excited inertial modes in the system over a wide range of parameters. Since the inertial modes are characterized by a degree

l and order m, in addition to a frequency ω, they are easily identified by taking the power spectra of the Gauss coefficients, and looking for peaks in the frequency range $[0, 2\Omega]$ where Ω is the rotation rate of the vessel (or, more precisely, of the bulk of the fluid). For the case of waves with a definite azimuthal wave number m but no specific degree structure, the Gauss coefficient approach can still be helpful in identifying the m number, and in indicating whether the wave has a definite equatorial symmetry (symmetric or anti-symmetric).

In the use of selection rules to identify possible velocity modes, we follow the approach of Bullard and Gellman [27], as explicated in [91], and note that since the magnetic field is divergence-free, and the velocity field is assumed divergence-free (using the approximation of an incompressible fluid), both fields can be represented using a sum of poloidal and toroidal vector fields,

$$\mathbf{v} = \sum_{\alpha} (\mathbf{s}_\alpha + \mathbf{t}_\alpha), \tag{2.36}$$

and

$$\mathbf{B} = \sum_{\alpha} (\mathbf{S}_\beta + \mathbf{T}_\beta), \tag{2.37}$$

where the $\mathbf{t}_\alpha$, $\mathbf{T}_\beta$ are the toroidal vector spherical harmonics and the $\mathbf{s}_\alpha$, $\mathbf{S}_\beta$ are the poloidal vector spherical harmonics. Here we have introduced the convention of using lowercase letters for the velocity field representation ($\mathbf{t}_\alpha$, $\mathbf{s}_\alpha$) and uppercase letters for the magnetic field representation ($\mathbf{T}_\beta$,$\mathbf{S}_\beta$). The subscripts α and β stand in for the specific labels for the components, which are identified (like the scalar

spherical harmonics) by degree l and order m (with $0 \leq m \leq l$), and further labeled cosine or sine (in keeping all components real, also note that the $m = 0$ term counts as a cosine, with no corresponding sine component); another approach is in terms of complex exponentials, in which case instead of cosine and sine labels for the nonzero m terms, we use only l and m to label them, but with m running from $-l$ to $+l$ instead of from 0 to l. Also note that in either case, for each value of l there are a total of $2l + 1$ terms. The vector spherical harmonics can be defined as

$$\mathbf{T}_l^{mt} = \nabla \times T(r) Y_l^{mt}(\theta, \phi)\hat{\mathbf{r}} \tag{2.38}$$

and

$$\mathbf{S}_l^{mt} = \nabla \times \nabla \times S(r) Y_l^{mt}(\theta, \phi)\hat{\mathbf{r}} \tag{2.39}$$

where the superscript t in $\mathbf{T}_l^{mt}$, $\mathbf{S}_l^{mt}$, and Y_l^{mt} are all either s or c, denoting the cosine or sine component of the vector and scalar spherical harmonics, the Y_l^m being the scalar spherical harmonics, discussed above, and $T(r)$ and $S(r)$ are complete and orthogonal scalar function of r, with $\hat{\mathbf{r}}$ the unit radial vector. We note that since both the toroidal and poloidal terms are written in terms of a curl (or a curl of a curl), the resulting field will be divergence-free by construction. Besides the mathematical convenience of automatically satisfying the requirement that the fields be solenoidal, the use of an identical basis for both fields makes the use of selection rules relatively straightforward (if mathematically intensive). Here we assume the applied field geometry is known (as it is in the case of our experiments), and then for a given

induced field geometry, we can use selection rules to infer what possible flow velocity field geometries could result in the observed induction. While the field was always primarily dipolar (produced by two ring-shaped electromagnets with their shared axis aligned with the rotation axis of the experiment, and thus in a Helmoholtz pair-like configuration) for the 60 cm hydromagnetic experiments, in the case of the 3 m experiment, the field used was sometimes dipolar (produced either by a single electromagnet located around the equator, or by a pair of electromagnets in a similar configuration to the 60 cm magnets) and sometimes quadrupolar (with the pair of magnets, but with their produced fields being opposed rather than aligned). Also we note that the induced field can also act on the velocity field to result in further induced fields, quickly complicating the picture, but for the case of weak applied fields (i.e. Lorentz force term in the hydromagnetic Navier-Stokes equation being negligible compared to the dominant terms) such second-order effects can be neglected.

2.3.2 Acoustic Modes of Full Sphere and Spherical Shell

In this section we consider the calculation of acoustic modes in idealized models of our experiments, which illustrate the basic properties of the modes and yield approximations to their frequencies. This will lay the groundwork for the inference of zonal flows from frequency splittings of acoustic modes, discussed further in section 2.3.3. Since acoustic waves are just pressure waves in the fluid, we start with the wave equation for the pressure of a isentropic fluid (since we're assuming the fluid

is in approximate equilibrium, or at least steady state; here we follow the discussion in Appendix A of [92]), which is

$$\frac{\partial^2 P(\mathbf{r},t)}{\partial t^2} = c^2 \nabla^2 P(\mathbf{r},t). \tag{2.40}$$

Plugging in an ansatz of $P(\mathbf{r},t) = f(\mathbf{r})e^{-i\omega t}$, corresponding to oscillatory behavior, the above reduces to the Helmholtz equation for $f(\mathbf{r})$:

$$\nabla^2 f(\mathbf{r}) + k^2 f(\mathbf{r}) = 0 \tag{2.41}$$

where we have introduced the wavenumber k, given by $k = \omega/c$. For acoustic waves propagating in an infinite fluid, then, any frequency is allowed. Next we consider the case of waves propagating in a spherical cavity (a first rough approximation of our vessels). In this case, we must solve the Helmholtz equation in spherical coordinates, and subject to boundary conditions. Using the usual spherical coordinates $\mathbf{r} = (r,\theta,\phi)$, we note that the Helmholtz equation separates, so that $f(\mathbf{r}) = R(r)Q(\theta)\Phi(\phi)$. The solutions for $Q(\theta)$ and $\Phi(\phi)$ are, not surprisingly, the spherical harmonics $Y_l^m(\theta,\phi)$, while for $R(r)$ we have the spherical Bessel equation

$$\frac{\partial}{\partial r}[r^2 \frac{\partial}{\partial r} R(r)] = [l(l+1) - k^2 r^2] R(r), \tag{2.42}$$

and the solution for $R(r)$ is, up to a constant pre-factor, given by

$$R(r) = j_l(kr) + B n_l(kr), \tag{2.43}$$

where j_l and n_l are the order l spherical Bessel functions of the first and second kind, respectively. Boundary conditions are needed to fully specify the possible solutions. For the case of a full sphere, we require that the pressure be finite at $r = 0$, and thus we must have $B = 0$, since the n_l are singular at the origin. We also require that the radial derivative of the pressure vanish at the outer boundary, $\frac{\partial}{\partial r}P = 0$, so we must have $R'(r = r_o) = 0$, where the prime denotes a radial derivative and r_o is the radius of the cavity. Working in units where $r_o = 1$, this gives $j_l'(k) = 0$. This determines the allowable wavenumbers k, namely the zeros of the first derivative of the spherical Bessel function of the first kind. So, for each value of l, $l = 0, 1, 2, ...$ there are an (denumerably) infinite number of possible wavenumbers k, which we label in ascending order of k by $n = 0, 1, 2...$; n can be thought of as the number of radial nodes within the fluid volume. Each (n, l) pair will have a corresponding k, or equivalently, angular frequency ω_{nl} given by $\omega_{nl} = ck/r_o$, where c is the sound speed of the fluid, and r_o is the outer radius of the vessel. In our reports of experimental results, we usually work with the cyclic frequency f, given by $f = \omega/(2\pi)$. Also, as noted above, the frequency does not depend on m, and thus the $2l + 1$ modes of each (n, l) family are degenerate, sharing the same frequency for the case of spherical symmetry.

For the case of a spherical shell, that is an outer spherical boundary and an inner sphere (a closer approximation to our experiments, though still spherically symmetric), we return to equation 2.43, and note that since $r = 0$ is no longer in the fluid region, both kinds of Bessel functions can appear in $R(r)$. Instead of requiring regularity at the origin, we now have an inner boundary at $r = r_i$ with the

same boundary condition as the outer boundary, namely $\frac{\partial}{\partial r}P(r = r_i) = 0$. These two boundary conditions determine can be used to solve for B and k. Again working in units where $r_o = 1$, and defining $r_i = a$ in these units, we have

$$j_l'(ka) + Bn_l'(ka) = 0 \tag{2.44}$$

and

$$j_l'(k) + Bn_l'(k) = 0. \tag{2.45}$$

Multiplying the first equation by $n_l'(k)$ and the second by $n_l'(ka)$ and summing them, we can eliminate B, obtaining

$$j_l'(ka)n_l'(k) - j_l'(k)n_l'(ka) = 0, \tag{2.46}$$

and solving for B we have

$$B = -\frac{j_l'(k)}{n_l'(k)}(= -\frac{j_l'(ka)}{n_l'(ka)}). \tag{2.47}$$

The possible values of k for this case are then determined by equation 2.46, and for a given k the corresponding value of B is given by equation 2.47. We again label the modes corresponding to a given k by n, for $n = 0, 1, 2..$, with the k arranged in ascending order. The values of k can be found numerically, and then the corresponding mode frequency is again given by $\omega_{nl} = ck/r_o$. Here again the $2l + 1$ modes (corresponding to $m = -l, ..., 0, ...l$) are degenerate, since spherical

symmetry is still present (since we have neglected the presence of a shaft and other departures from spherical symmetry in the experiments). Thus, using the above approach, and plugging in the values of r_o, $a = r_i/r_o$, and c (see Table 2.1.2 for values relevant to the experiments), we can obtain approximate predictions for the mode frequencies.

2.3.3 Acoustic Velocimetry

In this section we provide some background on the techniques of helioseismology, along with the basics of it as applied to laboratory experiments, which we refer to as acoustic velocimetry. As noted in section 1.1.3 above, the field of helioseismology makes use of observations of the frequencies of acoustic modes of the sun, including the splittings of modes in the same (n,l) family but with different azimuthal wave number m, to infer properties of the solar interior, including the pattern of azimuthal flow. This approach relies on the fact that the frequencies of acoustic oscillations in the sun depend on the properties of the solar interior, and different modes reflect properties in different regions of the sun. While the measurement of oscillation frequencies has been important in validating and fine-tuning models of the solar interior [28], here we focus on the use of these measurements to infer azimuthal velocities as a function of position within the solar interior.

Assuming an adequate model of the expected frequencies for a non-rotating sun has been constructed, the oscillation frequency of a given mode ω_{nlm} can be written in terms of the non-rotating frequency ω_{nl0} (since the $m = 0$ mode is not

affected by the rotation to first order, while the rotation splits the non-zero m modes in the (n,l) family from the $m = 0$ mode) and the solar rotation profile $\Omega(r, \theta)$ as [28]

$$\omega_{nlm} = \omega_{nl0} + m \int_0^R \int_0^\pi K_{nlm}(r, \theta)\Omega(r, \theta) r dr d\theta, \tag{2.48}$$

where $K_{nlm}(r, \theta)$ is the sensitivity kernel of the given mode to the solar rotation profile. It is basically a weight function, giving the sensitivity of the mode frequency to flows in different parts of the meridional plane, and is calculated using the eigenfunction of the given mode in the non-rotating solar model. Since the dependence on r and θ of K_{nlm} will vary among modes, by combining observations of multiple mode splittings from the non-rotating case a picture of $\Omega(r, \theta)$ can be built up. In particular, for the case of the sun we note that high degree modes modes tend to be concentrated near the surface of the sun, while low degree modes probe deep into the solar interior. In particular, the turning point of a mode, that is the radius r_t (within the sun) at which the wave vector is horizontal, resulting in the wave turning back towards the surface, with the wave exponentially decaying in the region $r < r_t$, is given by [28]

$$r_t = \frac{c(r_t)\sqrt{l(l+1)}}{\omega}, \tag{2.49}$$

with this relationship holding for modes of high radial order, which many of the observed acoustic modes in the sun are. As can be seen in the above equation, r_t is small for low degree (small l) modes or high frequency modes, and is in fact zero for radial modes ($l = 0$). Since the speed of sound varies with depth in the sun,

this must also be taken into account, and $c(r_t)$ is the speed of sound at the turning point. By measuring the frequencies of modes of both low and high degrees, the sun can be probed at a variety of depths. In addition, high degree modes that have m close in value to l are concentrated around the equator.

Applying this to the case of laboratory experiments, if we can measure the mode frequencies for the stationary case, and develop a good model of the mode eigenfunctions, then we can use the above relation to perform an inverse problem: using the observed frequencies for a number of modes, and the calculated sensitivity kernels for them, we can infer the rotation profile $\Omega(r, \theta)$ of the experiment. See Chapter 5 below for more details on applying these techniques to experiments, and on the results obtained.

2.3.4 Previous Laboratory Results

In this section we review some results from previous acoustic investigations in laboratory experiments. Using the 30 cm experiment, a spherical Couette device with a fixed outer sphere and a rotating inner sphere, measurements were performed in air both of aoustic mode splittings and, using an anemometer, of the average azimuthal velocity at a number of locations within the fluid volume [92].

A speaker was used to excite acoustic modes in the system, by playing a chirp, and the acoustic signal was acquired on several microphones, with both the microphones and the speaker mounted on the outer sphere. In addition, an anemometer was inserted into the system to measure the azimuthal velocity of the fluid at several

different locations. Experiments were conducted for a variety of different inner rotation rates, and the splittings of 26 different acoustic modes were determined. The amount of splitting of a given mode as a function of inner rotation rate was found to fit a line (indicating that the state of the fluid was not changing significantly, with the velocities simply scaling up with the inner rotation rate). In addition, a reasonable fit was found between the azimuthal velocities inferred using the splitting measurements, and the velocities measured by the anemometer; it is important to note that the anemometer measurements were used to guide the inversion method (see Mautino's forthcoming master's thesis for further discussion).

Chapter 3: Experimental Apparatus

In this chapter we provide details about the experimental apparatus used to obtain the results described in this thesis. The main devices used were two spherical Couette devices, consisting of an outer shell and an inner sphere that can be rotated differentially, to drive a shear flow in the working fluid between them. The smaller experiment, 60 cm in diameter, had experiments done using liquid sodium, as well as experiments with gas (air and nitrogen) as the working fluid; the focus of the liquid sodium experiments was hydromagnetics, while the gas experiments were aimed at further developing the technique of acoustic mode velocimetry. In this thesis I will focus on the acoustic experiments performed in the 60 cm experiment. The larger experiment, 3 m in diameter, was configured as a liquid sodium experiment for all of the results discussed in this thesis (though earlier work was done with water serving as the working fluid [32, 47, 49, 93]). First we discuss the 60 cm experiment, describing the set-up and instrumentation for the gas experiments. Then, we turn to the 3 m experiment, detailing the set-up used for the liquid sodium experiments discussed in Chapter 4 of this thesis.

3.1 The 60 cm Experiment

3.1.1 Overview

As noted previously, the 60 cm experiment is a spherical Couette device, with a rotating outer spherical shell and an independently rotating inner sphere driving a turbulent flow in the working fluid lying between them. We first provide a description of the mechanical set-up of the system (see Figure 3.1). Further details on the design and set-up, especially for liquid sodium experiments, can be found in [94] and [91].

3.1.2 Mechanical Set-up

The experimental vessel of the 60 cm experiment consists of an outer spherical shell, machined from aircraft alloy titanium (Ti, 6% Al, 4% V) and consists of three parts: an upper hemisphere, a lower hemisphere, and an equatorial hoop into which both pieces screw when the experiment is assembled. The vessel rests in a cylindrical base, on a pair of spherical roller bearings (SKF 7216BECBY). The cylindrical base is in turn attached to the bottom of a large stainless steel vessel which holds the experiment. A lid for this vessel in turn covers the experiment (for mechanical and sodium safety purposes) and holds the upper bearing (SKF 6016-2RSGA) that sits around the shaft that extends from the top of the upper hemisphere. This shaft is hollow, and extends through the top hemisphere, towards the center of the sphere. The bottom hemisphere has a similar design. There are historical reasons

for this design: originally the experimental vessel was designed for a liquid sodium rotating convection experiment, described in Woodward Shew's dissertation [94]. The shafts extending from the top and bottom hemispheres mated with a hollow inner sphere, and kerosene was pumped through a rotating fluid junction in the base of the experiment, up through the hollow shaft of the bottom hemisphere, and through the inner sphere before returning out the bottom. The experiment was heated from the outside with incandescent heaters, and cooled by the kerosene circulating within the inner sphere. The centrifugal force due to the overall rotation served as an analog for gravity, and the heating of the outer sphere and cooling of the inner set up an adverse temperature gradient unstable to convection. Later the experiment was modified by Douglas Kelley [91] to have a differentially rotating, solid copper inner sphere. The bottom shaft was plugged, and the top of it modified to hold the lower bearings for the inner sphere shaft. This inner shaft then extended up through the hollow top hemisphere shaft, which held a seal and top roller bearing assembly. The inner shaft extends out of the outer shaft, where it can be driven by a motor. This motor sits on a mount that in turn sits on the containment vessel's lid. The outer sphere is also rotated by a motor, via a belt that runs around a pulley mounted on the outer shaft, with the motor sitting on the lid, to the side of the inner sphere motor mount. The pulley also has a pair of slip rings in order to acquire the signal from an internal thermal couple, used to monitor the temperature of the working fluid.

The motors used are both General Electric 5KS215SAB105 (10 Hp 60Hz) AC induction motors, and are each driven by a 10 Hp, variable frequency drive (ABB

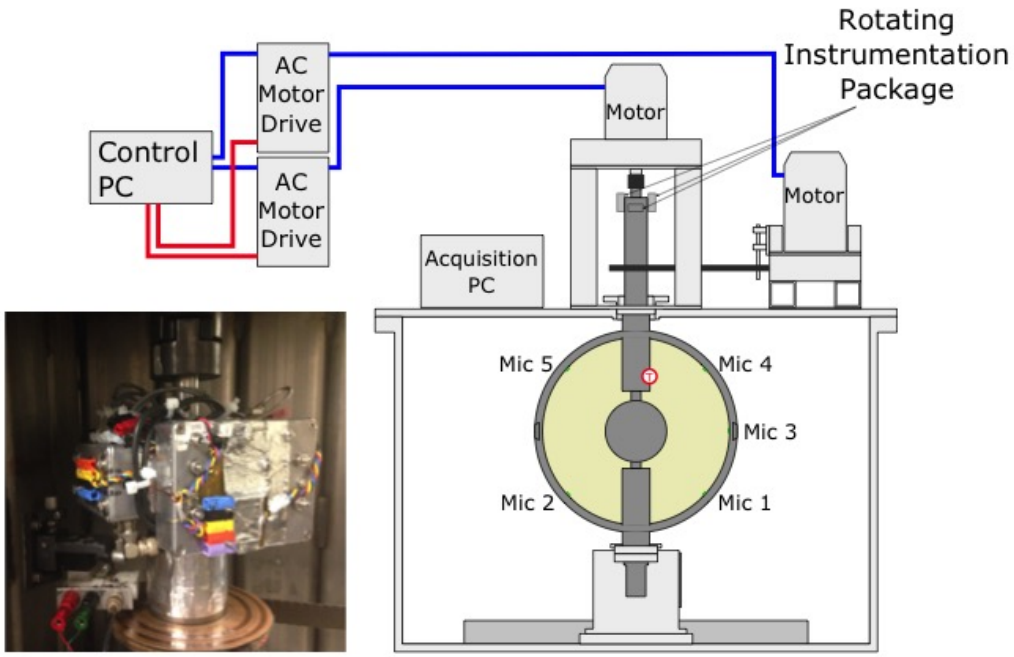

Figure 3.1: Mechanical setup of the 60 cm experiment during the acoustic experiments. Adapted from Figure 3.1 of [91]. The red circle with a "T" in it indicates the position of the internal thermocouple; while the experiment was not purposely heated in the acoustic experiments, viscous dissipation in the system did result in measurable temperature changes (rising from room temperature to a maximum of $\sim 50 - 55$ °C), which in turn change the frequencies of the acoustic modes. The green rectangles indicate the location of 5 of the 6 microphones and are labeled with the numbering used throughout this dissertation; the last microphone does not lie in the plane shown, but is separated from Mic 5 by an azimuthal angle $\Delta\phi = \pi/26$ radians. Inset photo shows installed rotating instrumentation package.

ACH-500). Control signals are sent via an opto-isolated RS-232 connection, and the drives are controlled with a program written in C, run on a control computer. The program uses the MODBUS library to communicate with the drives, and during sodium experiments also controls the magnets. This code is based on similar code written by Santiago Andres Triana to control the motors for the 3 m experiment, and adapted by the author for the 60 cm experiment.

3.1.3 Acoustic Instrumentation

Data for the acoustic mode experiments in 60 cm is taken using two microphones at a given time, from a choice of six microphones. These microphones (model ADMP404) are small, low aspect (3.35 x 2.50 x 0.88 mm), MEMS-element microphones with a built-in impedance converter and output amplifier; their design is typical of those used in mobile devices, and thus are inexpensive and readily available. The microphones are powered, and their analog outputs are acquired, using a rotating instrumentation package mounted to the top outer shaft of the experiment (see figure 3.1). A sketch of the rotating instrumentation set-up is given in figure 3.2 and a schematic of the circuit used with the microphones is given in figure 3.1.3. The position of the microphones are listed in Table 3.1, and Figure 3.1.3 has photographs showing them installed in the hemispheres of the experiment. The combination of mics 1 and 2 allows the parity of the azimuthal m-structure of an acoustic mode to be determined, while the combination of mics 1 and 4 allows determination of a mode's equatorial parity. Mics 5 and 6 are arranged in an m-finder set-up, placed

Microphone	θ	ϕ
Mic 1	$\frac{3\pi}{4}$	0
Mic 2	$\frac{3\pi}{4}$	π
Mic 3	$\frac{\pi}{2}$	0
Mic 4	$\frac{\pi}{4}$	0
Mic 5	$\frac{\pi}{4}$	π
Mic 6	$\frac{\pi}{4}$	$\pi - \frac{\pi}{26}$

Table 3.1: Microphone Positions given by spherical polar angle θ and azimuthal angle ϕ.

Speaker	θ	ϕ
Top Speaker	$\frac{\pi}{2} - \frac{\pi}{13}$	$\pi - \frac{\pi}{13}$
Bottom Speaker	$\frac{3\pi}{4}$	$\frac{3\pi}{4}$

Table 3.2: Speaker Positions given by spherical polar angle θ and azimuthal angle ϕ.

at the same latitude and separated in azimuth by an angle of $\pi/26$.

The acoustic modes can be excited in the system using chirps from one of two speakers, whose positions are shown in Table 3.2. The speakers (model APS2509S-T-R) are piezoelectric, low aspect (25.2 x 16.6 x 1.6 mm) devices, of the type used in mobile devices. A WAV file for the chirp, constructed using Matlab, is played using the rotating computer's soundcard, and sent to the speaker circuit shown in figure 3.5. When one or both sphere are spinning the modes are also stochastically excited (by the turbulent flows, mechanical noise of the experiment, or both). For the most recent data acquired for differential rotation, and for which the inversions detailed below were performed, mics 1 and 2 were used (allowing m-parity to be determined), and the analysis has focused on data taken without any chirp being played.

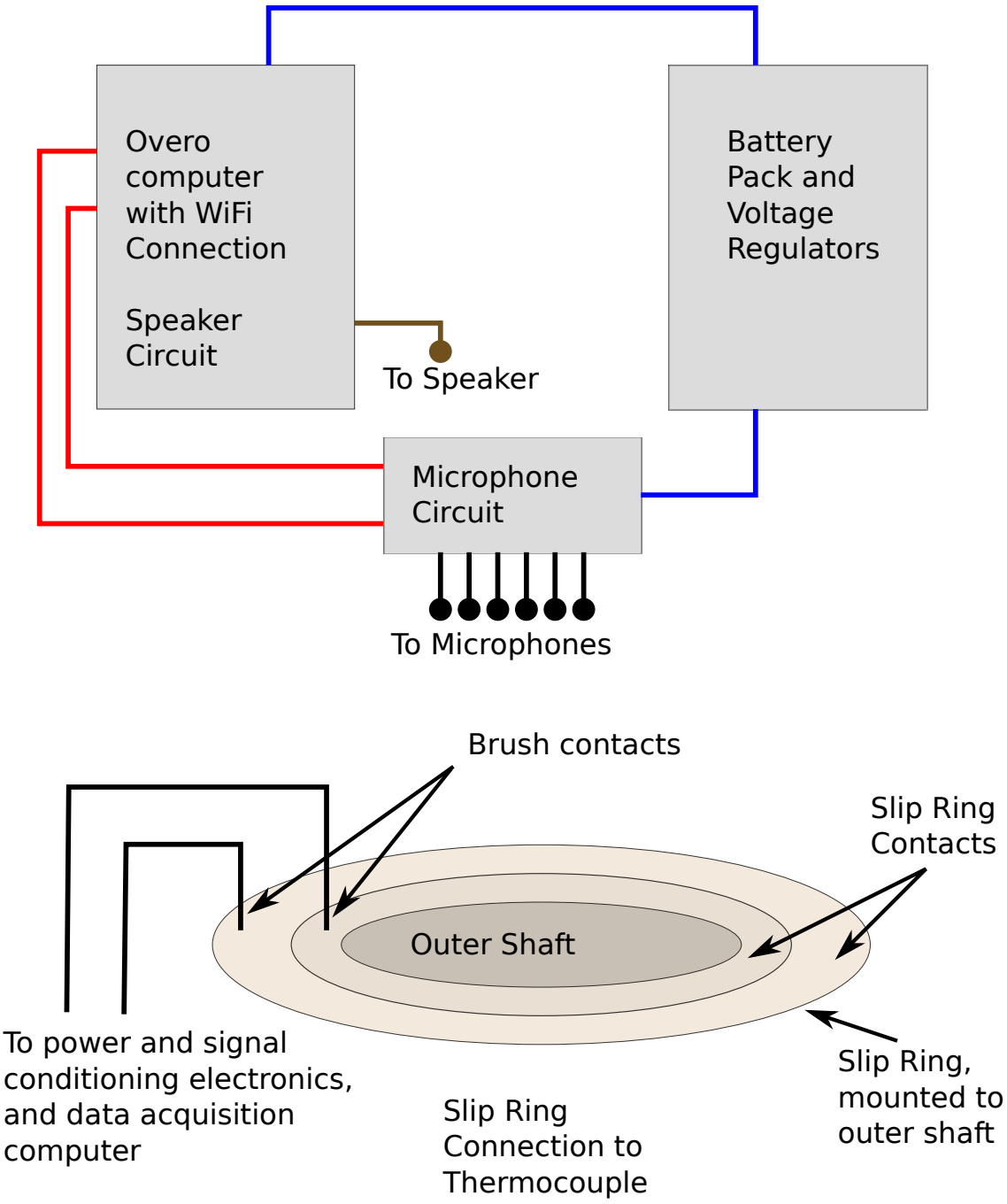

Figure 3.2: Rotating Instrumentation for the 60 cm experiment during the acoustic experiments. Two of the six microphone signals are acquired into the sound card of a rotating computer, mounted on the outer shaft of the 60 cm experiment; the stereo audio output of this card can also be used to drive one of two speakers installed in the vessel. The data is then written out wirelessly to a computer in the lab frame. The temperature measured by the internal thermocouple is also acquired through a slip ring.

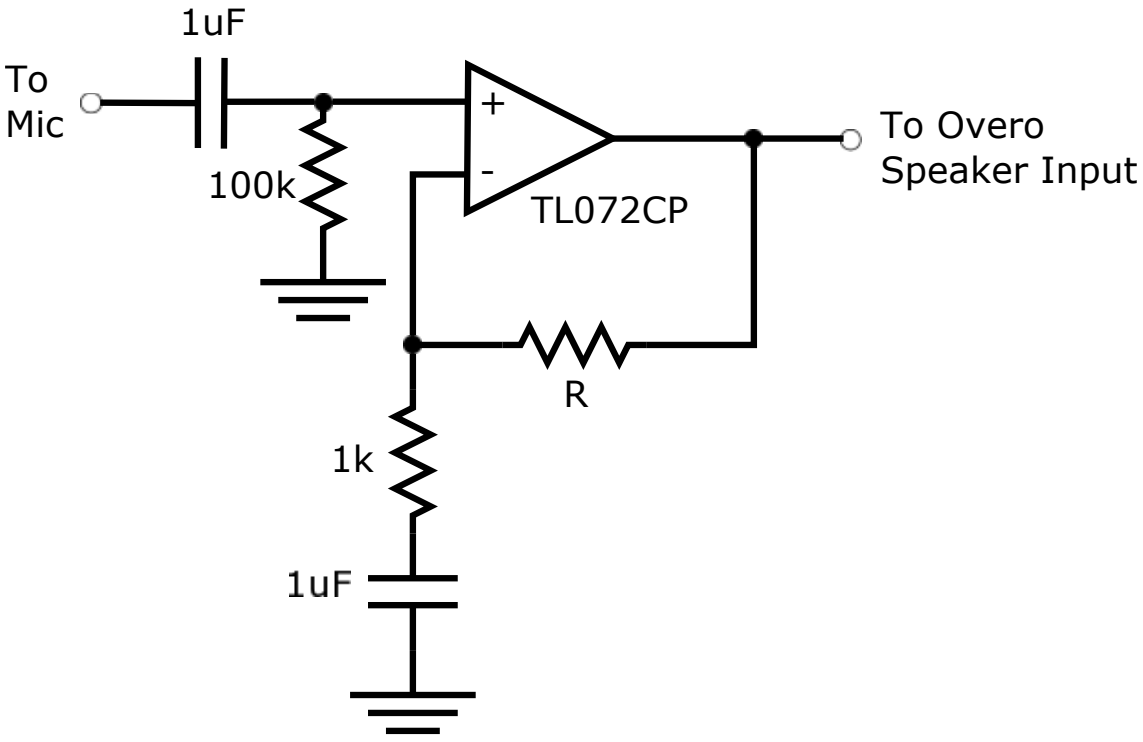

Figure 3.3: Circuit for acquiring data from the microphones. The resistor labeled R determines the gain G of the circuit, with $G = 1 + R/(1k\Omega)$. For the experiments done to date, we have used $R = 15k\Omega$, 6 kΩ, and $\sim$ 0 kΩ, giving $G = 16$, 7, and 1, respectively.

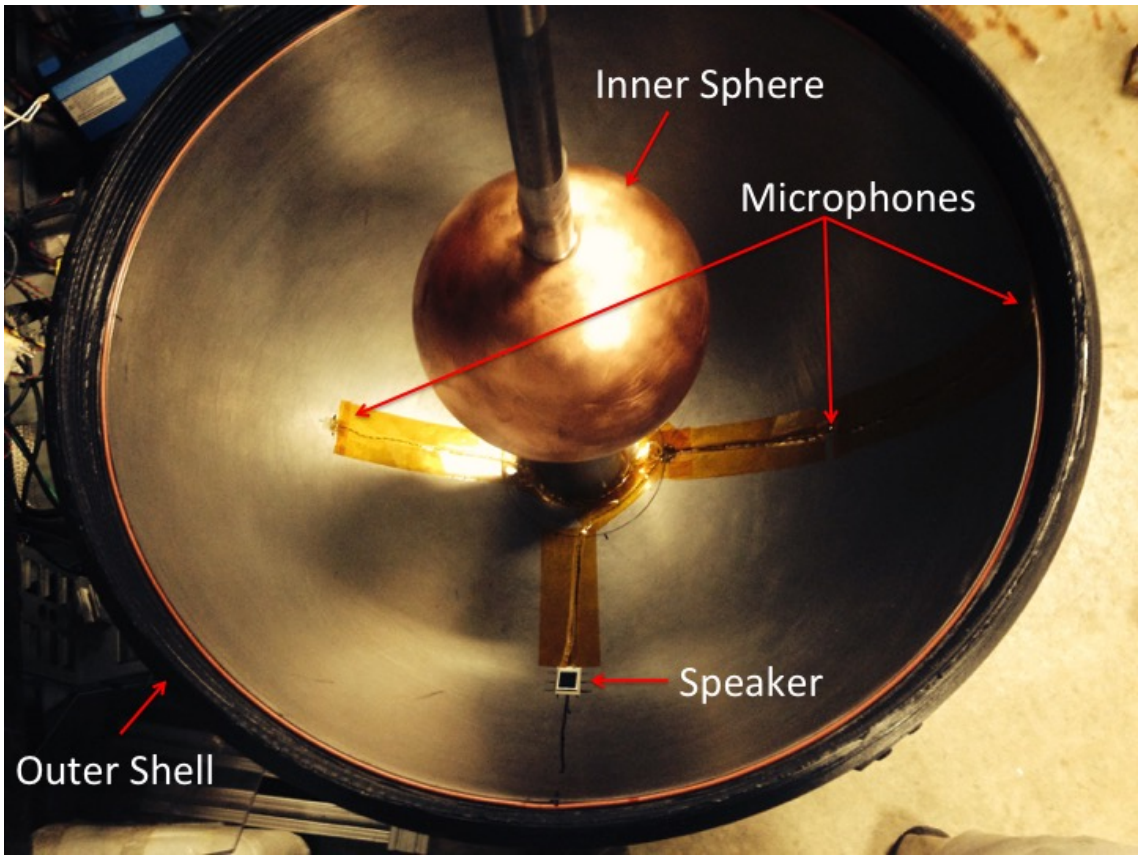

Figure 3.4: Photograph of bottom hemisphere with inner sphere, microphones, and speaker installed.

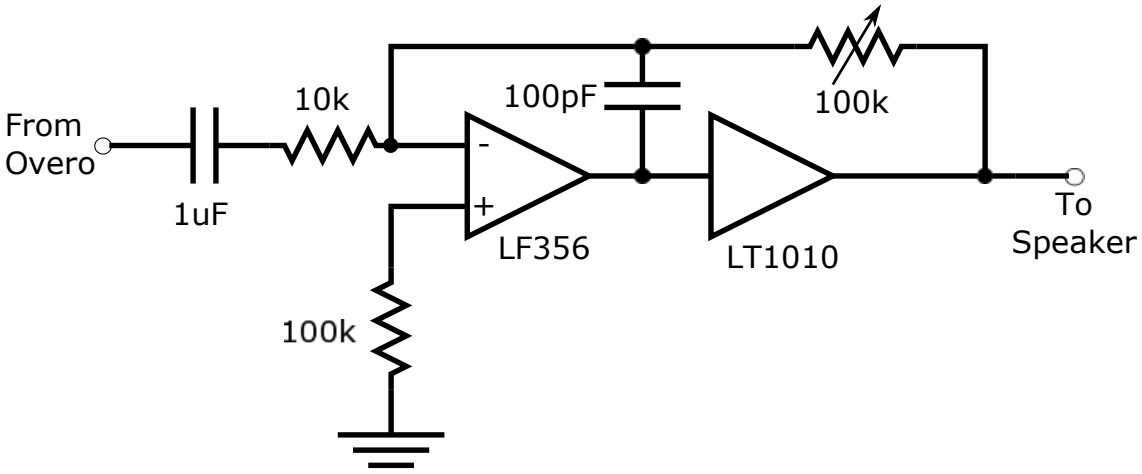

Figure 3.5: Circuit for powering speakers. The LT1010 is an integrated circuit specifically designed to allow op-amps to drive reactive loads, like the piezoelectric speakers we used.

3.2 The 3 m Experiments

We now detail the experimental set-up for the 3 m liquid sodium experiments. In the following sections we describe the mechanical set-up of the 3 m system, as well as the instrumentation and control systems used. Further details on the design and construction of the 3 m experiment can be found in [93] and [32].

3.2.1 Mechanical Set-up

The mechanical set-up of the 3 m system is similar to that of the 60 cm experiment, but on a grander scale. The main vessel again consists of an outer spherical shell, in this case 2.920 m in diameter, and an inner sphere, 1.016 m in diameter (thus, with a inner-to-outer radius ratio $\Gamma = 0.348$, approximating the geometry of earth's core, with $\Gamma = 0.35$). The two spheres rotate independently, and differential rotation is used to drive a shear flow in the liquid sodium that fills the volume between them (see figures 3.2.1 and 3.2.1). The sphere is housed in a stainless steel cubic structure, which in addition to serving as a safety barrier around the sphere, also supports the base of the sphere (which holds the bearing and rotating fluid junctions) and the top bearing, as well as the inner and outer sphere motors. Like in the 60 cm experiment, the inner sphere motor is mounted directly above the vessel, on axis with it. It is coupled to the inner sphere shaft through a Futek TFF-600 reaction flange torque sensor, which provides a measure of the torque required to drive the inner sphere at its set rotation rate. The outer sphere motor is mounted off-axis, on the top of the cube near one of the sides, and

drives the outer sphere via a belt and pulley system.

The outer spherical shell is solid, 1-inch thick stainless steel, up to a northern latitude of 59 degrees, where it mates with a lid. The bottom surface of the lid serves as the top boundary of the spherical fluid volume, while its top surface is flat and serves as a location to mount instrumentation and data acquisition systems. There is a vacuum space in between the top and bottom surfaces of the lid, to insulate these systems from the heat of the liquid sodium during operation. The lid holds the top bearing for the inner sphere shaft, and is also the attachment point for the inner race of the top bearing for the outer sphere. At its thinnest (at the instrumentation ports), this surface is 3/8" thick. A series of halfpipes welded onto the outer sphere serve as channels for heating oil to be circulated, providing temperature control of the experiment. This oil is fed in through a manifold mounted on one side of the outer sphere, while the return flow enters another manifold on the opposite side of the sphere. The oil enters the system and returns to the heating and cooling units through a rotating fluid junction in the base of the experiment. Four instrumentation ports in the lid of the experiment provide direct access to the working fluid. They are located 60.3 cm from the axis of the experiment (corresponding to a cylindrical radial distance of $0.41R_{outer}$), equally spaced in 90 degree increments around the experiment (see figure 3.2.1). See [32] and [93] for more details on the design of the 3 m experiment's vessel and associated systems.

Figure 3.6: Rendering of the 3 m Experiment. The inner sphere and the outer spherical shell can be driven independently by their two respective motors (top). Liquid sodium serves as the working fluid for hydromagnetic experiments. Figure credit: Laurent Hindryckx.

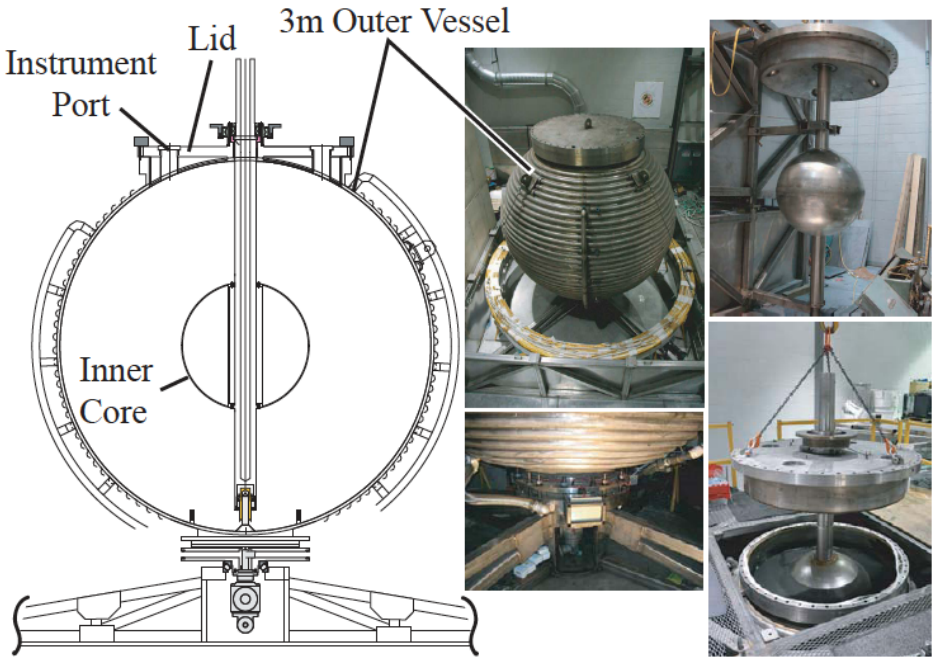

Figure 3.7: Schematic and Photos of the 3 m Experiment. Left: A schematic of the experimental apparatus. Photos, clockwise from top center: the outer sphere; the inner sphere with shaft and lid; the inner sphere being lowered into the outer vessel, which is filled with water in this view; the bottom bearing and rotating fluid junction (allowing heating oil to be circulated in the jacket around the outer sphere). Figure credit: Daniel Zimmerman.

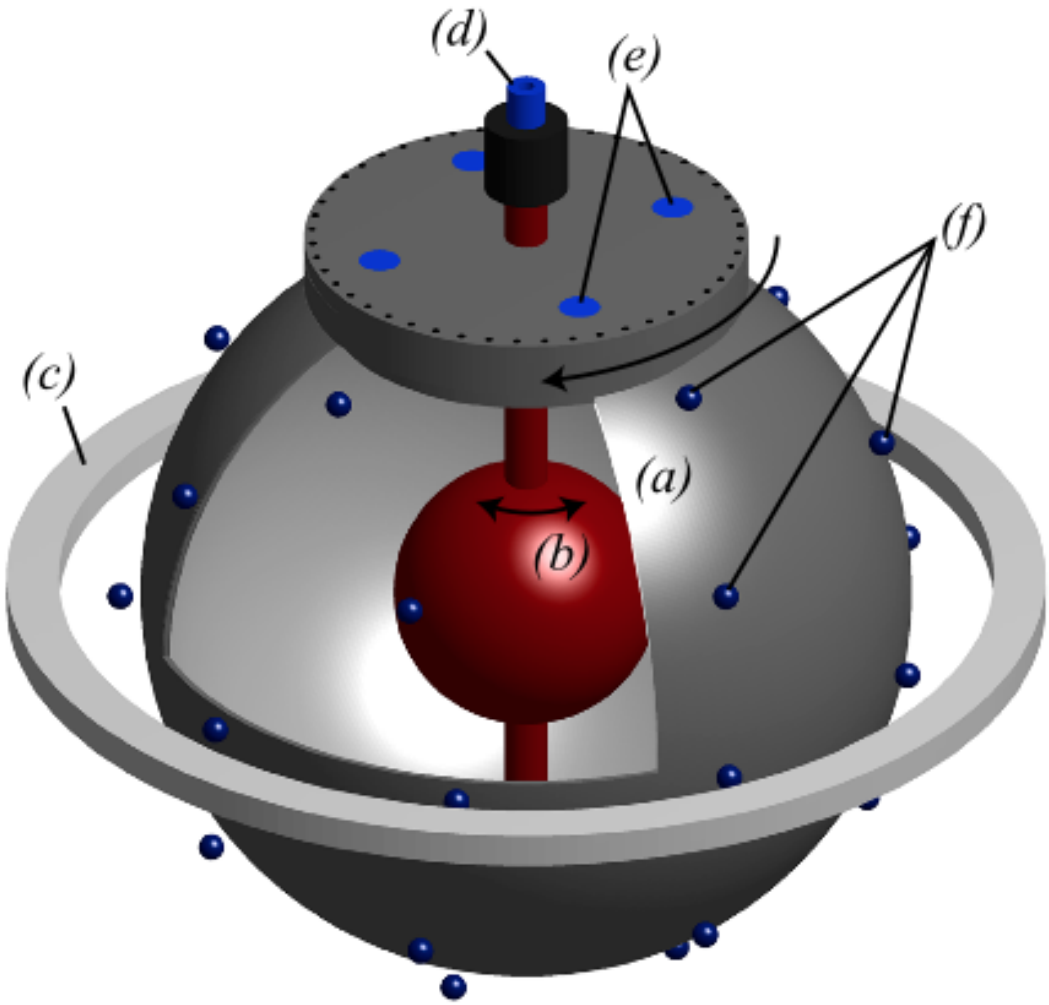

Figure 3.8: Instrumentation for 3 m Experiment. (a) Outer spherical shell; (b) Inner sphere; (c) External magnet, located around the vessel's equator; Note that in later experiments a pair of external mangets was used, with the magnets located symmetrically above and below the equator; (d) Reaction torque sensor; (e) Instrumentation ports; (f) External Hall effect magnetic field probes. Originally Figure 1 from [90].

3.2.2 Magnets

When running 3 m sodium experiments, in addition to choosing inner and outer sphere rotation rates (thus setting Ro and Re), the strength and geometry of the magnetic field applied can be varied. First, we note that since the system is not magnetically shielded, there is always a background magnetic field present, due to the earth and the building that houses the system. For the initial hydromagnetic studies, a single magnet located around the equator of the sphere was used, applying an approximately dipolar field to the system [90] (see figure 3.2.1). More recently, a pair of magnets, located symmetrically above and below the equator, have been used, and can be wired to apply either a dipolar field (with current flowing through them in the same sense) or quadrupolar field (with the dipole moments of the magnets anti-parallel); I assisted Doug Stone in installing the magnets, and in rewiring them as necessary to switch between dipole and quadrupole configurations.

3.2.3 Torque Measurements

While crude measures of the torque supplied by both inner and outer motors are provided by their respective motor drives, a more precise measure of the torque required to drive the inner sphere is provided by a reaction torque sensor, mounted in-line between the inner motor output shaft and the shaft of the inner sphere. Under the assumption of a statistically steady turbulent shear flow, there should be a constant flux of angular momentum through the system, with opposite torques applied to the inner and outer spheres. An imbalance would imply the fluid is

spinning up (for a net positive flux into the system) or down (for a net negative flux) and thus that the fluid is not in a statistically steady state. This neglects the additional angular momentum sinks of bearing friction and air resistance, but for all but the lowest rotation rates these are small compared to fluid torques (at the percent level of the fluid torques for high speeds, but up to around 50% at the lowest Re). [32] Thus measurements of the torque required to drive the inner sphere serve as a good approximation of the angular momentum flux through the system, which in turn serves as a good way of delineating different states of the system [90], which seem to depend on Ro rather than Re. A rotating battery pack mounted on the inner shaft powers the torque sensor as well as the rotating data acquisition system that acquires the torque signal and sends it wirelessly to the primary control computer in the lab frame (see [32] for more details).

3.2.4 Magnetic Measurements

The magnetic field around the system is measured using hall-effect probes (Honeywell SS94A1F), arranged in an array around the exterior of the system. The main array, consisting initially of 31 probes (see figure 3.2.1), is made up of probes mounted on the outer sphere, measuring the field in the spherical radial direction (and thus measuring the external field, including any field due to the magnets, as well as the induced fields in the liquid sodium of the experiment). The probes are arranged in five rings, with the probes in a given ring each sharing approximately the same latitude. The rings ranged in latitude from about 66.0 degrees "south"

to 53.5 degrees "north". For later experiments, an additional two Hall probes were installed at a higher latitude (81.8 degrees "north"), mounted on the lid of the experiment. These were added in order to better constrain the field values at this location, in order to improve estimates of the gauss coefficients, especially the higher degree ones (i.e. $l = 3, 4$); previously the field in this region had been essentially a free parameter, with the possibility that unrealistic field values in this region were favored in order to better fit the measured field at lower latitudes. The exact position of the probes was selected partly based on constraints due to the geometry of the experiment, and partly on an analysis performed by Yuto Beki to determine what measurement locations would give the greatest improvement to the gauss coefficient estimates. The locations of the probes of this external array are given in Table 3.3; the last two entries correspond to the recently added probes. In addition to these measurements of the external field, a pair of measurements of the internal field are obtained from two Hall probes mounted inside the end of a stalk that extends 10cm from one of the instrumentation ports into the fluid. These Hall probes (the same model as those used in the external array) measure the internal field at this location in the fluid in the cylindrical radial and azimuthal directions.

3.2.5 Gauss Coefficient Projection and Selection Rules

While time series and spectra of the Hall probes can be looked at individually, and the internal field measurements are generally analyzed in this way, the external array data is used to estimate the associated Gauss coefficients of the field up to

r/b	θ	ϕ	r/b	θ	ϕ
1.0522	2.7065	0.7856	1.0522	1.6008	4.1905
1.0522	2.7049	2.3564	1.0522	1.6008	4.8874
1.0522	2.7049	3.9259	1.0522	1.6118	5.5851
1.0522	2.7222	5.4978	1.0522	1.0818	0.4485
1.0522	2.1429	0.4485	1.0522	1.0914	1.3458
1.0522	2.1490	1.3458	1.0522	1.1023	2.2445
1.0522	2.1607	2.2445	1.0522	1.1074	3.1416
1.0522	2.1710	3.1416	1.0522	1.1177	4.0387
1.0522	2.1853	4.0387	1.0522	1.1320	4.9375
1.0522	2.1941	4.9375	1.0522	1.0767	5.8345
1.0522	2.1375	5.8348	1.0522	0.6456	0.3943
1.0522	1.6158	0	1.0522	0.6713	1.9673
1.0522	1.6223	0.6980	1.0522	0.6796	3.5366
1.0522	1.6321	1.3964	1.0522	0.6369	5.1026
1.0522	1.6425	2.0954	1.1054	0.1431	1.3090
1.0522	1.5870	2.7861	1.1054	0.1431	3.9270
1.0522	1.5937	3.4908			

Table 3.3: Probe Positions of the External Hall Magnetic Field Probes for the 3 m Experiment. Angles are measured in radians, while the radial positions are normalized by the inner radius of the outer spherical shell, $b = 1.46$m.

degree and order 4. Details of the method used (a least squares fit of the Gauss coefficients (see section 2.3.1) up to $l = 4$) are given in [48]; the specific code used in performing the analysis consists of Matlab scripts.

Following this operation, the induced magnetic field is represented in terms of a sum of poloidal vector spherical harmonics S_l^m, the associated Gauss coefficients giving the strength of each of the harmonics. The external applied field can also be written in terms of vector spherical harmonics, and as noted in section 2.3.1, incompressible fluid flows can be written using the same expansion. The induction equation (eq. 2.25) allows us to calculate the magnetic field induced by the interaction of a given velocity field with a given applied magnetic field. For given applied field and velocity geometries, only certain induced field geometries are possible; the

mathematical rules governing this, so-called selection rules, are presented in Table 3.2.5, take from [27]. Essentially, for a given applied magnetic field geometry $\mathbf{B_{applied}}$, expressed as some S_l^m or T_l^m, and an observed induced field $\mathbf{B_{induced}}$, also expressed in terms of one or more of the S_l^m or T_l^m, then the observed induction can only be attributed to certain distinct velocity field patterns $\mathbf{v} = s_l^m, t_l^m$. For clarity, we use uppercase for vector spherical harmonics representing magnetic field (applied or induced) and lowercase for those representing fluid velocities. The selection rules governing the system specify which triplets of $(\mathbf{v_{fluid}}, \mathbf{B_{applied}}, \mathbf{B_{induced}})$ are allowed, given the geometrical properties of the vector spherical harmonics and the physics of the induction equation, and are similar in spirit and in mathematical machinery to the so-called 3j symbols used extensively in quantum mechanics. In Table 3.2.5, we write s_α or t_α for the vector spherical harmonic describing the fluid motion, with α representing the specific l and m of the field. Similarly for the applied magnetic field we write S_β or T_β, and for the induced field, S_γ or T_γ (following a similar convention used in Bullard and Gellman 1954 [27].

3.2.6 Pressure Measurements

Three of the four instrumentation ports contain a pressure probe (Kistler 211B5) to measure the local pressure (with a sensitivity of 50 mV/psi). These probes were also used in water experiments conducted previously in the 3 m experiment. The probes include compensating elements to cancel out signals due to centrifugal accelerations, so are unaffected by the rotation of the outer spherical shell

$(\mathbf{v_{fluid}}, \mathbf{B_{applied}}, \mathbf{B_{induced}})$	Selection Rules
$(s_\alpha S_\beta S_\gamma)$, $(s_\alpha T_\beta T_\gamma)$, $(t_\alpha S_\beta T_\gamma)$	(i) $l_\alpha + l_\beta + l_\gamma$ is even, (ii) l_α,l_β, and l_γ can form the sides of a triangle, including degenerate case of one equaling the sum of the other two, (iii) at least one of the four expressions $m_\alpha \pm m_\beta \pm m_\gamma$ vanishes, (iv) three of the harmonics has *cos* or one has ($m = 0$ counts as *cos*).
$(s_\alpha T_\beta S_\gamma)$, $(s_\alpha S_\beta T_\gamma)$, $(t_\alpha S_\beta S_\gamma)$, $(t_\alpha T_\beta T_\gamma)$	(i) $l_\alpha + l_\beta + l_\gamma$ is odd, (ii) l_α,l_β, and l_γ can form the sides of a triangle, (iii) at least one of the four expressions $m_\alpha \pm m_\beta \pm m_\gamma$ vanishes, (iv) two of the harmonics has *cos* or none has ($m = 0$ counts as *cos*), (v) no two harmonics are identical.
$(t_\alpha T_\beta S_\gamma)$	Always zero.

Table 3.4: Selection Rules. For the given combinations of vector spherical harmonics of the fluid velocity, applied magnetic field, and induced magnetic field in the first column, only those obeying the selection rules given in the second column are allowed, i.e. the velocity field $(s,t)_\alpha$ can interact with the applied magnetic field $(S,T)_\beta$ to produce the induced magnetic field $(S,T)_\gamma$.

in which they are installed. Their -5% low frequency response point is at 0.025 Hz, so they are insensitive to the centrifugal pressure of the fluid due to the overall rotation, but are sensitive to fluctuations, including those associated with inertial waves. Their +5% high frequency response point is at 50 kHz, so they are also sensitive to acoustic signals, though that depends on the filters used with them and the sample rate of the data acquisition system. Previously the circuit used to power these probes and filter their outputs (described in [93]) used both a high-pass filter (with roll-off frequency 0.033 Hz, similar to the probes' -5% point) and low-pass filter (with roll-off frequency 207 Hz, chosen based on the data acquisition system's typical sampling rate of 256 Hz). I modified this circuit, replacing the 1.425 nF capacitors used in the RC low-pass filters with 19.42 nF capacitors, changing the

roll-off frequency from 207 Hz to 2.34 kHz. For some of the acoustic studies performed in 3 m, described later in section 5.6, a sampling rate of 5 kHz was used for these probes, so the measurements were sensitive to acoustic modes of the system.

In addition to these three probes, there are another set of three probes, one in each of the ports that also has a Kistler pressure probe, installed with a view towards taking acoustic measurements. Three ICP Dynamic Pressure Sensors (model 106B51 or 106B52, with 1000 mV/psi and 5000 mV/psi sensitivities, respectively), manufactured by the Pressure Division of PCB Piezotronics, are used. These probes are powered by Model 480C02 Battery-Powered ICP Sensor Signal Conditioners. Their -5% low frequency response point is at 2.5 Hz, so they are not sensitive to some of the slow waves that might be present in the system, including some of the inertial waves, but with a resonant frequency above 40 kHz they provide more sensitive pressure measurements in the acoustic frequency range. Data is not normally acquired from them, but they were used for some of the acoustic studies done (and discussed in section 5.6).

Chapter 4: Magnetic Studies

In this chapter we present some of the findings from the 3 m liquid sodium experiment, which in addition to their general scientific interest serve as the motivation for the development of the acoustic velocimetry technique, described in chapter 2, with results given in chapter 5.

4.1 Overview of Results in the 3 m Experiment

Previous hydrodynamic and hydromagnetic studies in the 3 m device have established that in the accessible parameter ranges, the turbulent state is mainly a function of $Ro = (\Omega_i - \Omega_o)/\Omega_o$, with changes in Re serving to simply scale the system variables (velocities, torques, etc.) but not altering the topology of the flow [90] (see Figure 4.1). The 3 m experiment has now been taken to full speed on the outer sphere (a rotation rate of 4 Hz), and for a number of Ro has also reached the maximum allowed torque values (as set by the torque rating of the currently installed reaction torque sensor installed in-line between the inner motor and inner sphere shaft, which is also close to the maximum torque that can be supplied by the inner motor as currently configured; see section 3.2.3 for more details). Here we build on some of the work presented in [90].

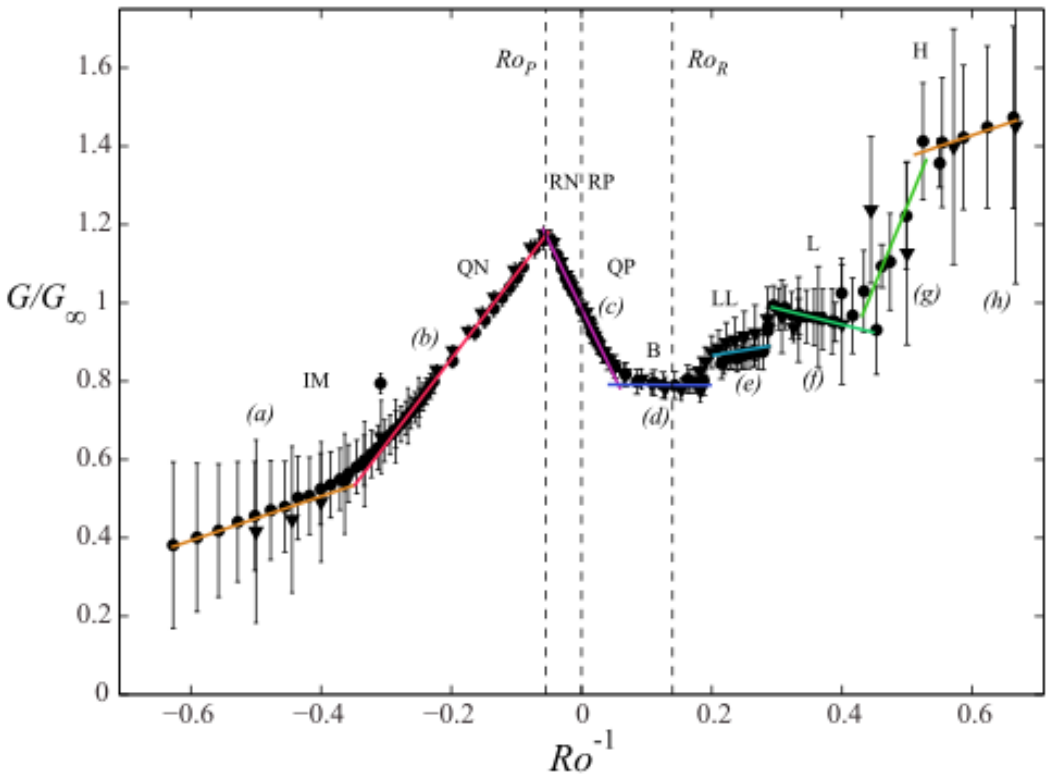

Figure 4.1: Normalized Torque vs. Ro^{-1} in 3 m Experiment. The average torque G required to drive the inner sphere at its selected rotation rate is plotted, normalized by the torque G_{inf} needed to drive it at that same rotation rate when the outer is stationary (corresponding to $Ro = \text{inf}$), versus Ro^{-1}. Inverse Ro is used for the abscissa because the torque curve is continuous through $Ro^{-1} = 0$, while it is discontinuous through $Ro = 0$. The fact that the curves collapse for different Re (i.e. different inner rotation rates for measuring G and G_{inf}) indicates that for the parameters explored in the 3 m experiment, the flow state is a function only of Ro, and not Re. The different state regions are labeled, and discussed further in the text. Originally Figure 3 from [90].

4.2 Inferred Velocity Patterns

In previous work [90], some of the different states (as determined by the spectra of wall shear probes, as well as torque measurements) seen in the 3 m experiment as a function of Ro were classified and characterized. Here we consider a similar range of Ro, and characterize the states by looking at the induced magnetic fields found for the case of a dipolar applied field, as well as, where available, the case of a quadrupolar field. We use this information to infer the possible spatial velocity patterns present in the flow, investigate how the patterns change with Ro, and compare with results found for wall shear stress and torque (see Figure 4.1). In particular, here we make used of the array of external Hall magnetic field probes, and fit these measurements with an expansion in vector spherical harmonics (see sections 3.2.4 and 3.2.5 for more details on the array and this method); then by using selection rules we infer the possible flows within the experiment. In Table 4.1 we present the only possible velocity patterns that can produce a given induced field pattern, for both the case of a dipolar applied field and a quadrupolar applied field, using the selection rules from [27], presented in Table 3.2.5. In Figure 4.2, we show the vector spherical harmonics up to $l = 4$ and $m = 4$, at the surface of a sphere (presented with the Mollweide projection), showing the component of the field in the cylindrical radial direction, to give an idea of what these various magnetic field patterns look like.

Turning to experimental results, in Table 4.2, we note the possible velocity fields that could cause the observed induction patterns seen at a variety of Ro. In

	Possible Velocity Patterns $\mathbf{s_l^m}$ for:	
Observed **B** Field $\mathbf{S_l^m}$	S_1^0 applied **B** field	S_2^0 applied **B** field
S_1^0	s_2^0	s_1^0, s_3^0
S_1^{1c}	s_2^{1c}, t_1^{1s}	$s_1^{1c}, s_3^{1c}, t_2^{1s}$
S_2^0	s_1^0, s_3^0	s_2^0, s_4^0
S_2^{1c}	$s_1^{1c}, s_3^{1c}, t_2^{1s}$	$s_2^{1c}, s_4^{1c}, t_1^{1s}, t_3^{1s}$
S_2^{2c}	s_3^{2c}, t_2^{2s}	$s_2^{2c}, s_4^{2c}, t_3^{2s}$
S_3^0	s_2^0, s_4^0	s_1^0, s_3^0, s_5^0
S_3^{1c}	$s_2^{1c}, s_4^{1c}, t_3^{1s}$	$s_1^{1c}, s_3^{1c}, s_5^{1c}, t_2^{1s}, t_4^{1s}$
S_3^{2c}	$s_2^{2c}, s_4^{2c}, t_3^{2s}$	$s_3^{2c}, s_5^{2c}, t_2^{2s}, t_4^{2s}$
S_3^{3c}	s_4^{3c}, t_3^{3s}	$s_3^{3c}, s_5^{3c}, t_4^{3s}$
S_4^0	s_3^0, s_5^0	s_2^0, s_4^0, s_6^0
S_4^{1c}	s_3^{1c}, s_5^{1c}	$s_2^{1c}, s_4^{1c}, s_6^{1c}, t_3^{1s}, t_5^{1s}$
S_4^{2c}	$s_3^{2c}, s_5^{2c}, t_4^{2s}$	$s_2^{2c}, s_4^{2c}, s_6^{2c}, t_3^{2s}, t_5^{2s}$
S_4^{3c}	$s_3^{3c}, s_5^{3c}, t_4^{3s}$	$s_4^{3c}, s_6^{3c}, t_3^{3s}, t_5^{3s}$
S_4^{4c}	s_5^{4c}, t_4^{4s}	$s_4^{4c}, s_6^{4c}, t_5^{4s}$

Table 4.1: Selection Rules Relevant for 3 m Experiment. For the induced modes with non-zero m, we list only the velocity patterns responsible for the *cos* modes S_l^{mc}; to get the selection rules for the *sin* ones S_l^{ms}, the c and s symbols are switched in the velocity modes s_l^m.

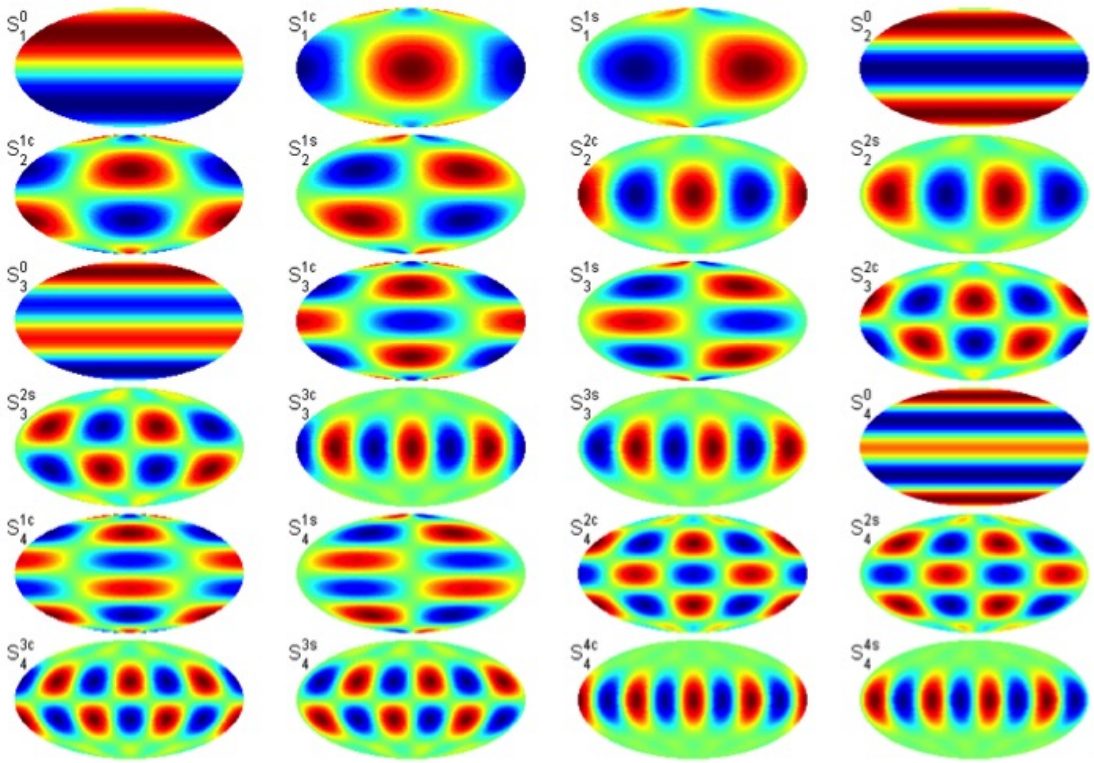

Figure 4.2: Cylindrical Radial Component of Vector Spherical Harmonics up to degree and order 4. Red corresponds to field out of the page, while blue is field into the page, with green being zero field. These illustrations give an idea of the field patterns that are discussed throughout this chapter. Figure Credit: Douglas H. Kelley.

the Induced Magnetic Fields column of this table, we note the Gauss coefficients that have the largest fluctuations (quantified by their RMS deviations). This gives us information about what magnetic field patterns are present in the system, and thus also what velocity patterns may be present. Since we're looking at fluctuating patterns (i.e. those Gauss coefficients with large RMS deviations), the spectral properties of the Gauss coefficients also inform us about possible waves present in the system with the geometry of the velocity patterns associated with them. We also obtain information about the turbulent amplitude present in the system specific to that spatial harmonic, among other things.

We can also look at the means of the Gauss coefficients. Here we generally expect only the axisymmetric (i.e. $m = 0$) modes to have significant mean values, since any non-zero m pattern will average to zero unless it is stationary in the frame of the external array. Since the inner sphere rotates at a different rotation rate than the outer, the shear flows driven by this differential rotation will in general drift relative to the frame of the external array. Also, since we are applying axisymmetric fields (dominated by either S_1^0 or S_2^0), proper calibration is more critical to separate out the induced field from the applied field. In the third column of Table 4.2, we list the possible velocity field patterns that could result in the observed induction, assuming that the measured induced magnetic field is created by the velocity field interacting with the applied dipolar field. We do not list velocity fields that could generate one of the induced fields by interacting with another of the induced fields. In other words, we assume that the induced magnetic fields are not strong enough to produce additional large magnetic fields by interacting with the velocity field. This

assumption is reasonable since the applied field is weak and the measured induced magnetic field is smaller than the applied field, with the possible exception of T_2^0, induced from the applied field by the ω effect (discussed previously in section 2.2.4, and discussed further later in this section). Since we are driving a shear flow by differentially rotating the two spheres, for most Ro the dominant velocity pattern present is simply azimuthal flow of varying magnitude (to match the boundaries). This corresponds in vector spherical harmonics to a t_1^0 velocity field. Thus, in the final column of Table 4.2, we list the magnetic field patterns induced by the action of a t_1^0 velocity pattern on the experimentally measured induced fields (listed in column 2). Note that neither an S_1^0 nor an S_2^0 applied field act on a t_1^0 velocity pattern to produce any observable (i.e. of the form S_l^m) induced fields, so this is perforce a two-step induction process, (applied field $->$ induced field $->$ secondary induced field), but the overall strength of the t_1^0 velocity pattern makes it worthwhile to consider.

One particularly important aspect of the t_1^0 flow's interaction with magnetic field is the so-called ω effect, whereby poloidal magnetic field (i.e. fields that can be described by some combination of S_l^m components) is converted into toriodal magnetic field (T_l^m). For at least some of the hydromagnetic states studied in the 3 m experiment, there is a strong ω effect, with large azimuthal fields, as measured by the internal Hall probe measuring B_ϕ, present [90] (see Figure 4.3).

Another phenomenon of particular interest is the so-called spin-over mode, which is an inertial mode that has the same frequency as the fluid rotation, and is often one of the easiest to excite. For instance, it can be excited via precessional

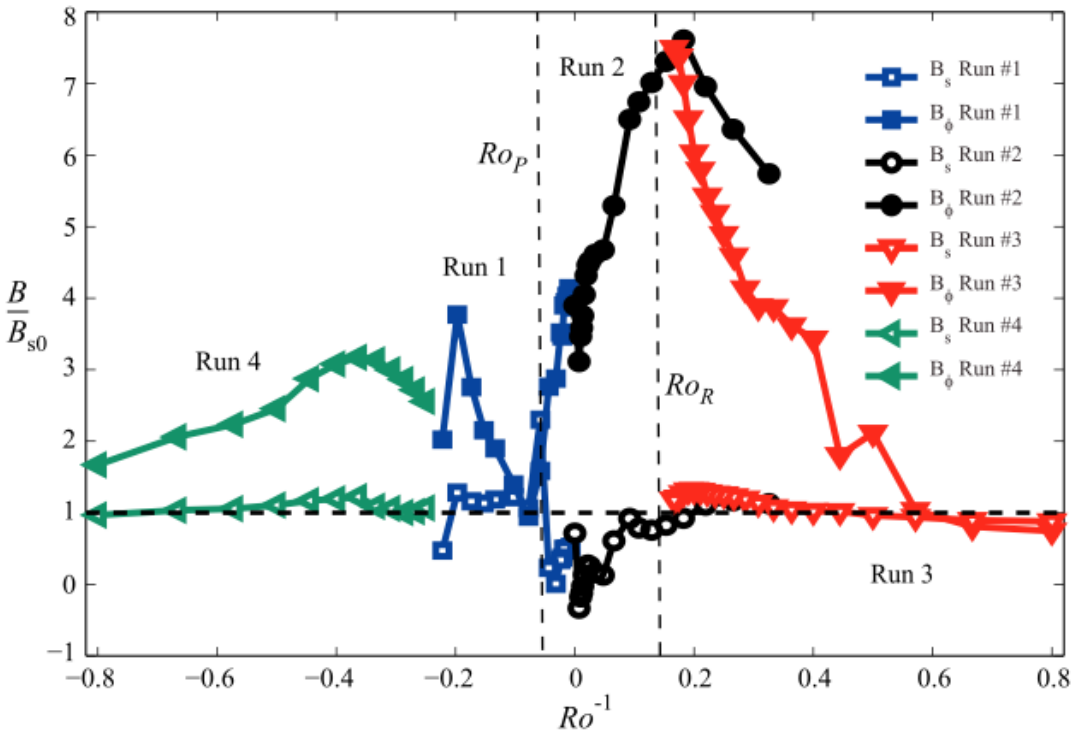

Figure 4.3: Internal Field Measurements from 3 m Experiment. Mean cylindrical radial (B_s) and azimuthal (B_ϕ) fields measured at one location, 10 cm into the flow, at a cylindrical radius of 60 cm, normalized by the applied field strength at that location. Notice the large amplification of B_ϕ over the applied field, a sign of the ω effect acting in the experiment. Originally Figure 9 from [90].

forcing, and for the case of solid body rotation of the 3 m experiment (i.e. inner and outer spheres rotating at the same rate), this mode is excited due to the precession of the experiment's rotation axis as the Earth rotates; in-depth investigations of this phenomenon were reported in [93]. The spin-over mode corresponds to a t_1^1 velocity pattern, and results in a S_1^1 induced field for the case of an applied dipole field (S_1^0). In Figure 4.4 we plot the power in the S_1^1 induced magnetic field at the frequency of the outer sphere f_o versus Ro, since the spin-over mode has the same frequency as the fluid rotation, which in our system is usually dominated by the outer sphere rotation. For the Ro values considered, the peak excitation of the spin-over mode corresponds to the torque maximum of the system, around $Ro = -18$, while the minimum occurs at $Ro = 5$, near the boundary between the LL and B states, where some of the lowest normalized torques are found.

4.3 Characterization of States at different Ro

It is informative to look at the frequency spectra of the most significant Gauss coefficients, to see if there are waves present in the system (indicated by significant power at specific frequencies), and to further distinguish between different states found as we vary Ro. Here we organize our findings in terms of the previously identified states found in the 3 m system, organized in terms of their Ro dependence. In the figures below we present the power spectral density versus frequency of the dominant induced field patterns, for a variety of Ro. We consider both the case of a dipole (S_1^0) applied field (Figures 4.5 to 4.9) and the case of a quadrupole (S_2^0)

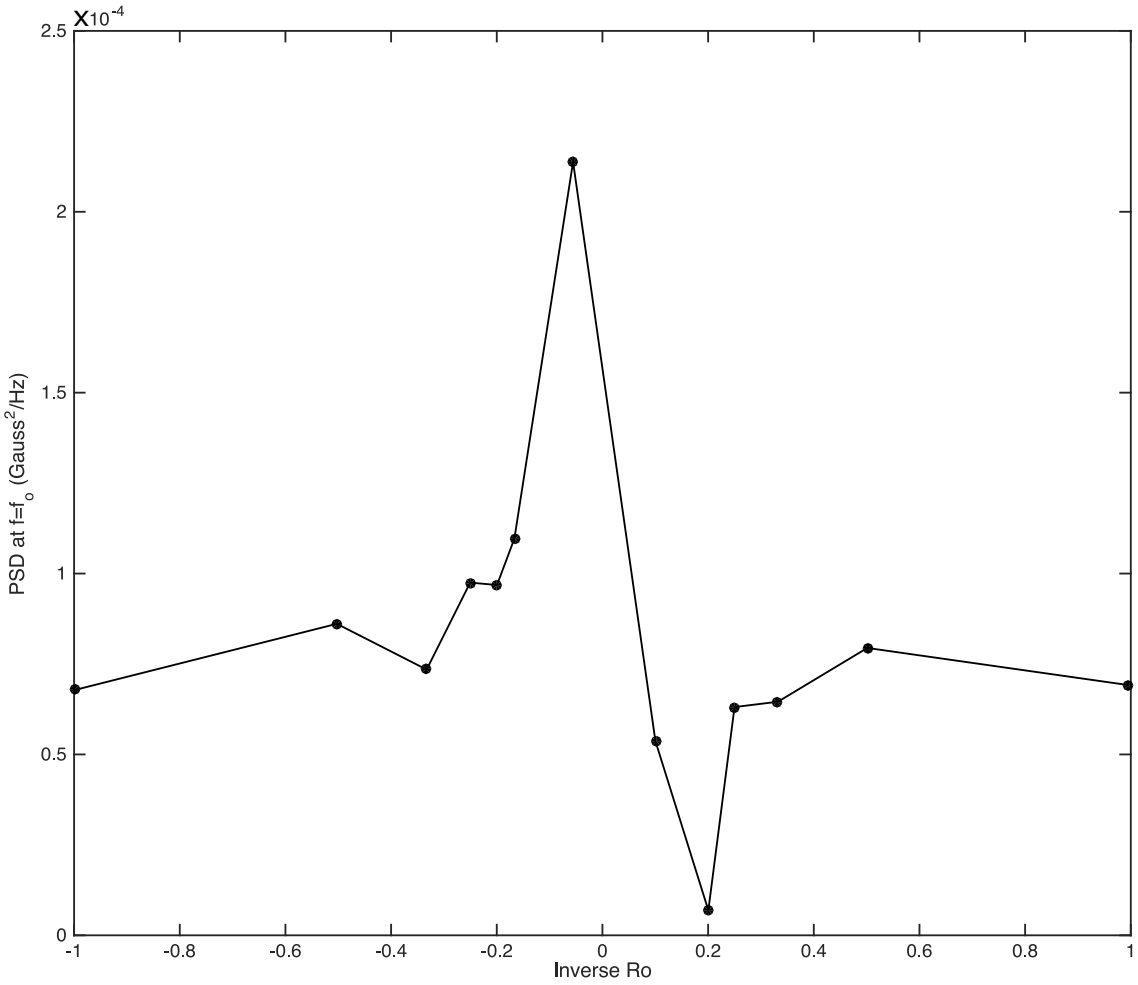

Figure 4.4: Average Power Spectral Density at f_o, for the case of a S_1^0 applied field, for a variety of Ro. The lines are offset from one another for clarity.

Ro	Observed Induced Magnetic Fields	Possible Velocity Fields	Possible Induced B via t_1^0
-1	S_1^0, S_3^0, S_1^1	$s_2^0, s_2^1, s_4^0, t_1^1$	$S_1^1, T_2^0, T_2^1, T_4^0$
-2	S_1^1, S_3^1	$s_2^1, s_4^1, t_1^1, t_3^1$	$S_1^1, S_3^1, T_2^1, T_4^1$
-3	S_1^1, S_1^0, S_3^1	$s_2^0, s_2^1, s_4^1, t_1^1, t_3^1$	$S_1^1, S_3^1, T_2^0, T_2^1, T_4^1$
-4			
-5			
-6	S_1^0, S_1^1, S_2^1	$s_1^1, s_2^0, s_2^1, s_3^1, t_1^1, t_2^1$	$S_1^1, S_2^1, T_1^1, T_2^0, T_2^1, T_3^1$
-18	S_2^1, S_1^1	$s_1^1, s_2^1, s_3^1, t_1^1, t_2^1$	$S_1^1, S_2^1, T_1^1, T_2^1, T_3^1$
10	S_1^1, S_1^0, S_3^1	$s_2^0, s_2^1, s_4^1, t_1^1, t_3^1$	$S_1^1, S_3^1, T_2^0, T_2^1, T_4^1$
5	S_1^0, S_1^1, S_2^1	$s_1^1, s_2^0, s_2^1, s_3^1, t_1^1, t_2^1$	$S_1^1, S_2^1, T_1^1, T_2^0, T_2^1, T_3^1$
4			
3			
2			
1			

Table 4.2: Experimentally Measured Induced Large Magnetic Fields for various *Ro* for S_1^0 (dipole) applied magnetic field. Column 2 lists the largest observed induced magnetic fields (categorized by Gauss coefficient) for the *Ro* listed in the column 1. Column 3 lists the possible velocity patterns that could interact with the applied (dipole) magnetic field to result in the induced fields listed in column 2. The final column lists the magnetic fields that could be induced by the action of the observed fields of column 1 via a t_1^0 velocity field (note that the applied S_1^0 field does not result in any observable induced field).

applied field (Figures 4.10 to 4.12). For this discussion we follow the categorization of fluid states presented in [90], which organizes the states according to Ro^{-1}, and so in the following plots we order the states by Ro^{-1}, even though the labels are still in terms of Ro. In Tables 4.3 and 4.4, we summarize these findings.

The first state region we consider is the Inertial Mode (IM) region, characterized by strong spectral peaks corresponding to inertial modes that have been excited in the system. For the data we are presenting here, both $Ro = -1$ and $Ro = -2$ fall into this category. Strong spectral peaks are evident for one or both of these states in Figures 4.6, 4.7, and 4.9 for the dipole case, and in Figures 4.11 and 4.12 for the quadrupole case. Note also the differences between $Ro = -1$ and $Ro = -2$, indicating the presence of different inertial modes (as has been noted previously in [90] for the 3 m experiment, and systematically investigated in the 60cm liquid sodium experiment [91]). Since $|Ro|$ is relatively small for these states, the system is dominated by the overall rotation of the system, and thus it is not surprising that the inertial modes, Coriolis-restored wave modes, are present and the dominant feature of the system.

The next state region is labeled the Quiet region (QN), with the second letter indicating that the Ro is negative. This state is characterized by broadband spectra corresponding to turbulence in the system, but no sharp spectral peaks in the wall shear or pressure. For this data, the states $Ro = -3, -4, -5, -6$, and -18 all fall into the "QN" category. As can be seen from the spectra in Figures 4.5 to 4.9, while these states do not have the sharp spectral peaks at low frequencies characteristic of the Inertial Mode region, they do have some variations among them. In particular,

while $Ro = -3$ and $Ro = -4$ have relatively flat spectra, a broad peak around a frequency of $2.8\Omega_o$ appears for $Ro = -5$, and is also present in $Ro = -6$; possibly the same feature is present for $Ro = -18$ at a lower normalized frequency of around $2.5\Omega_o$. This peak is much broader than the inertial mode peaks, and thus does not have as well-defined a frequency as the inertial modes. Also, it shows up most strongly in the $m = 1$ Gauss coefficients, but is also seen in $m = 0$ ones, and thus does not seem to be characterized by a single azimuthal wave number. Also for this state, which corresponds approximately to the torque maximum of the system (normalized by Re), there is a large broad peak at $\Omega = \Omega_o$.

We did not take data for the "RN" and "RP" states, corresponding to $|Ro^{-1}| < 0.03$. Moving on to positive Ro, we note that here there are a couple of regions of bistability, where the system spontaneously transitions between two distinct states for some range of Ro, with the neighboring regions in Ro on either side dominated by one or the other state. Starting at low positive Ro, we first have the high torque, or "H", state. For the data considered here, the $Ro = 1$ state falls in this category. It is characterized by a number of fairly sharp spectral peaks, possibly inertial modes, at $0.100 f_o$ and $0.176 f_o$ (with $l = 2$, $m = 1$), as well as by a spectral feature at $0.276 f_o$ that doesn't seem to have a definite l or m associated with it. In particular, the $(2, 1 : 0.176 f_o)$ peak likely corresponds to a $l = 3$, $m = 1$ velocity mode, which closely matches the full sphere prediction for an inertial mode with $l = 3$, $m = 1$, and a frequency of $0.1766 f_o$. For a range of Ro numbers, this state is bistable with another state characterized by a lower value of the torque, the so-called low ("L") state; the $Ro = 2$ state falls in this region of bistability. These states and the region

of bistability were investigated in depth in the 3 m water experiments and the results presented in [32]. As Ro is further increased, the transitions between the H and L states cease, with the system always in the L state. For $Ro = 3$ the system is in this L state. At even greater Ro, however, another region of bistability is found, with the system transition between the L state and another state characterized by even lower torque, and thus denoted "LL"; the transition region is narrower than in the H/L bistability case, however, and for the Ro values considered here there isn't an example of this bistability, with $Ro = 3$ in the L state and $Ro = 4$ in the LL state. The final state we consider here is the "B", or "bursty", state identified in [90]. For the data presented here, the $Ro = 10$ state falls in this category, and the $Ro = 5$ state is near the boundary between this state and the "LL" state.

4.4 Internal Field Measurements

While the majority of the measurements taken for the 3 m experiment are from the external Hall probe array, two measurements of the magnetic field in the interior of the system are taken. These are also taken by Hall magnetic field probes, in this mounted inside a tube that extends from one of the instrumentation ports into the fluid to a depth of 10cm (see 3.2.4). The probe measuring the azimuthal component of the field gives some sense of the toroidal field present in the system; since the toriodal field does not extend outside the fluid volume, the external array gives no access to this. On the other hand, since these probes only measure two

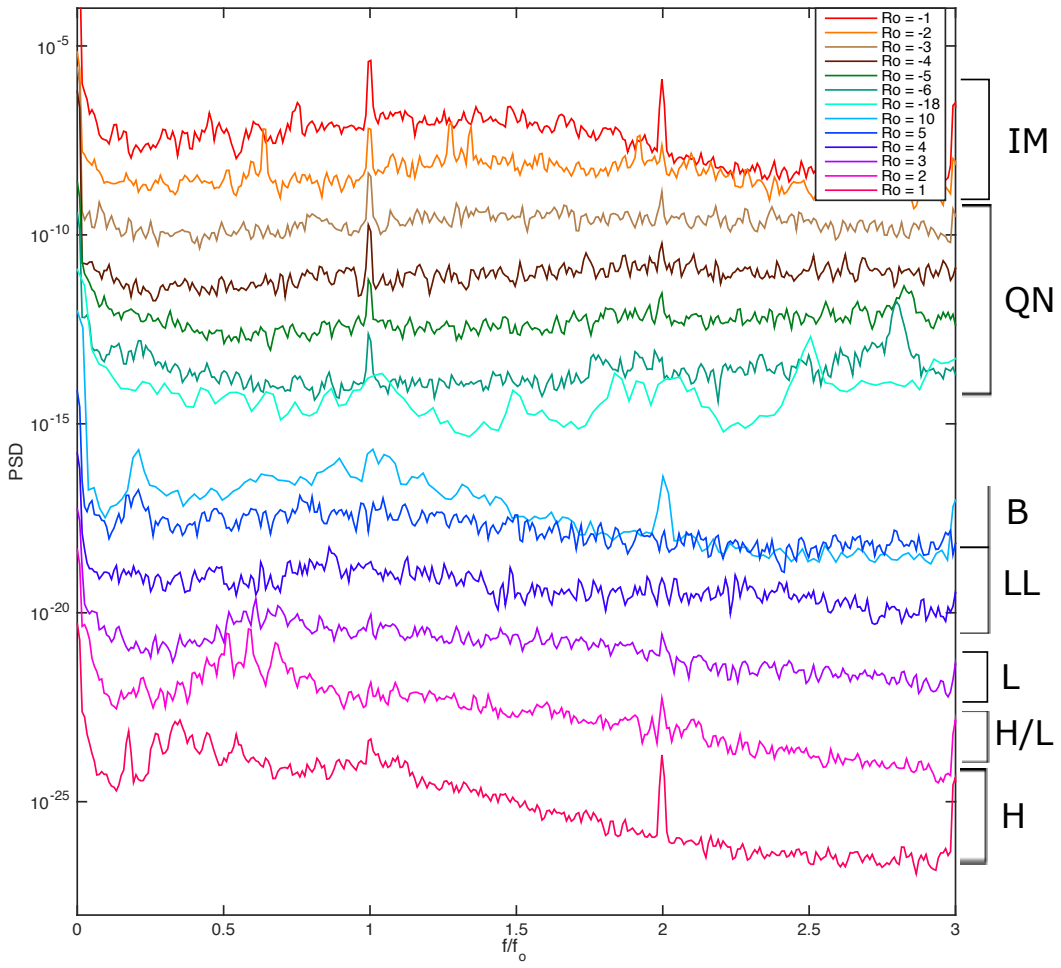

Figure 4.5: Power Spectral Density of induced S_1^0 magnetic field, for the case of a S_1^0 applied field, versus frequency for a variety of Ro. The lines are offset from one another for clarity. The different colors correspond to different Ro, with the ordering following that from the Ro^{-1} torque curve in Figure 4.1, with $Ro^{-1} = -1$ at the top, increasing through $Ro^{-1} = 0$ to $Ro^{-1} = 1$ at the bottom; the corresponding Ro values are given in the legend. The corresponding state labels are indicate on the right side of the figure. Note the sharp spectral features present for some Ro, particularly $Ro = 1, 2$, the significant variation in the amount of power at low frequencies, and in the relative power at $f/f_o = 1$.

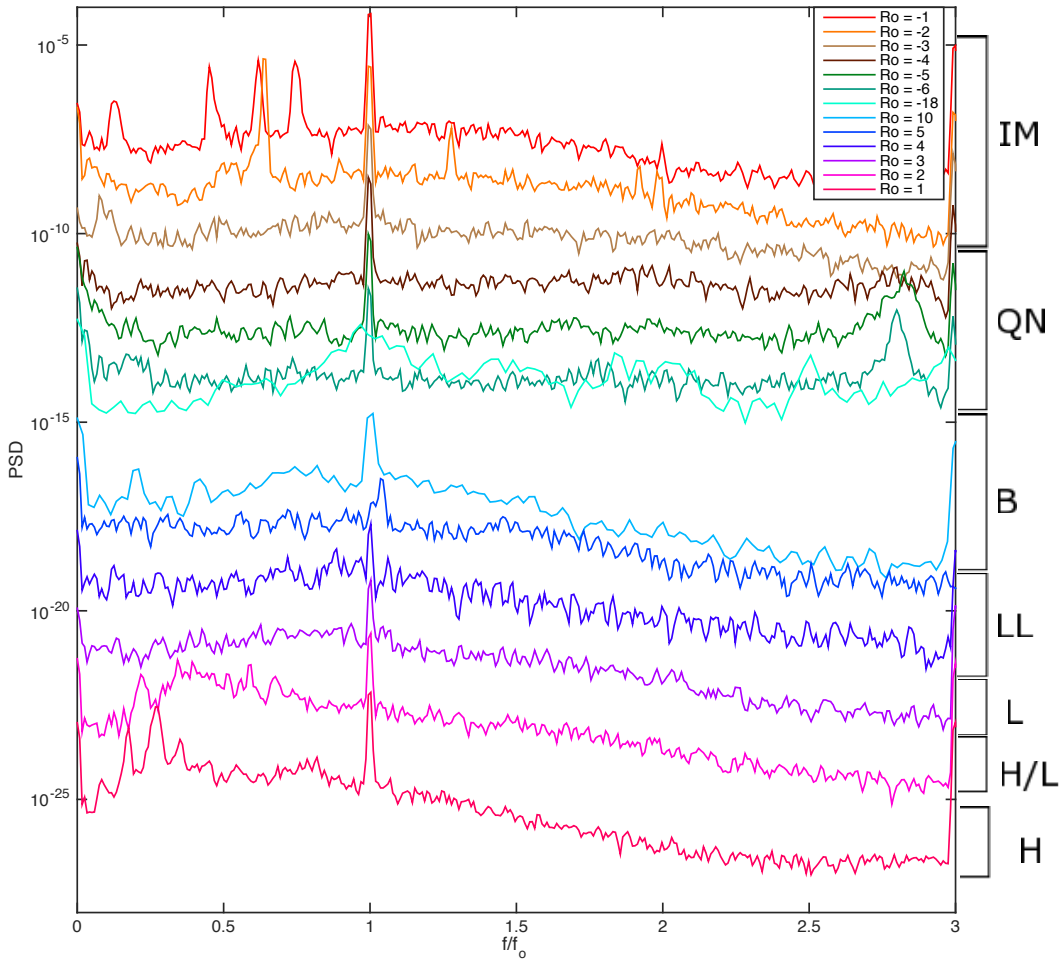

Figure 4.6: Power Spectral Density of induced S_1^1 magnetic field, for the case of a S_1^0 applied field, versus frequency for a variety of Ro. The lines are offset from one another for clarity. The different colors correspond to different Ro, with the ordering following that from the Ro^{-1} torque curve in Figure 4.1, with $Ro^{-1} = -1$ at the top, increasing through $Ro^{-1} = 0$ to $Ro^{-1} = 1$ at the bottom; the corresponding Ro values are given in the legend. The corresponding state labels are indicate on the right side of the figure. Note the sharp spectral features for $Ro = -1, -2$, not present in the previous plot for S_1^0, which are likely associated with inertial modes.

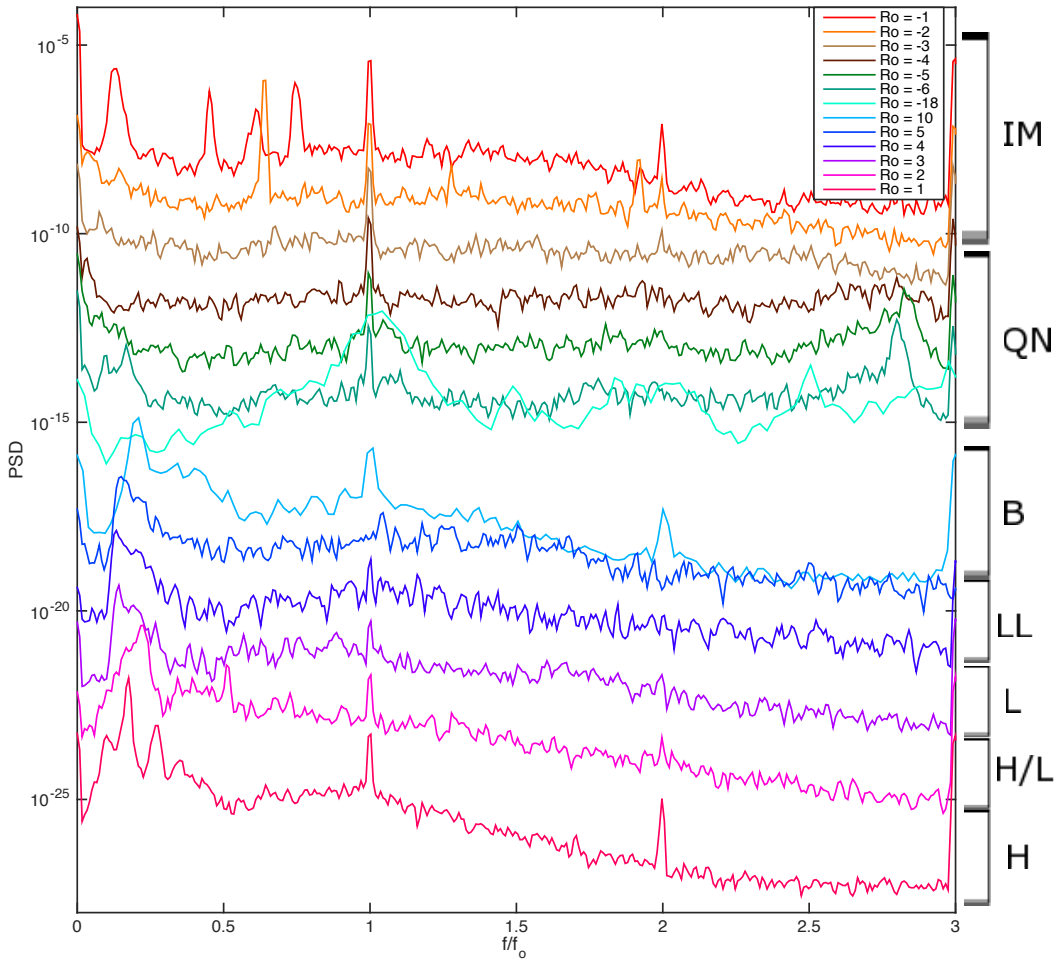

Figure 4.7: Power Spectral Density of induced S_2^1 magnetic field, for the case of a S_1^0 applied field, versus frequency for a variety of Ro. The lines are offset from one another for clarity. The different colors correspond to different Ro, with the ordering following that from the Ro^{-1} torque curve in Figure 4.1, with $Ro^{-1} = -1$ at the top, increasing through $Ro^{-1} = 0$ to $Ro^{-1} = 1$ at the bottom; the corresponding Ro values are given in the legend. The corresponding state labels are indicate on the right side of the figure. Note the very large and broad peak around $f/f_o = 1$ for the $Ro = -18$ curve, corresponding approximately to the torque maximum for this system. Also note that the peaks around $f/f_o = 2.8$ for $Ro = -5, -6$ are especially prominent in this coefficient, and occur in the Quiet Negative (QN) state, indicating that there is some type of wave present in this state as well.

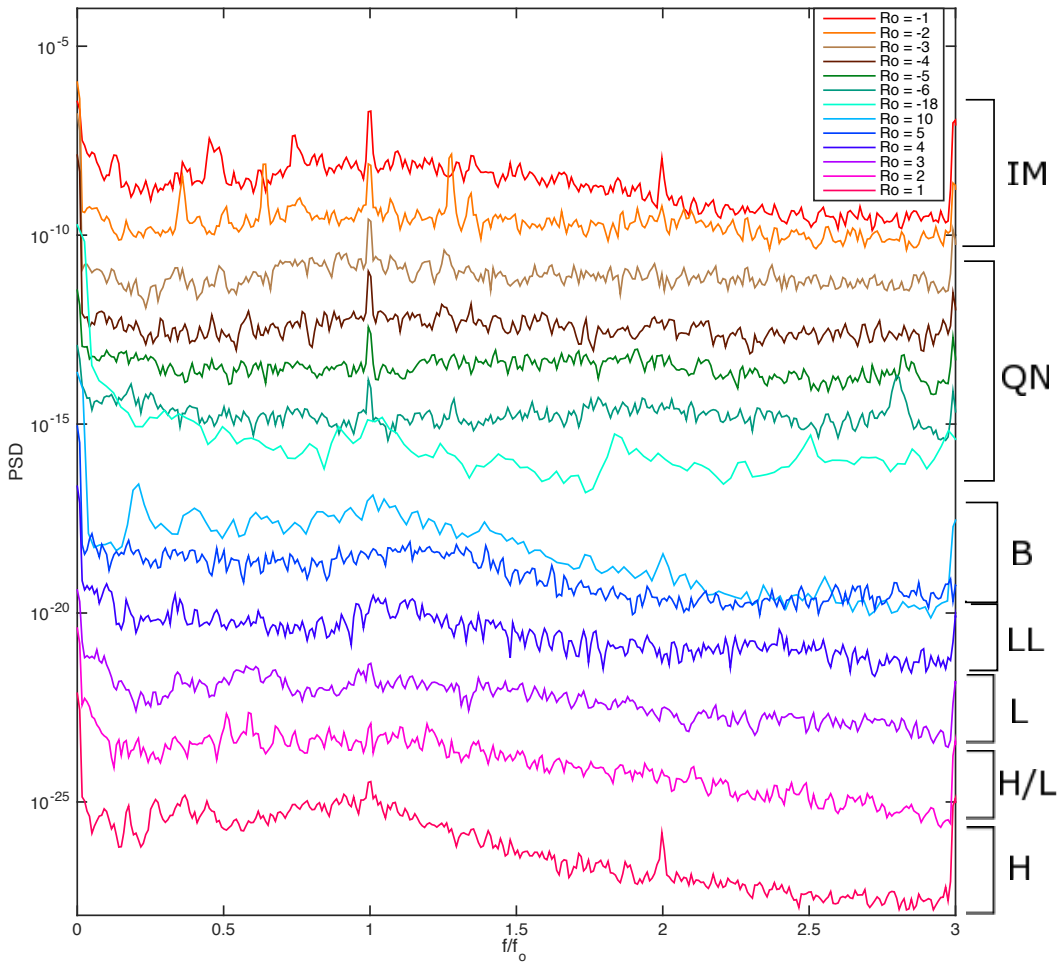

Figure 4.8: Power Spectral Density of induced S_3^0 magnetic field, for the case of a S_1^0 applied field, versus frequency for a variety of Ro. The lines are offset from one another for clarity. The different colors correspond to different Ro, with the ordering following that from the Ro^{-1} torque curve in Figure 4.1, with $Ro^{-1} = -1$ at the top, increasing through $Ro^{-1} = 0$ to $Ro^{-1} = 1$ at the bottom; the corresponding Ro values are given in the legend. The corresponding state labels are indicate on the right side of the figure. Note the large amount of power at very low frequencies for the $Ro = -18$ (torque maximum) state.

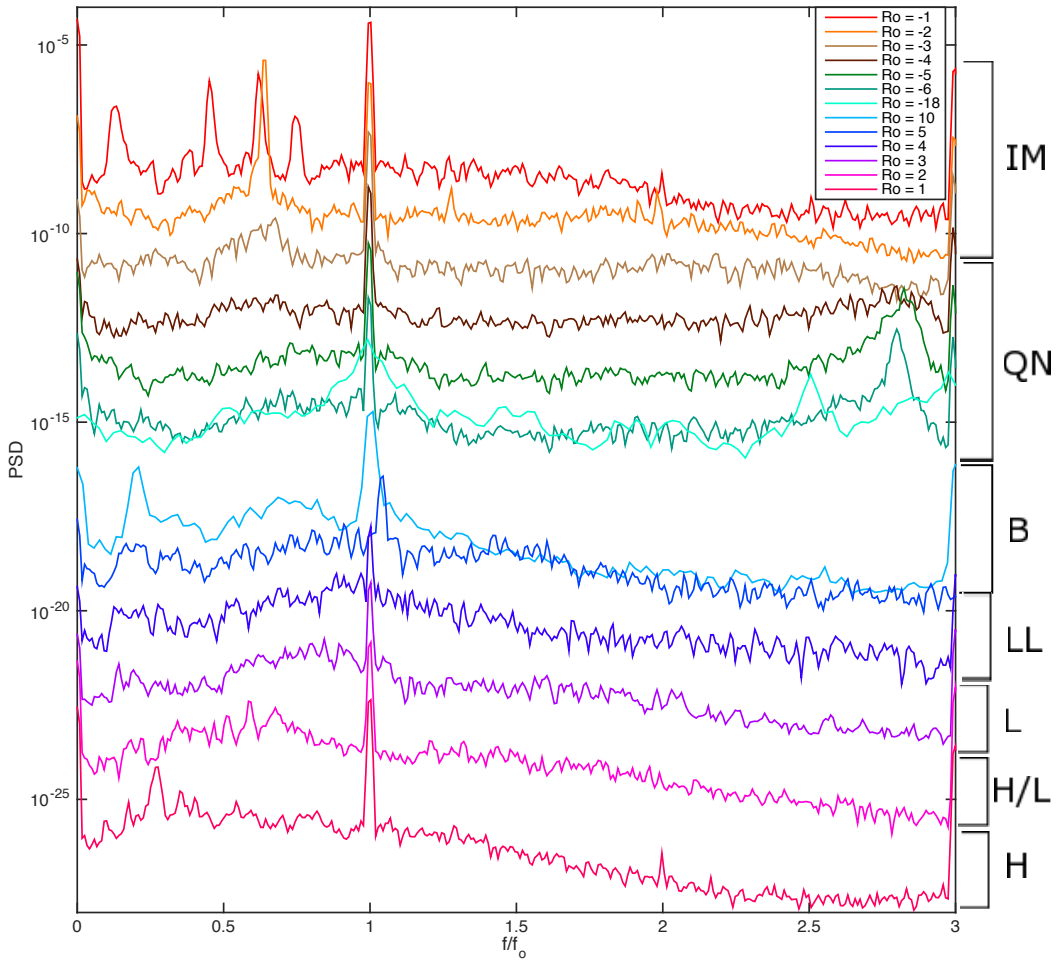

Figure 4.9: Power Spectral Density of induced S_3^1 magnetic field, for the case of a S_1^0 applied field, versus frequency for a variety of Ro. The lines are offset from one another for clarity. The different colors correspond to different Ro, with the ordering following that from the Ro^{-1} torque curve in Figure 4.1, with $Ro^{-1} = -1$ at the top, increasing through $Ro^{-1} = 0$ to $Ro^{-1} = 1$ at the bottom; the corresponding Ro values are given in the legend. The corresponding state labels are indicate on the right side of the figure. Note the peak near $f/f_o = 2.5$ for $Ro = -18$, which may be related to the peaks at $f/f_o = 2.8$ for $Ro = -5, -6$.

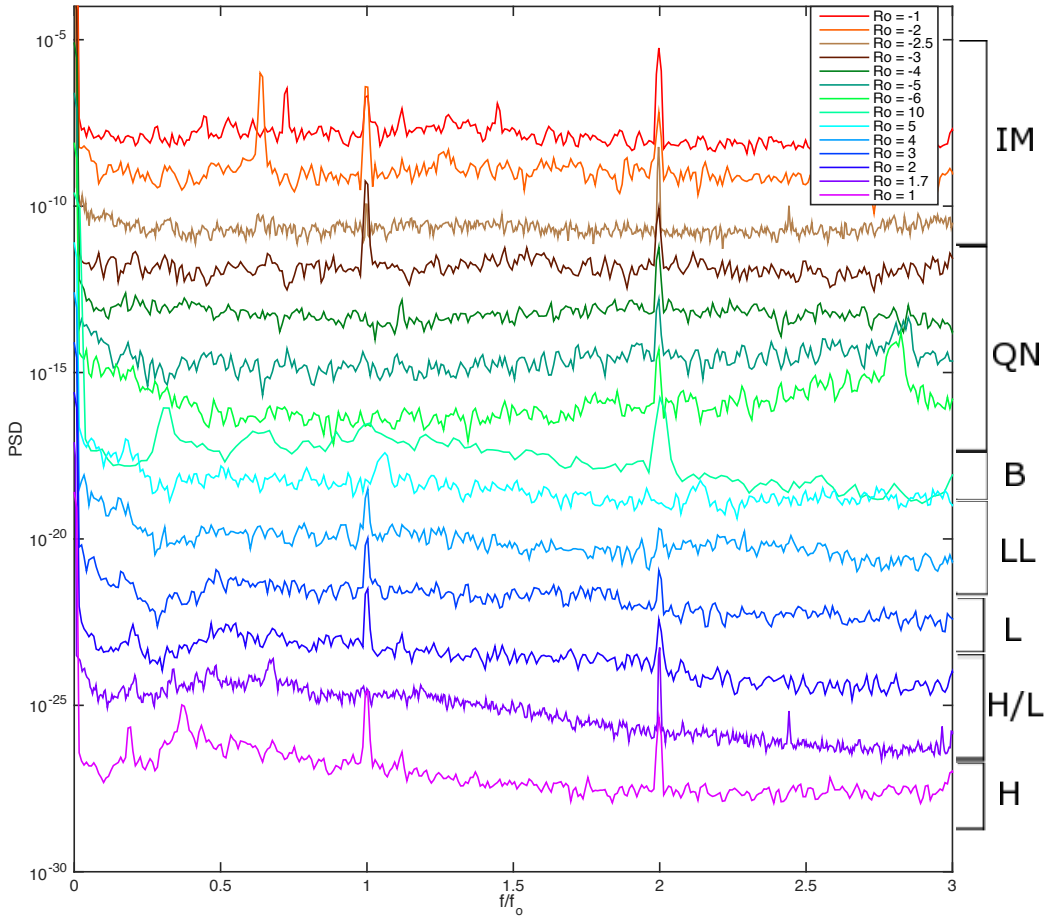

Figure 4.10: Power Spectral Density of induced S_1^0 magnetic field, for the case of a S_2^0 applied field, versus frequency for a variety of Ro. The lines are offset from one another for clarity. The different colors correspond to different Ro, with the ordering following that from the Ro^{-1} torque curve in Figure 4.1, with $Ro^{-1} = -1$ at the top, increasing through $Ro^{-1} = 0$ to $Ro^{-1} = 1$ at the bottom; the corresponding Ro values are given in the legend. Also note that the Ro values shown are not exactly the same as for the case of a S_1^0 applied field. The corresponding state labels are indicate on the right side of the figure. Note how flat many of the spectra are for $Ro < 0$ as compared to the $Ro > 0$ spectra, which have more power at lower frequencies that then falls off at higher frequencies.

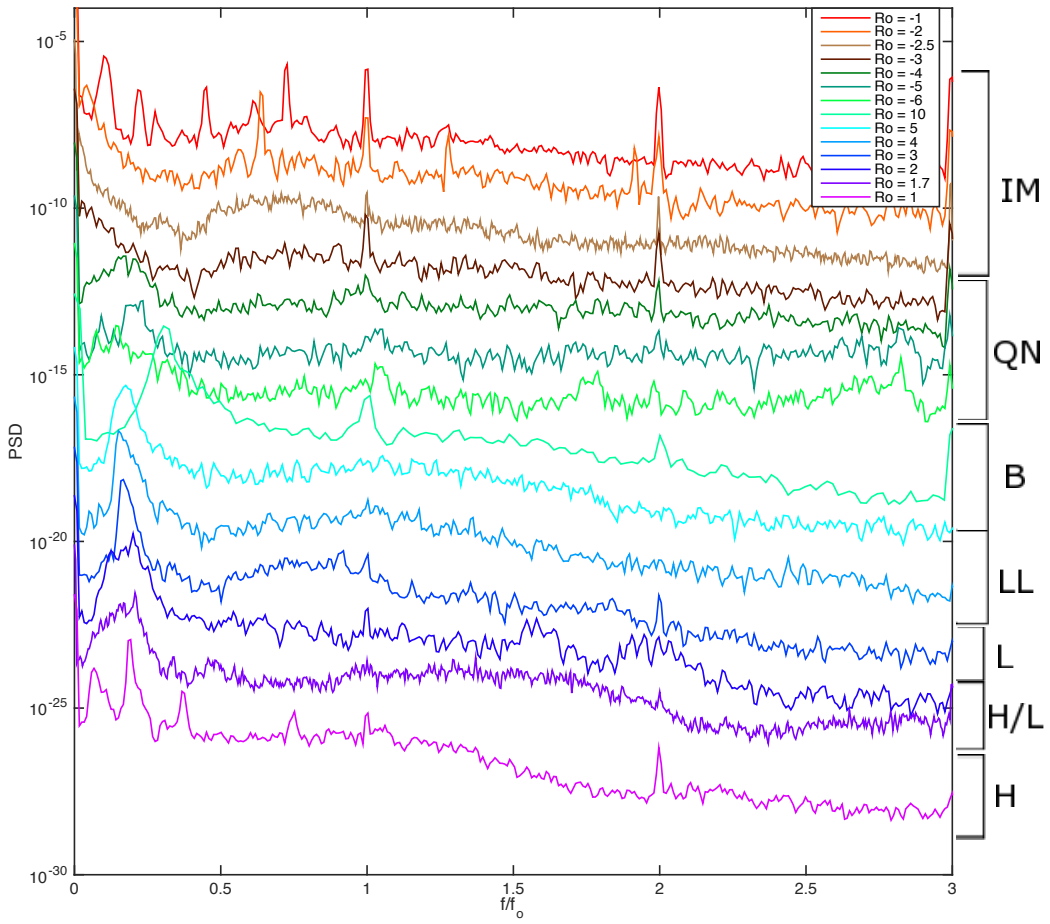

Figure 4.11: Power Spectral Density of induced S_1^1 magnetic field, for the case of a S_2^0 applied field, versus frequency for a variety of Ro. The lines are offset from one another for clarity. The different colors correspond to different Ro, with the ordering following that from the Ro^{-1} torque curve in Figure 4.1, with $Ro^{-1} = -1$ at the top, increasing through $Ro^{-1} = 0$ to $Ro^{-1} = 1$ at the bottom; the corresponding Ro values are given in the legend. Also note that the Ro values shown are not exactly the same as for the case of a S_1^0 applied field. The corresponding state labels are indicate on the right side of the figure. Note the very large, broad peaks around $f/f_o = 0.2$ for $Ro = 1 - 5$.

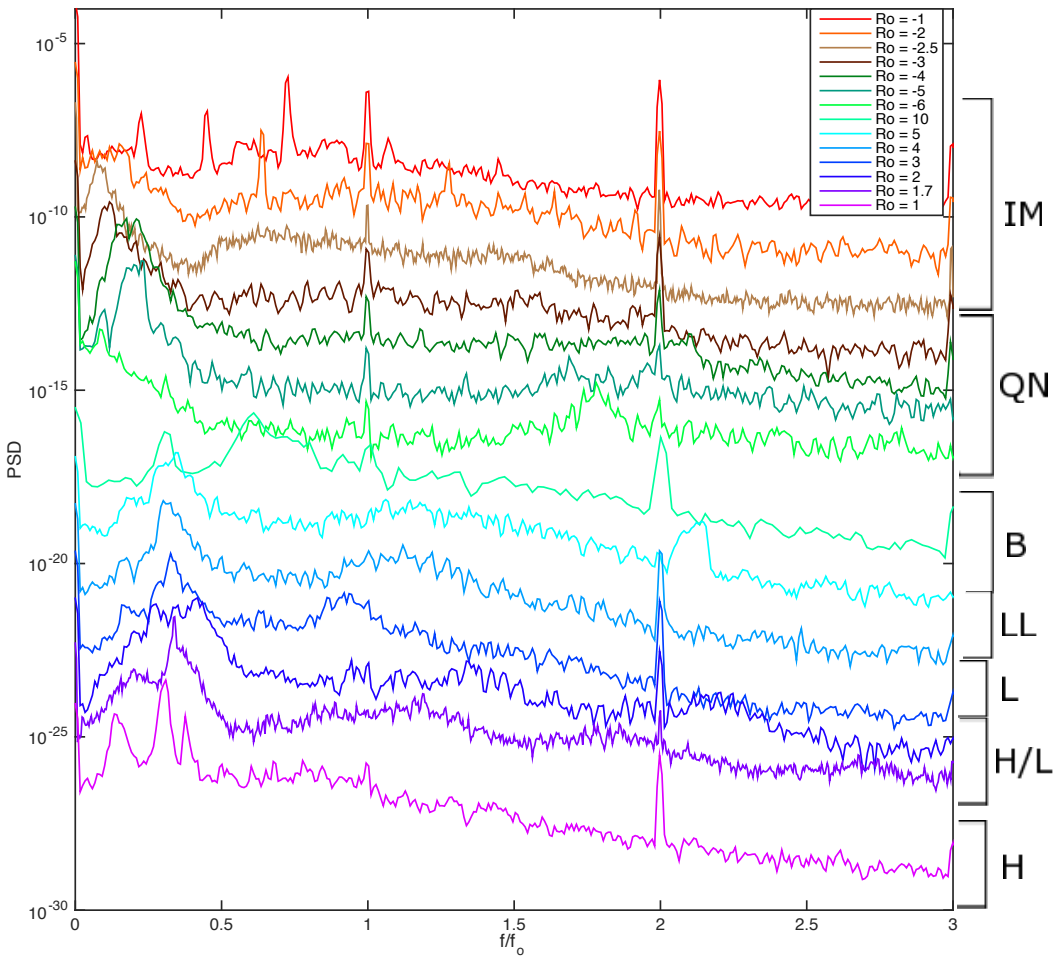

Figure 4.12: Power Spectral Density of induced S_2^2 magnetic field, for the case of a S_2^0 applied field, versus frequency for a variety of Ro. The lines are offset from one another for clarity. The different colors correspond to different Ro, with the ordering following that from the Ro^{-1} torque curve in Figure 4.1, with $Ro^{-1} = -1$ at the top, increasing through $Ro^{-1} = 0$ to $Ro^{-1} = 1$ at the bottom; the corresponding Ro values are given in the legend. Also note that the Ro values shown are not exactly the same as for the case of a S_1^0 applied field. The corresponding state labels are indicate on the right side of the figure. Note the large peaks at low frequency for $Ro = -2.5$ to $Ro = -5$, with the peak around $f/f_o = 0.1$ for $Ro = -2.5$, and shifting up in frequency, to $f/f_o = 0.25$ for $Ro = -5$. Again this shows that there is significant activity in the Quiet Negative state. In addition, the lack of such a peak for $Ro = -6$ may indicate that at this Ro value the flow is in a distinct state from the rest of the states labeled QN.

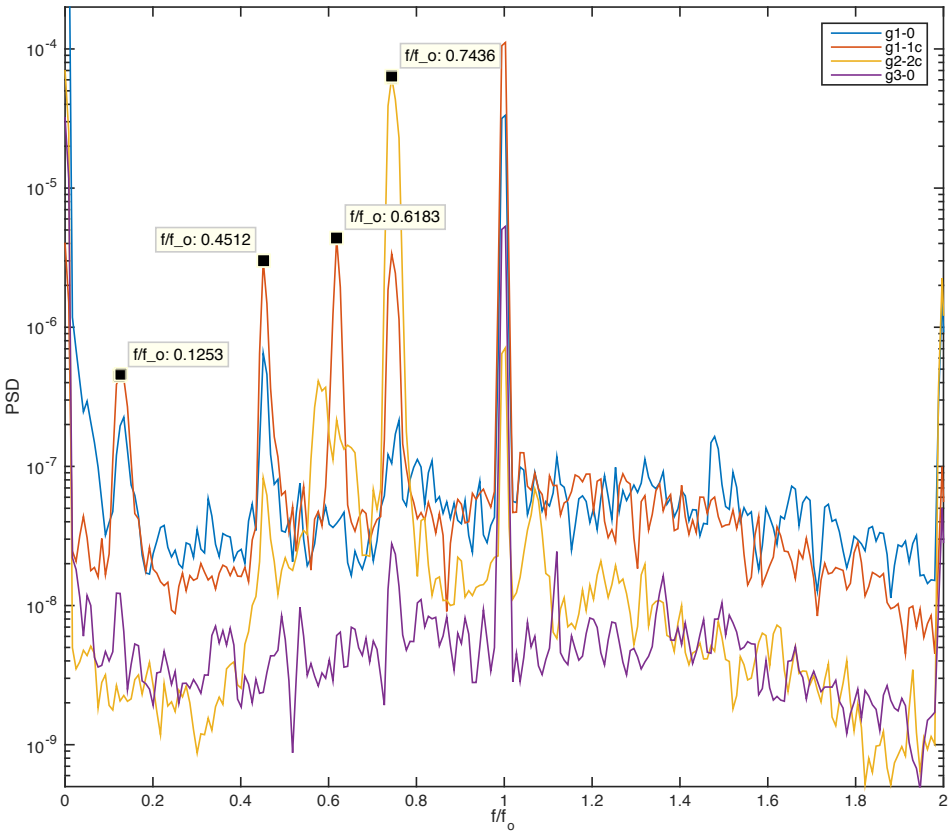

Figure 4.13: Power Spectral Density of main induced magnetic fields, for $Ro = -1$ and an S_1^0 applied field, versus frequency. Note the sharp spectral features below $f/f_o = 1$, which have their frequencies indicated, and the variation in power seen for different Gauss coefficients.

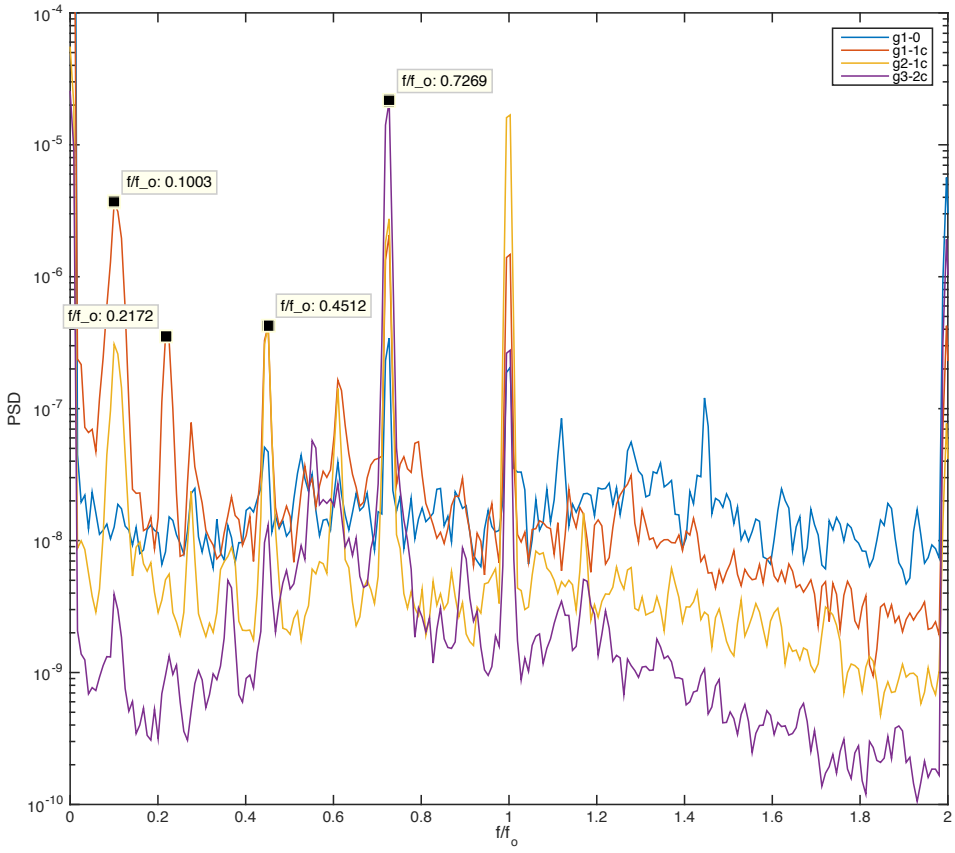

Figure 4.14: Power Spectral Density of main induced magnetic fields, for $Ro = -1$ and an S_2^0 applied field, versus frequency. Note the peak at $f/f_o = 0.2172$, seen here but not for the case of a dipole applied field (Fig. 4.13), indicating that the combination of quadrupole and dipole results may yield more information than just one of them in isolation.

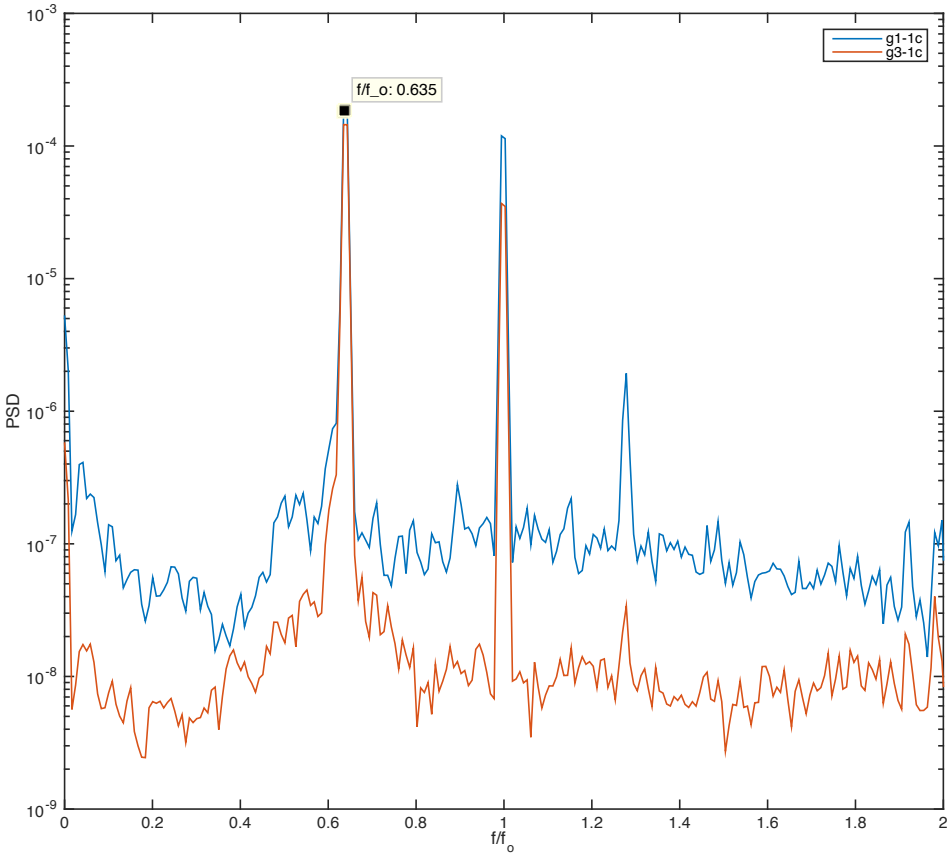

Figure 4.15: Power Spectral Density of main induced magnetic fields, for $Ro = -2$ and an S_1^0 applied field, versus frequency. Note the sharp spectral peak at $f/f_o = 0.635$, likely associated with an inertial mode with $l = 4$ and $m = 1$.

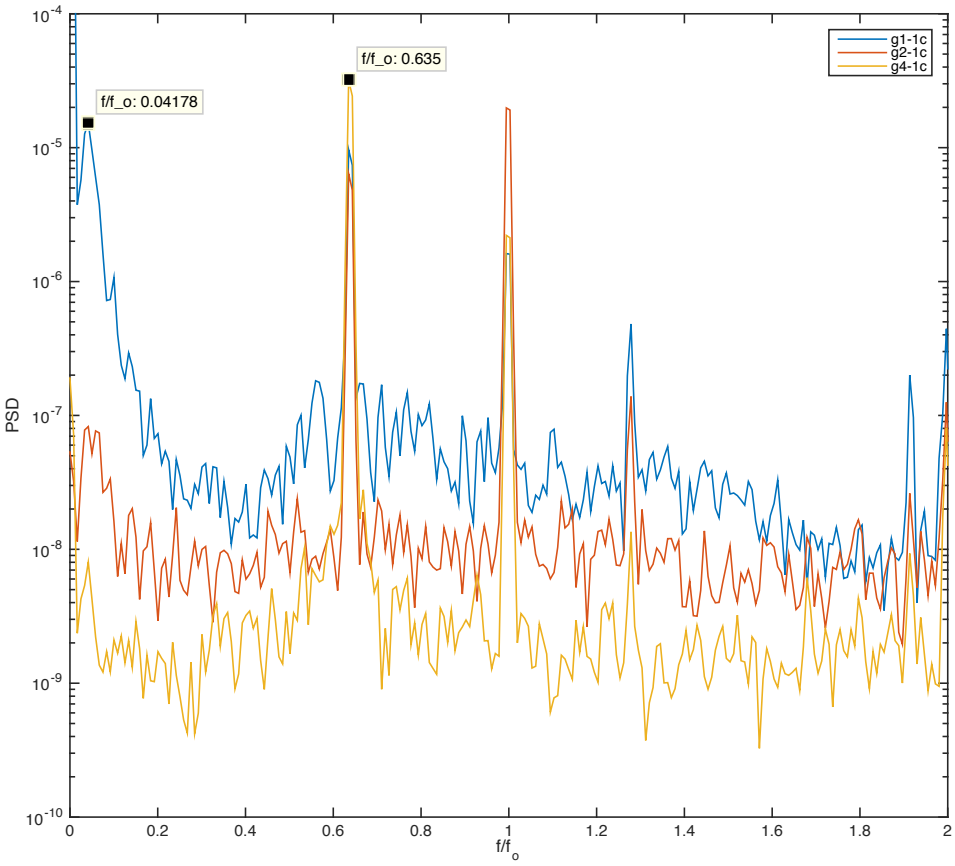

Figure 4.16: Power Spectral Density of main induced magnetic fields, for $Ro = -2$ and an S_2^0 applied field, versus frequency. While the signature of the inertial mode (4,1,0.64) is also seen here, note that the low-frequency $f/f_o = 0.04178$ peak is much more prominent here than for the case of a dipole applied field (Fig. 4.15).

Ro	State Label	Spectral Peaks $(l, m : f/f_o)$	Notes
10	B	(2,1: 0.210), (1,1: 0.210), (3,1: 0.210)	Broadband power at low frequencies in S_1^0
5	B/LL	(1,0: 0.18,0.28), (2,1: 0.150)	Some oscillations in fall off at higher frequencies in S_1^0
4	LL	(2,1: 0.134)	
3	L	(2,1: 0.142)	Low frequency power in S_1^0, also broadband rise around 0.6
2	H/L	(1,0: 0.510,0.593,0.677), (1,1: 0.343,0.0.393), (2,1: 0.223)	Faster fall off in power at higher frequencies for S_1^0
1	H	(1,0: 0.351,0.443,0.543), (1,1: 0.276), (2,1: 0.100,0.176), (3,2: 0.276), (3,1: 0.167)	Inertial mode: (3,1,0.1766)

Table 4.3: Spectral Peaks of Gauss Coefficients in 3 m for various positive Ro. The left column gives the value of Ro. The second column gives the state label, discussed in the text. The third column lists the spectral peaks seen, with the l and m of the Gauss coefficient given, and their frequencies, normalized by the outer sphere rotation rate. A "b" appended to the frequency value indicates that it is a broad spectral feature, rather than a sharp peak. The final column contains comments about the states where appropriate.

Ro	State Label	Spectral Peaks $(l, m : f/f_o)$	Notes
-1	IM	(1,0: 0.142,0.443,0.5), (1,1: 0.125,0.45,0.618,0.744), (2,2: 0.577,0.744), (2,1: 0.134)	Inertial mode: (3,2,0.75)
-2	IM	(1,1: 0.635,1.278), (1,0: 0.359), (3,1: 0.64)	Inertial mode: (4,1,0.64)
-3	QN	(1,0: 0.042), (1,1: 0.117,0.075)	
-4	QN	(2,1: 0.033), (3,1: 2.8b), (2,1: 2.8b), (3,2: 0.0334,0.292,1.6b)	
-5	QN	(1,1: 2.8b), (1,0: 2.8b,3.5b), (2,1: 0.167,2.8b), (3,1: 2.8b)	
-6	QN	(1,0: 2.8b,3.5b), (1,1: 0.215,2.8b), (2,1,: 0.167,2.8b), (3,1: 2.8b)	
-18	QN	(1,0: 4b)	Broadband power at low frequencies, oscillations in S_1^1 spectra as it falls off

Table 4.4: Spectral Peaks of Gauss Coefficients in 3 m for various negative Ro. The left column gives the value of Ro. The second column gives the state label, discussed in the text. The third column lists the spectral peaks seen, with the l and m of the Gauss coefficient given, and their frequencies, normalized by the outer sphere rotation rate. A "b" appended to the frequency value indicates that it is a broad spectral feature, rather than a sharp peak. The final column contains comments about the states where appropriate.

components of the field at one location, we cannot build up a global picture of the full magnetic field within the fluid, as can be done for the external field using the array. Another advantage of these internal probes is their sensitivity to higher frequency fluctuations in the flow; the external probes are somewhat shielded from the flow by the vessel and thus have a cutoff frequency above which they do not see magnetic fluctuations in the flow.

In Figures 4.17 and 4.18 we have plotted the spectra of these two probe measurements for a variety of Ro. The spectra are plotted versus frequency normalized by the outer rotation rate, and we see similar features to those noted above in the spectra of various Gauss coefficients. For $Ro = -1$ and $Ro = -2$ there are sharp spectral features below $2f_o$ corresponding to inertial modes. For the other Ro, the only sharp spectral features correspond to the outer rotation rate and its harmonics. For the QN states, $Ro = -3, -4, -5, -6, -18$, we note that there is a somewhat sharp spectral feature below $3f_o$ that was found above in the Gauss coefficient spectra, but here it is clear that this feature is also present for $Ro = -3$ and $Ro = -4$. It becomes more prominent for $Ro = -5$ and $Ro = -6$ where it also shows up in some of the Gauss coefficient spectra.

Moving on to the case of positive Ro, for the high torque state, for the B_ϕ spectra there is strong broadband power at low frequencies, but no distinct spectral peaks (other than at f_o at harmonics), while B_s shows similar spectral content at low frequencies to that found in the Gauss coefficients. For larger Ro, the spectra start to exhibit oscillations, with several broad peaks one after another in the spectra. Finally, for the B state, the spectra of B_ϕ is relatively featureless, while the spectra

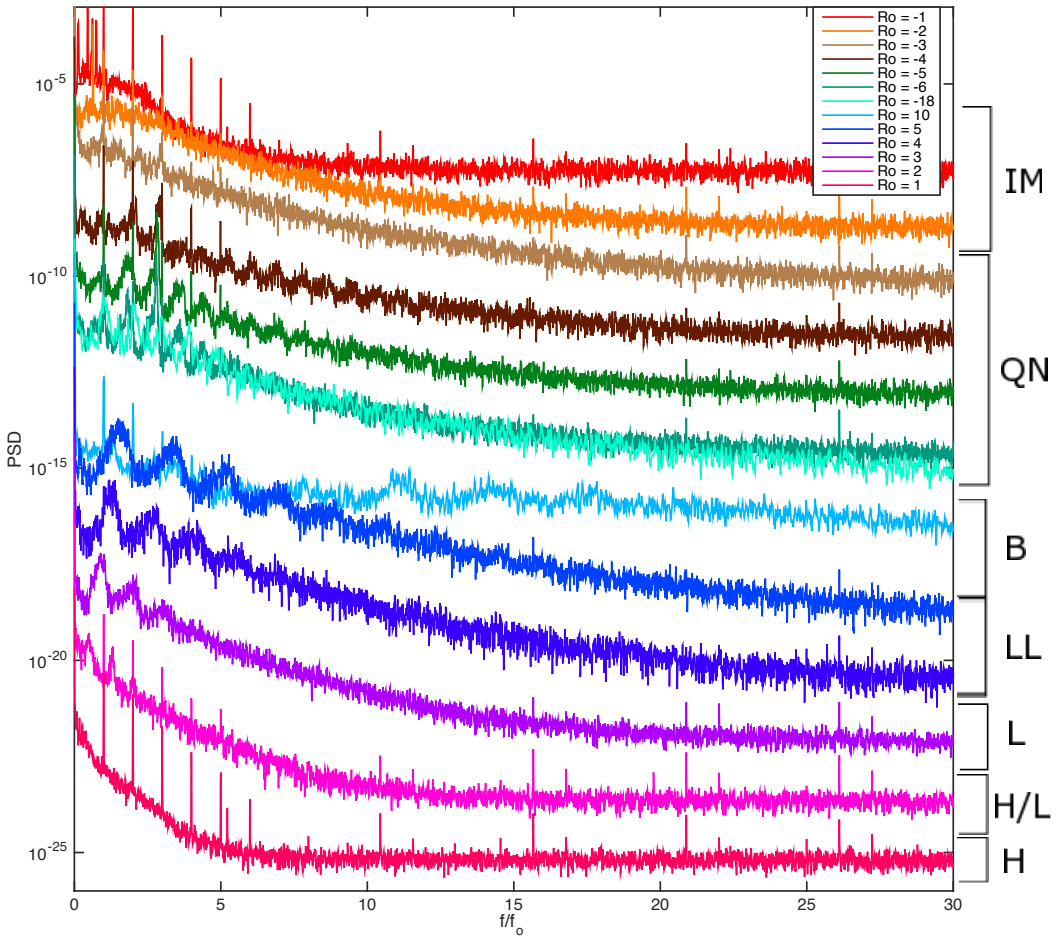

Figure 4.17: Power Spectral Density of locally measured internal azimuthal magnetic field, for the case of a S_1^0 applied field, versus frequency for a variety of Ro.

of the B_s shows a spectral peak around $0.210 f_o$ similar to what was found in the Gauss coefficient spectra in S_2^1, S_1^1, and S_3^1.

In addition to the internal field measurements, we also have pressure measurements, from probes in 3 of the instrumentation ports. Some of these are presented in section 5.6 below, in regards to looking for acoustic modes in the 3 m experiment.

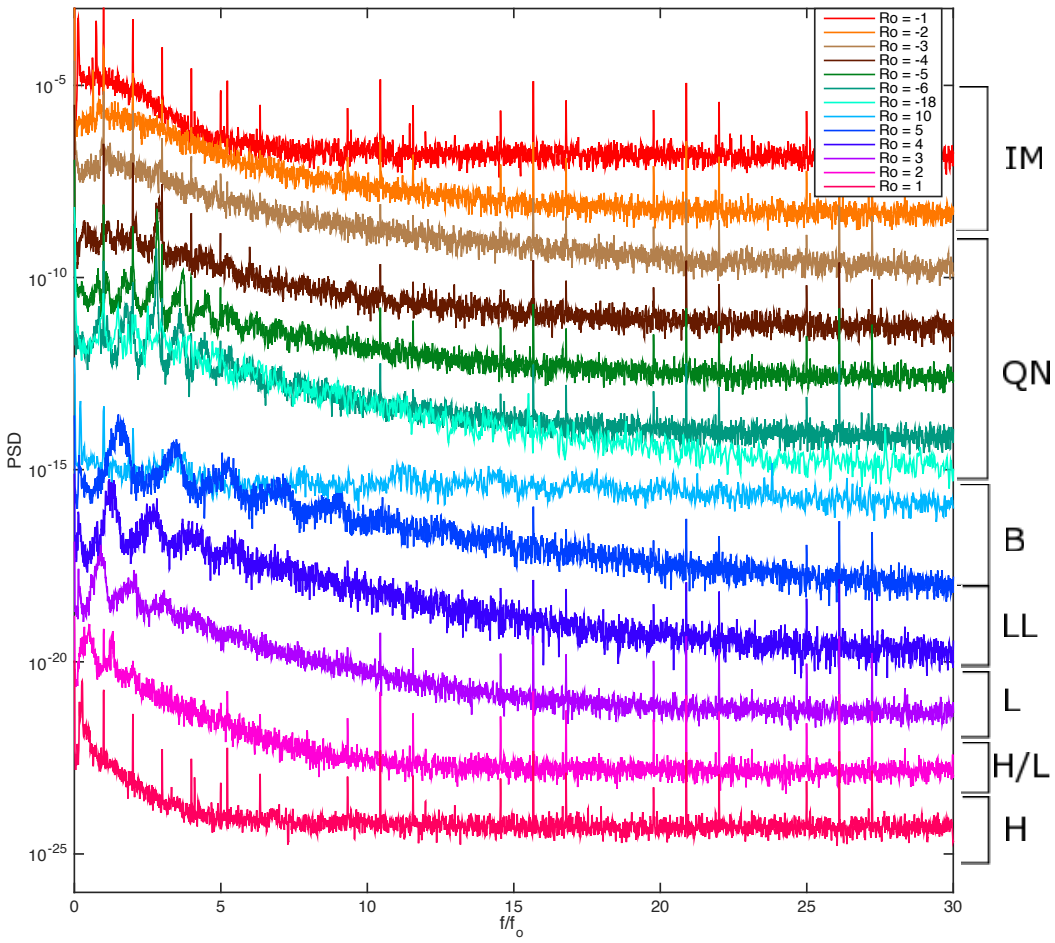

Figure 4.18: Power Spectral Density of locally measured cylindrical radial magnetic field, for the case of a S_1^0 applied field, versus frequency for a variety of *Ro*.

Chapter 5: Acoustic Studies

In this chapter we review the results of acoustic studies in gas experiments in the 60 cm experiment, and also discuss efforts at measuring acoustic modes in the 3 m liquid sodium experiment.

5.1 Computed Modes

As noted in section 2.3.2, the calculation of the acoustic modes of a whole sphere, or simple spherical shell (i.e. inner and outer spherical surfaces without a shaft or other geometrical complications), is straightforward numerically speaking: one has only to find the roots of equations involving Bessel functions. To get better estimates of mode frequencies, as well as to more precisely determine the sensitivity of the modes to flows within the cavity, a more accurate model of the acoustic cavity of the experiment is required. Mode frequency predictions based on this model are then compared in detail to experimental acoustic measurements.

We worked with seismologist Ved Lekic and his Master's student Anthony Mautino, who constructed a finite-element model of the 60 cm experiment to more closely approximate the geometry of the experiment. This is an axisymmetric model; in order to determine the mode frequencies and structures, for each value of az-

imuthal wavenumber m the scalar Helmholtz wave equation in pressure is solved. To do this, a specific m is selected, and then the equation is rewritten using a quasi-2D acoustic operator with the choice of m built in, and is solved over a 2D domain comprising a meridional slice of the model of the experiment. It is solved by using a piecewise linear isoparametric finite element formulation on a highly regular mesh to calculate the stiffness and mass matrices. The eigenvalues and eigenvectors are solved using ARPACK, with sparse Lanczos iteration. For more details see the forthcoming Master's thesis of Anthony Mautino.

An example of the structure of a mode calculated in this way is shown in Figure 5.1. The colors indicate the pressure field in a meridional plane of the acoustic mode labeled (2,3,2). Since $l - m = 1$, this mode has one node on the outer surface, located at the equator; since $n = 2$ there are two radial nodal lines between the inner and outer spheres. Note also the presence of both the inner sphere and the outer shaft that projects from the poles of the outer sphere towards the inner sphere. This pressure pattern is an eigenvector of the acoustic operator, and the associated eigenvalue gives the mode's frequency (we assume the speed of sound in the fluid is uniform). In Figure 5.2 the sensitivity kernel (K_{nlm} of eq. 2.48) of this same mode (2,3,2) is given. Here the colors indicate the amplitude of the frequency shift expected in this mode as a function of location in the meridional plane, for a given rotation pattern in the flow. In particular, note that the kernel is symmetric about the equator; as in helioseismology this is a limitation of only considering (or analyzing) the coupling of isolated modes with the flow, in that asymmetries between the northern and southern hemispheres are not detectable. We could detect

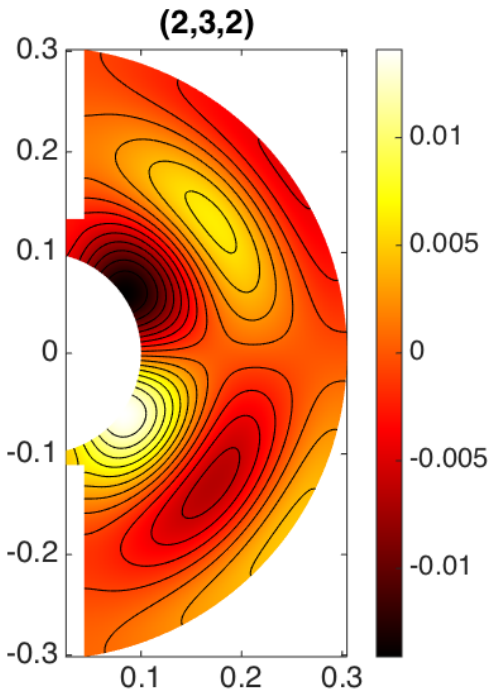

Figure 5.1: Example of Calculated Mode Pressure Pattern. The pressure pattern of the (2,3,2) mode. Figure credit: Anthony Mautino.

odd degree structure that would be sensitive to hemispheric differences if we were to compute coupling among the modes. Also, note that all the values are negative, indicating that positive m modes will have their frequencies shift lower, and negative m modes shift higher, due to flows in the positive azimuthal direction. This splits the frequencies of $\pm m$ pairs, here $m = \pm 2$, that otherwise have equal (degenerate) frequencies.

5.2 Observed Modes: Stationary Case

For the case of a stationary system (both inner and outer spheres at rest), $\pm m$ modes will have the same frequency, and the splittings of modes with different $|m|$

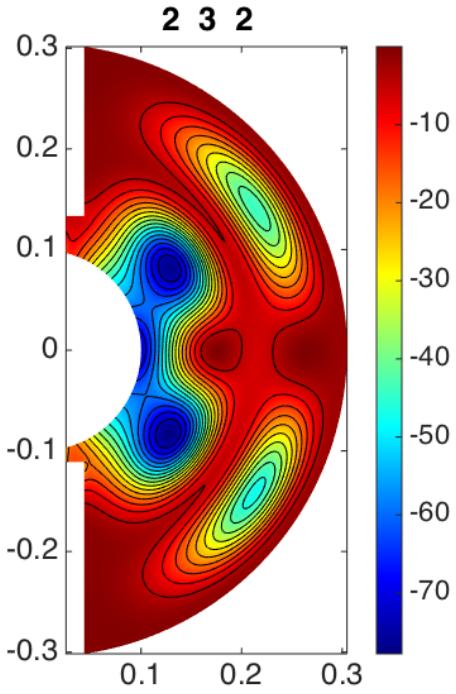

Figure 5.2: Example of Calculated Mode Kernel. The kernel of the (2,3,2) mode. This gives the sensitivity of the mode to fluid velocities as a function of position in the (r, θ) plane. Figure credit: Anthony Mautino.

within a given (n,l) family will be due to the departure of the system from spherical symmetry (mainly due to the large cylindrical shaft that extends above and below the inner sphere, but also any deviations in the shape of the outer shell and inner sphere away from perfect sphericity). Since there is no ambient noise due to the rotation of the experiment or fluid flow between the spheres, we excite the modes using a speaker. This is done by playing a chirp using one of the installed speakers, and simultaneously recording the sound inside the experiment. As described in more detail in section 3.1.3, we could simultaneously record on two (of six possible) microphones, while acoustically exciting the system with one of two speakers.

The acoustic excitation used was generally a chirp, that is rising tone, generated by sending a signal $s(t)$ to the speaker consisting of a sine wave with a frequency that varies linearly in time t:

$$s(t) = \sin(2\pi(f_{inital}t + \frac{f_{final} - f_{initial}}{2t_{chirp}}t^2)) \tag{5.1}$$

where $f_{initial}$ and f_{final} are the initial and final frequencies of the chirp signal, respectively, and t_{chirp} is the duration of the chirp. Typically these chirps lasted for 30 seconds, with a frequency that varied over a bandwidth from around 10 Hz to 2 kHz or often from about 50 to 200Hz. When the frequency of the chirp is near that of one of the modes of the cavity, the mode is resonantly excited and a large amplitude acoustic response is observed. Looking at the power spectrum of the microphone recordings, we can then identify peaks corresponding to acoustic modes.

Some of the acoustic modes that have been experimentally identified in the

60 cm experiment are listed in Table 5.1. The list of predicted mode frequencies is provided by Mautino, using a speed of sound $c = 348$ m/s. The modes are listed in order of increasing predicted frequency, and identified by their mode numbers, $(n, l, |m|)$. The n and l numbers for a given mode are determined by examining its structure from the calculations done by Mautino; information about l and m can also be inferred from the experiments by making use of the relative phase between the two recording microphones. Specifically, the parity of $l - m$ and of m (i.e. whether these are even or odd) can be determined if recordings from the appropriate pair of microphones are available.

By using microphones located at the same azimuth but at opposite latitudes (e.g., mics 1 and 4), the $l-m$ parity (i.e. whether $l-m$ is even or odd) can be found, determining whether the mode is equatorially symmetric or anti-symmetric. To do so, first both signals are bandpassed around the frequency range of the chirp used, and then their signals are normalized to have the same amplitude, and the sum and difference of these filtered and normalized time series are taken. The power spectral density of the sum and the difference is then taken; modes with $l-m$ even will appear in the sum signal, while modes with $l-m$ odd will appear in the difference signal. An example of this approach can be seen in Figure 5.3. Also, we note that the difference of the signals will tend to reduce any correlated digital noise on the signals, and in the case of differential rotation discussed below, the differences of the signals often have notably lower noise floors than the sums of the signals. Similar to the approach in determining $l - m$ parity, by using microphones located at the same latitude but separated in azimuth by π radians (e.g., mics 1 and 2), the m-parity of a mode

(n,l,m)	f_{pred}	Symm.: Eq.,Az.	Obs. Freq.	% error
(0,1,1)	346	S,O	346.0	0.00
(0,1,0)	365	A,E	367.0	0.54
(0,2,1)	570.2	A,O	569.5	0.12
(0,2,2)	593.0	S,E	594.5	0.25
(0,2,0)	612	S,E	616	0.65
(0,3,1)	774	S,O	775	0.13
(0,3,2)	806.7	A,E	807.5	0.10
(0,3,3)	808.8	S,O	810.5	0.21
(0,3,0)	838	A,E	843	0.60
(1,0,0)	932	S,E	936	0.43
(0,4,1)	970	A,O	972	0.21
(0,4,2)	1008.9	S,E	1010.0	0.11
(0,4,3)	1013.6	A,O	1015.0	0.14
(0,4,4)	1013.7	S,E	1015.5	0.18
(1,1,1)	1045.4	S,O	1048.0	0.25
(0,4,0)	1056	S,E	1063	0.66
(1,1,0)	1071	A,E	1080	0.84
(0,5,1)	1165	S,O	1168	0.26

Table 5.1: Identified Acoustic Modes. In addition to comparing the observed and predicted frequencies, mode identification was facilitated by looking at the symmetries of the mode: S,A refer to the symmetry of the mode about the equatorial plane (S for symmetric or A for anti-symmetric), and E,O refer to the whether the azimuthal wave number is even or odd, respectively. The gravest mode (0,1,1) was used to calibrate the temperature of the system, thus giving an exact match between its predicted and observed frequencies; the 0 % error for it is an artefact of this calibration. Prediction Data Credit: Anthony Mautino.

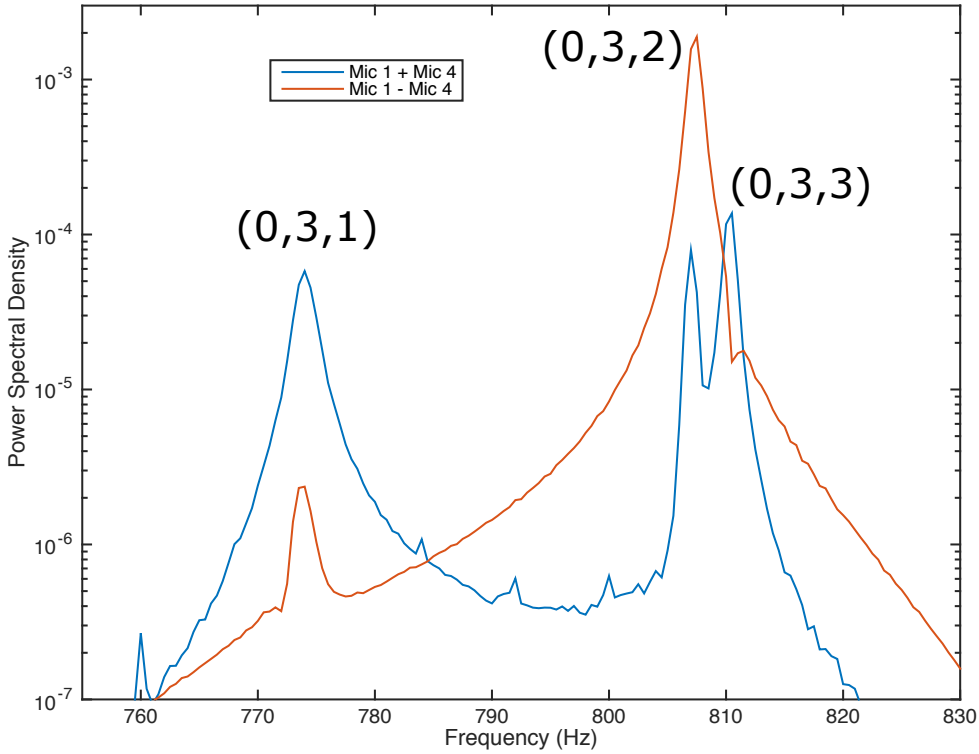

Figure 5.3: Modes $(0, 3, 1)$, $(0, 3, 2)$, and $(0, 3, 3)$ identified in a plot of the logarithm of power spectral density vs. frequency. This data was taken with the experiment stationary, and with a chirp from 700 to 900 Hz. The modes with $l - m$ even have much higher peaks in the sum curve, while the $l - m$ odd mode has a higher one in the difference curve.

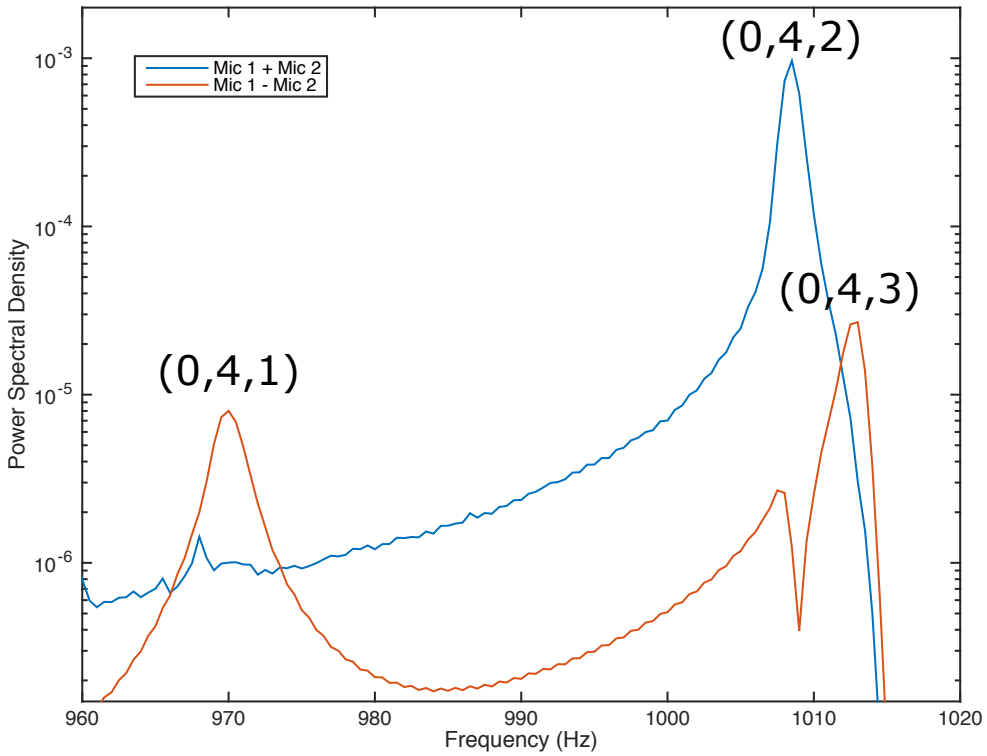

Figure 5.4: Modes $(0, 4, 1)$, $(0, 4, 2)$, and $(0, 4, 3)$ identified in a plot of the logarithm of power spectral density vs. frequency. This data was taken with the experiment stationary, and with a chirp from 940 to 1015 Hz. The mode with m even shows up prominently in the sum curve, while the m odd modes are prominent in the difference curve.

can be determined. An example of this can be seen in Figure 5.4. Using these two parities and the observed frequency of a given mode, the modes up through 1kHz can be identified unambiguously. In Table 5.1, the modes are labeled as equatorially symmetric (S) or anti-symmetric (A), with even (E) or odd (O) m-number, and if this spatial structure has been observed in the experiment, that is noted in the column giving information about experimental observations. Note that given the limitations of the current experimental set-up (only obtaining simultaneous data from two microphones), two experiments must be conducted to get both parities for a given mode. Another possible set-up is to use two closely spaced microphones located at the same latitude to extract information about the m-value (like Mics 5 and 6 of our setup). For the stationary case, however, this does not work since the $+m$ and $-m$ modes have the same frequency and can form a standing wave pattern; thus to get the absolute value of m associated with a given peak, one would need to make use of amplitude information as well, which is more challenging than using more easily extracted phase information. It also turned out that our m-finder setup (Mics 5 and 6) was note effective in determining m for the rotating case. Probably they were spaced too closely given our sample rate, so that the expected phase shifts between them for the modes we were observing were comparable to the smallest ones possible to measure. With the good agreement found between the mode frequency predictions of Mautino's model and the experimental results, however, modes can be identified by frequency without having both parities. Moreover, when measurements from a range of rotation rates are available, the splitting of $\pm m$ modes, with the amount of splitting being approximately proportional to m, can also be used to help

in identifying modes.

5.3 Observed Modes: Solid Body Rotation

Moving to non-stationary cases, the simplest state is that of solid body rotation, with the inner and outer spheres rotating at the same rate. In this case, the fluid simply rotates at the same angular velocity (barring effects due to precessional forcing, which are small for the cases considered here) and the only splitting of $\pm m$ mode pairs is due to the Coriolis force. This case serves as a useful test of the model of the acoustic modes, since the expected flow (solid body rotation) is known. Thus instead of doing the inverse problem of determining the flow from the splittings, we can perform the forward problem of calculating the expected splittings of modes due to a known flow. In this way we can validate the calculated mode structures, which in turn determine their sensitivities to the flow.

We measured the splittings for a number of different modes for the case of solid body rotation, and compared the frequency splitting with the calculated splittings. Splittings for nine different modes were used for three different rotation rates: 5 Hz, 10 Hz and 15 Hz. As expected [92], the splittings appear linear with the rotation rate of the system (for a given state). Thus it is natural to normalize the amount of splitting of a given mode δ_{nlm} by the overall rotation rate f. In Table 5.2 we compare this normalized predicted amount of splitting for each of the nine modes with the measured splitting at three different rotation rates, again normalized by the overall rotation.

The modes used are most of the nonzero m modes with frequencies up to about 1 kHz. The $m = 0$ modes do not split, though they can be used to help determine the speed of sound in the system, which varies with temperature and thus can and do vary between experimental runs. Temperature changes cause shifts in the frequencies of all modes, proportional to the change in the speed of sound, but do not have a significant effect on the values of the splittings. Mautino has also not detected frequency shifts due to nonuniform temperature profiles in the experiment; such effects appear to be below the detection limit given other noise limitations (see Mautino's forthcoming Master's Thesis). Also, a couple of the modes in this range (0 to $\sim$ 1 kHz) were not used because of the noisy nature of the power spectra for their peaks, perhaps a result of the location of the microphones used and the geometry of these modes. For the measurements, empirically it was found that there was often an optimum rotation rate range for measurements, with splittings being small and hard to conclusively identify for low rotation rates, while for the highest rotation rates the mechanical noise of the experiment eventually again made splitting measurements difficult. In Table 5.2 this can be seen in the errors, with the largest errors for most modes seen either at 5 Hz or at 15 Hz. Overall we find excellent agreement between the predictions and observations, with most errors being around the percent level or less.

Mode	Predicted $\frac{\Delta_f}{f}$	$\frac{\Delta_5}{5}$	% error	$\frac{\Delta_{10}}{10}$	% error	$\frac{\Delta_{15}}{15}$	% error
(0,1,1)	0.660	0.660	0.07	0.664	0.60	-	-
(0,2,1)	0.214	0.213	0.35	0.212	0.58	0.205	4.1
(0,2,2)	0.728	0.730	0.25	0.725	0.44	0.707	3.0
(0,3,2)	0.459	0.455	0.80	0.460	0.30	0.462	0.66
(0,3,3)	0.704	0.700	0.58	0.700	0.58	0.708	0.60
(0,4,2)	0.315	0.310	1.44	0.317	0.95	0.315	0.15
(0,4,3)	0.502	0.460	8.4	0.503	0.10	0.500	0.40
(0,4,4)	0.670	0.650	3.0	0.673	0.36	0.687	2.5
(1,1,1)	0.135	0.155	15.1	0.150	11.4	0.132	2.2

Table 5.2: Comparison of Predictions of Acoustic Mode Splittings with Observations for the case of solid body rotation. Most of the nonzero m modes up to a frequency of about 1kHz are used; (0,3,1) and (0,4,1) had complicated peaks that were difficult to extract splittings from. Mode prediction credit: Anthony Mautino.

5.4 Observed Modes: Differential Rotation

With the inner and outer spheres differentially rotating, it has been found empirically that the acoustic modes are excited without any excitation chirp needed, and that in fact the presence of a chirp does not enhance the prominence of the acoustic mode peaks above the background (and note that given the limitations of the speaker we were using, we could not further increase the volume of the chirp). This excitation is either from the turbulence in the flow, or from the mechanical noise of the experiment (bearings, motors, etc.), or some combination of the two.

Splittings of the lowest lying modes are generally easy to identify (see Figure 5.5), while for higher-order modes the peak structure becomes more complicated. Some of the $m = 0$ modes show fairly simple, easily identifiable peaks (e.g. $(0, 1, 0)$ for most Ro, see Figure 5.5, and $(1, 0, 0)$, see Figure 5.6); these are used to calibrate the temperature (and therefore mean sound speed) of the system. The variation

of their frequencies between experimental runs at different Ro is attributable to temperature variations (see Mautino's forthcoming Master's Thesis). Other $m = 0$ peaks show more complicated structure. For instance, the $(0, 4, 0)$ and $(1, 1, 0)$ modes lie fairly close to each other in frequency, and may be coupling via flow perturbations from the meridional flow [95], see Figure 5.7. The peaks of the acoustic modes also vary with time (see Figure 5.8), presumably due to fluctuations in the flow, as well as the stochastic nature of their excitation.

Using ambient excitation, we performed a scan in Ro, keeping the outer at a rotation rate of 6 Hz and varying the inner sphere from 4 to 40 Hz in 2 Hz steps, for both co-rotation and counter-rotation. An example of the spectra obtained can be seen in Figure 5.9, with a zoomed in view of the same in Figure 5.10. In addition, looking at spectrograms we can follow the frequency splitting of a given mode as Ro is varied, with the trend in splittings helping to constrain the amount of splitting for cases where the data is noisier, see Figures 5.11 and 5.12. Frequency splittings extracted from this data have in turn been used in calculating the velocity inversions presented in the next section.

5.5 Inversions and Implications

The ultimate goal of these acoustic measurements is to be able to infer characteristics of the zonal (azimuthal) flow in liquid sodium experiments; as a step towards this, we have measured acoustic splittings in gas in the 60 cm experiment. Acoustic modes are readily identified in the 60 cm gas system, as are the splittings

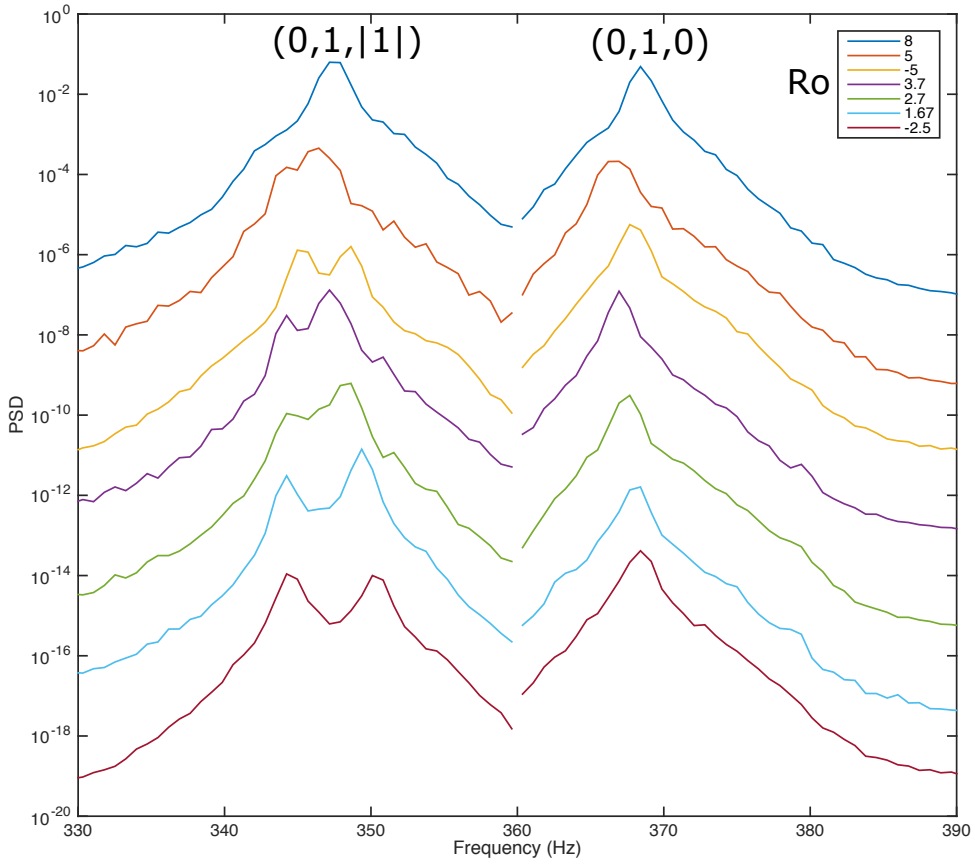

Figure 5.5: Peaks for modes $(0, 1, 1)$ and $(0, 1, 0)$ for a variety of Rossby numbers. Note the variation in the amount of splitting of $(0, 1, 1)$, seen on the left, which correlates well with the outer rotation rate. All the lines are plots of the logarithm of the power spectral density of either the difference (on the left) or sum (on the right) of the signals from Mics 1 and 2. Some of the variation in peak location between different runs may be due to temperature variations. The lines for different Rossby numbers are offset from each other for clarity.

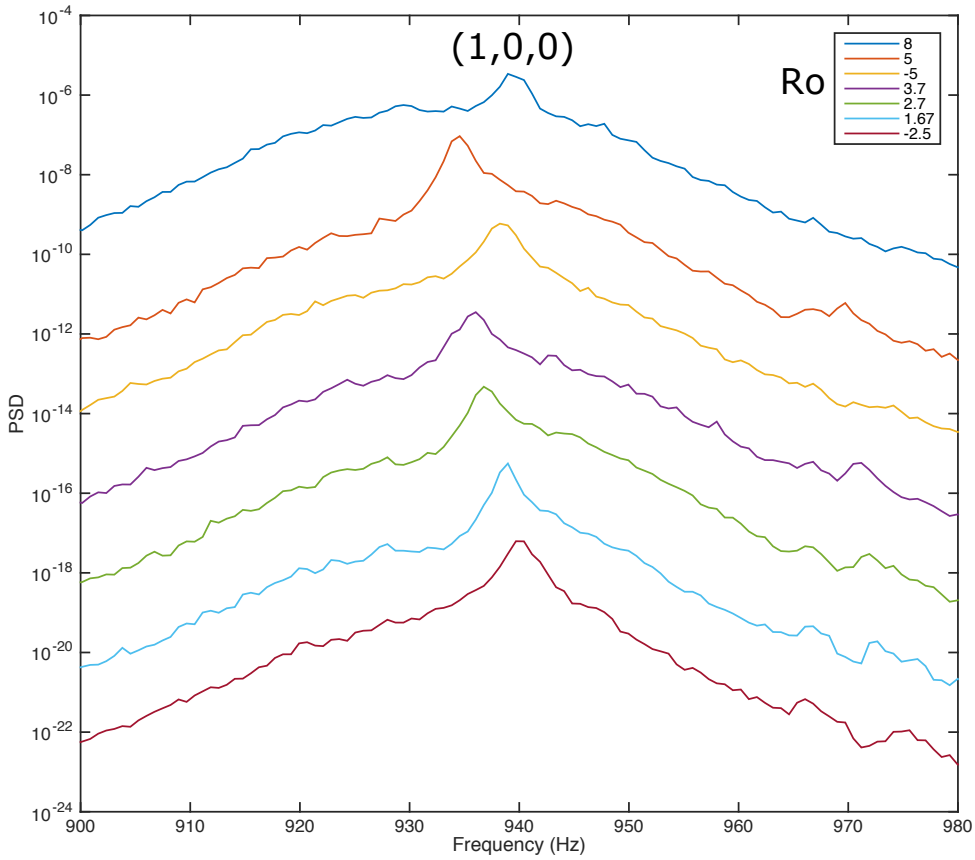

Figure 5.6: Peak for mode $(1, 0, 0)$ for a variety of Rossby numbers. This peak is more prominent and easily identifiable than some of the other $m = 0$ modes, though the width of its peak does show some variation with Rossby number. The variation in the location of the peak (in frequency) is probably due to variations in temperature between the different experimental runs. The lines for different Rossby numbers are offset from each other for clarity.

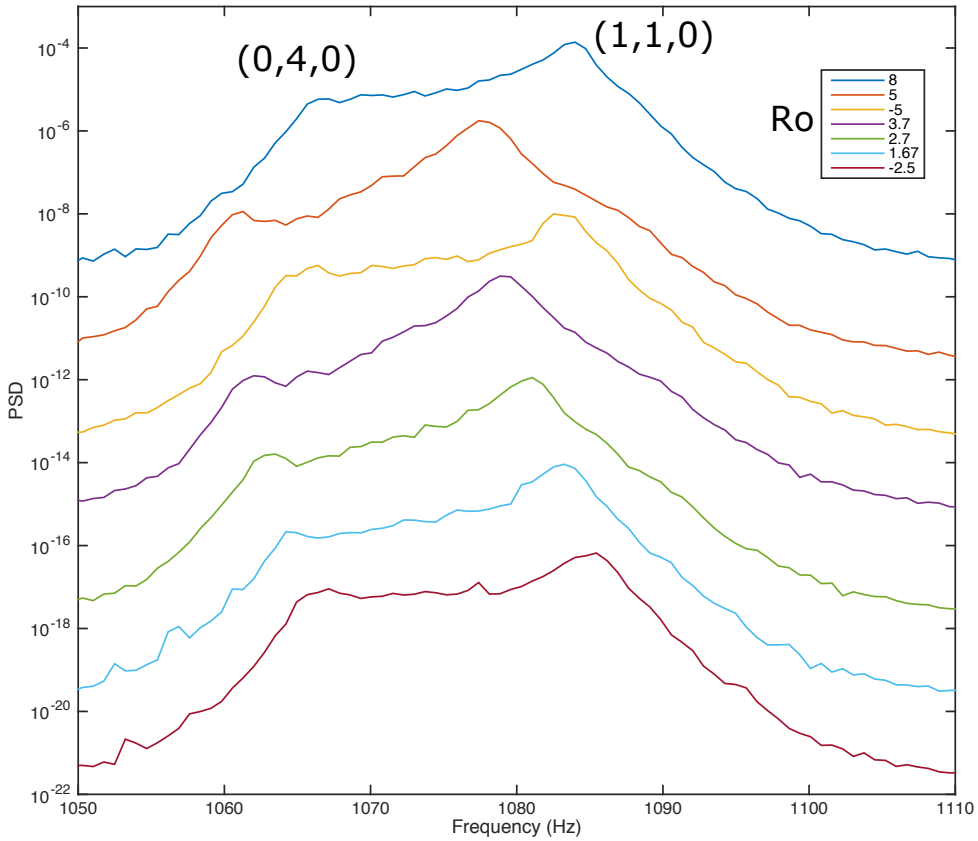

Figure 5.7: Peaks for modes $(0, 4, 0)$ and $(1, 1, 0)$ for a variety of Rossby numbers. These peaks are not as easily identifiable as some other $m = 0$ modes, like $(1, 0, 0)$. One possible explanation is meridional flows resulting in interaction between these two modes which are fairly close in frequency. The lines for different Rossby numbers are offset from each other for clarity.

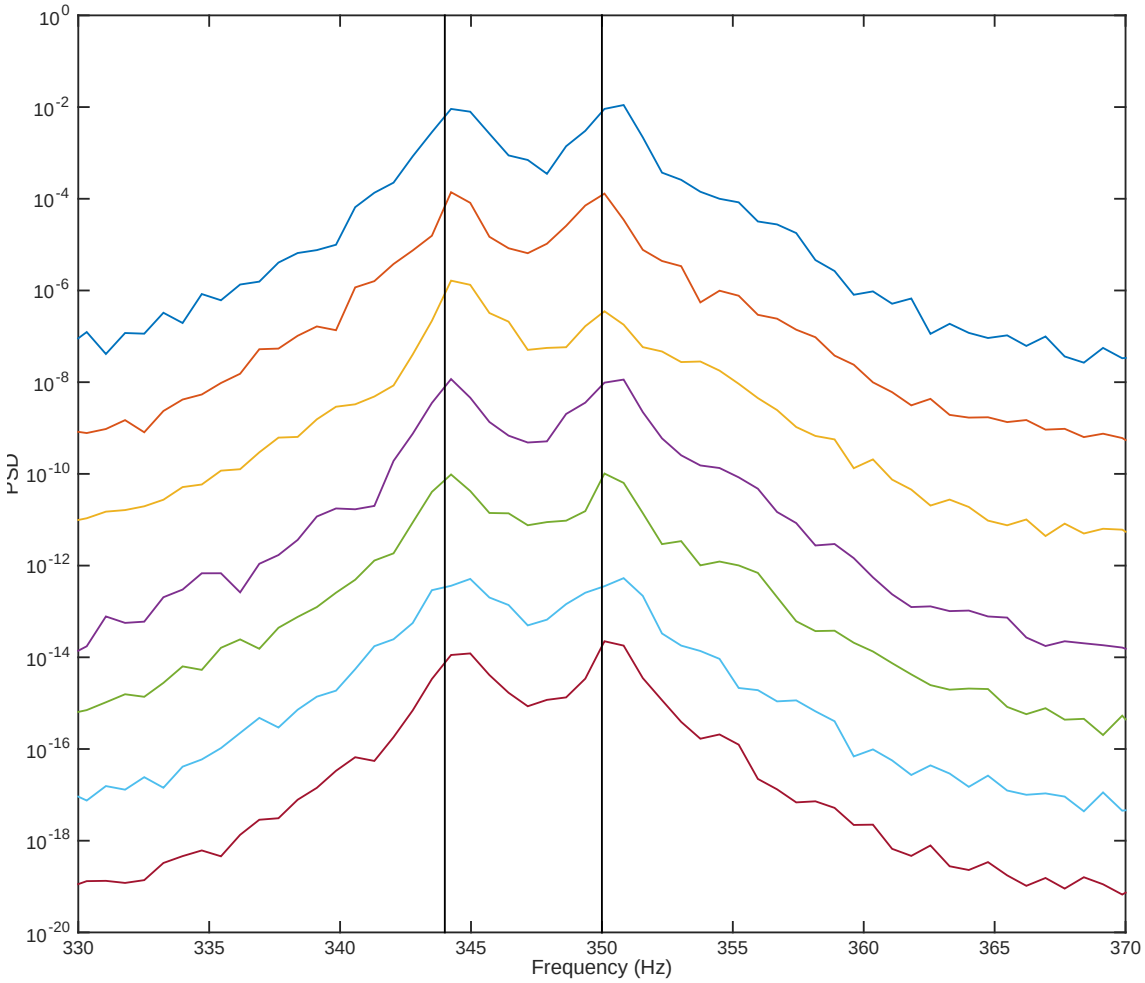

Figure 5.8: Variations in time of the splitting of modes $(0, 1, \pm 1)$ for the case of $Ro = -2.5$. Each line is a plot of the logarithm of the power spectral density of the difference between signals from Mic 1 and 2 (thus emphasizing modes with odd azimuthal wave number m); the lines are offset from each other for clarity. The spectra are calculated using consecutive time windows of an acoustic recording, with each window being about 5.2 s long. The location and prominence of the peaks varies over time, presumably due to fluctuations in the flow and the stochastic nature of the excitation of the mode. Vertical lines at 345 Hz and 350 Hz are shown to highlight the variation.

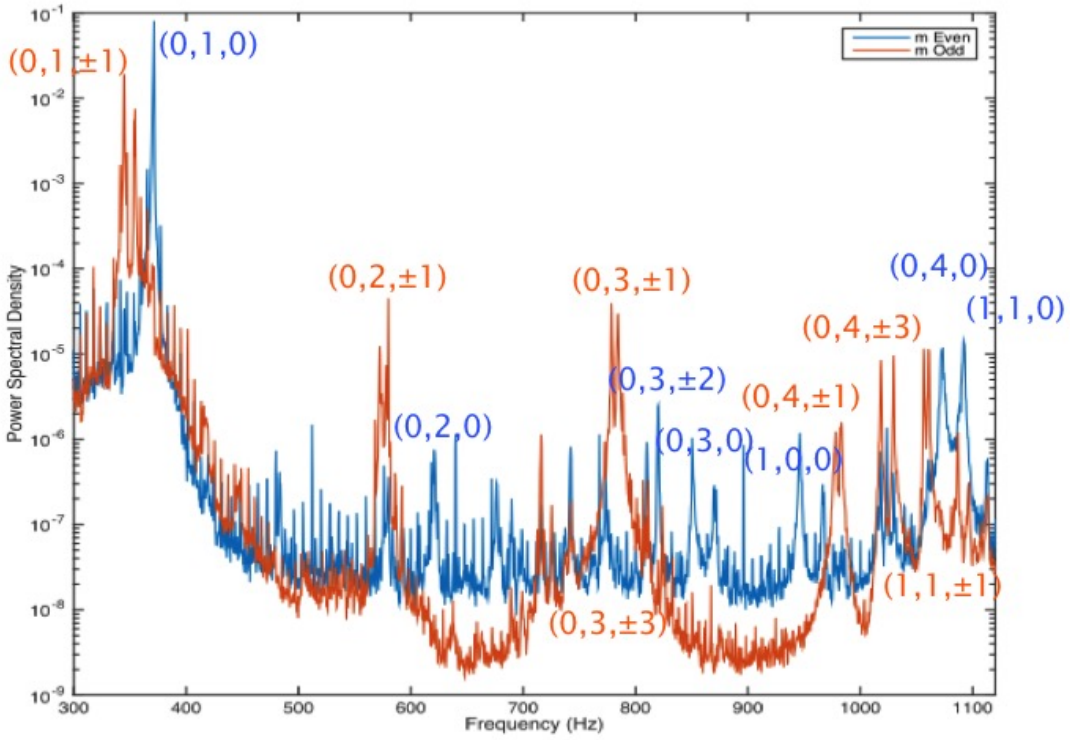

Figure 5.9: Power Spectral Density of the sum and difference of the signals from microphones 1 and 2, emphasizing even- and odd-m modes, respectively. Data taken with the outer sphere rotating at 6Hz, and with the inner counter-rotating at 24Hz, giving $Ro = -5$. No excitation chirp was used; note the many modes excited by the ambient noise. Also, note the lower noise floor for the difference of the signals, compared to their sum, which we believe is due to digital noise in the system that shows up on both microphone signals being canceled out by subtracting one from the other.

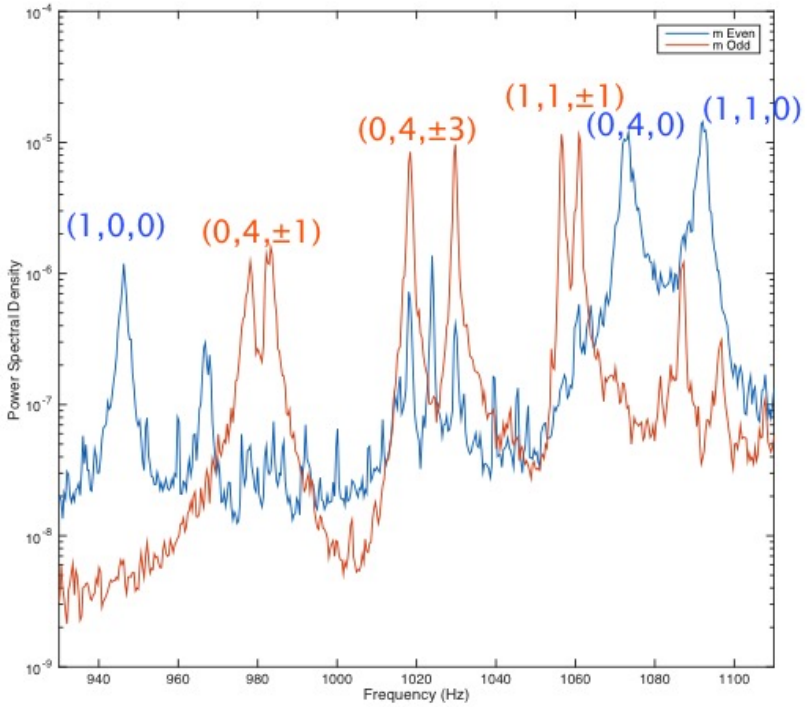

Figure 5.10: Power Spectral Density of the sum and difference of the signals from microphones 1 and 2, emphasizing even- and odd-m modes, respectively. Data taken with the outer sphere rotating at 6Hz, and with the inner counter-rotating at 24Hz (the same data as in Fig. 5.9). No chirp was used. Note the clear splittings of several of the modes, both even and odd, present in the frequency range shown.

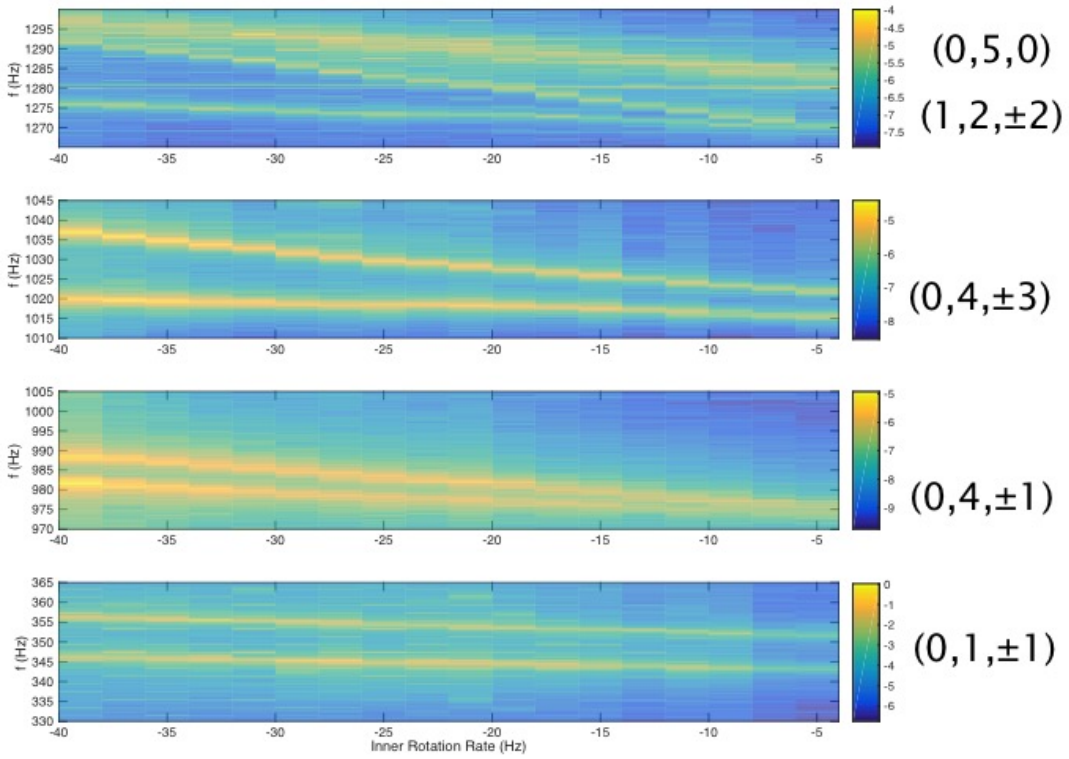

Figure 5.11: Spectrograms of the Power Spectral Density of acoustic signals for a variety of *Ro*, with the outer sphere rotating at 6Hz, and the inner sphere rotation rate varying from -4Hz to -40Hz. The sum or difference of the signals from microphones 1 and 2 are used to emphasize the acoustic modes in the displayed frequency range. Note the variations in the amount of splittings of the different modes as the inner rotation is varied.

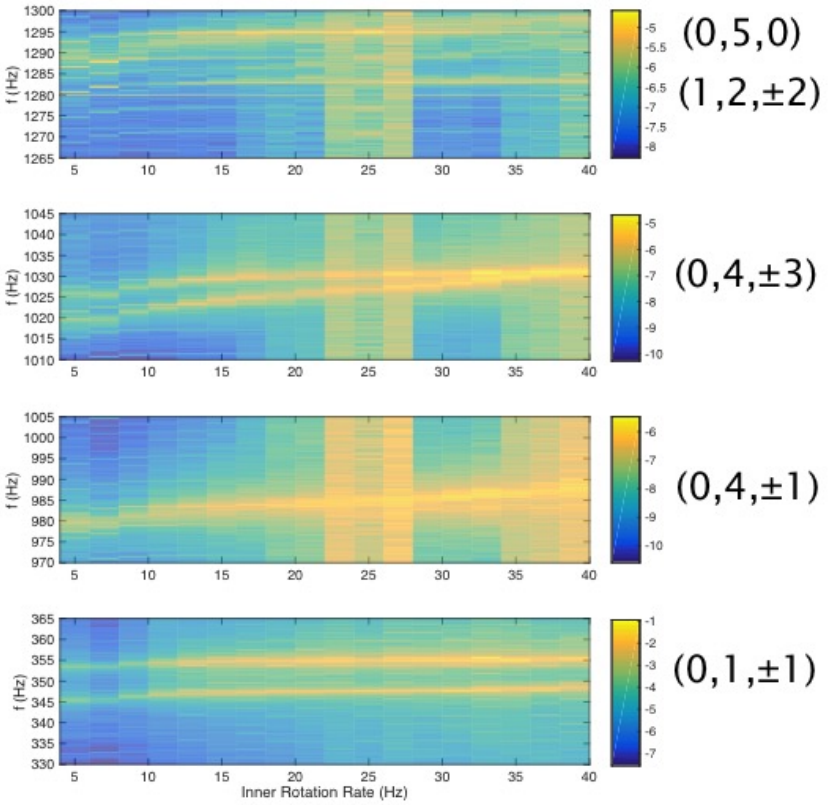

Figure 5.12: Spectrograms of the Power Spectral Density of acoustic signals for a variety of *Ro*, with the outer sphere rotating at 6Hz, and the inner sphere rotation rate varying from 4Hz to 40Hz. The sum or difference of the signals from microphones 1 and 2 are used to emphasize the acoustic modes in the displayed frequency range. Note the variations in the amount of splittings of the different modes as the inner rotation is varied.

Index	Mode
1	(0,1,1)
2	(0,2,1)
3	(0,3,1)
4	(0,3,2)
5	(0,4,1)
6	(0,4,3)
7	(1,1,1)
8	(0,5,1)
9	(0,6,1)
10	(1,3,2)
11	(1,4,1)
12	(2,2,1)
13	(1,5,1)
14	(2,3,1)
15	(2,3,2)

Table 5.3: Acoustic Modes used in Inversions, labeled by (n,l,m); the index label is the same as those used in Figures 5.14 and 5.16. Figure credit: Anthony Mautino.

induced in them by the flow. This is not the case for liquid sodium experiments, as we will discuss in section 5.6 below. For the 60 cm gas system, inversions have been computed using splitting measurements on 15 modes (see Table 5.3). Examples of inversions for the zonal flows are shown in Figures 5.13 and 5.15, while the fit of these inferred flows to the observed splittings are shown in Figures 5.14 and 5.16, respectively. The index of modes used in these inversions is given in Table 5.3.

The primary results from the inversions is a gradually strengthening jet from the inner sphere as the absolute rotation rate of the inner sphere is increased (as expected) with the bulk of the fluid rotating approximately with the outer sphere. Interestingly, the jet of fluid associated with the inner sphere appears to transport angular momentum from the inner sphere to the fluid above and below, resulting in a cylindrical region with larger zonal velocities (i.e. closer to that of the inner sphere) than the bulk of the fluid inside and outside it, which rotates at the outer

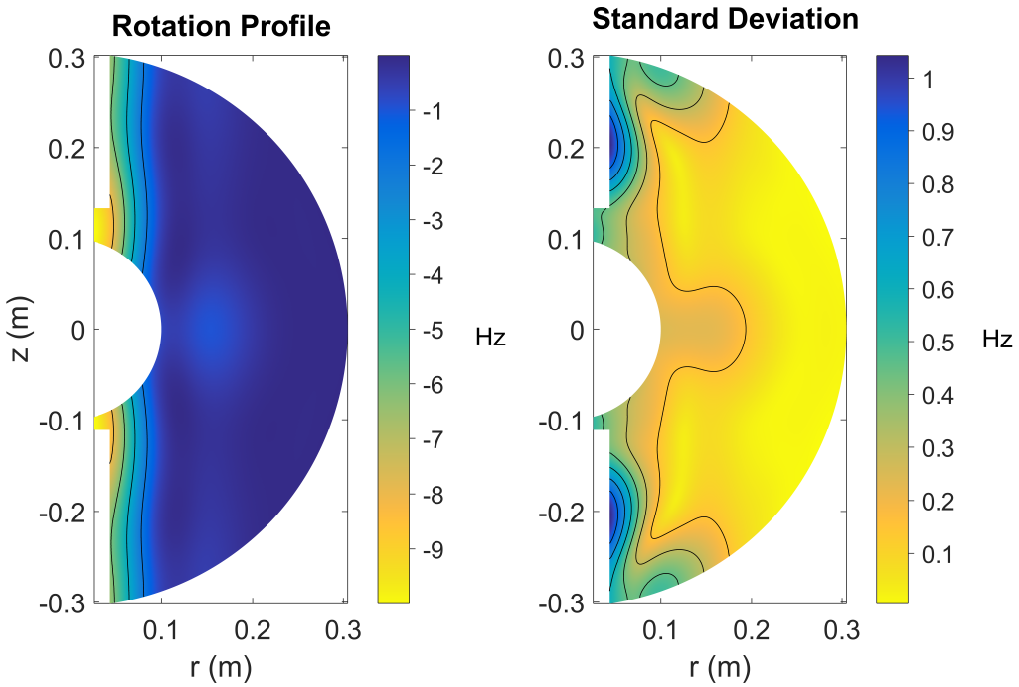

Figure 5.13: Inversion of Acoustic Mode Splittings for Zonal Flow, for the case f_i = -4 Hz, $f_o = 6$ Hz. On the left is the inferred rotation profile (i.e. rotation rate of the fluid as a function of (r, θ) in Hz in the rotating frame. Thus 0 Hz corresponds to the fluid rotating with the outer sphere. On the right is the standard deviation of the inferred velocity from inversion ensembles, giving a sense of the uncertainty in the inferred velocities. Figure credit: Anthony Mautino.

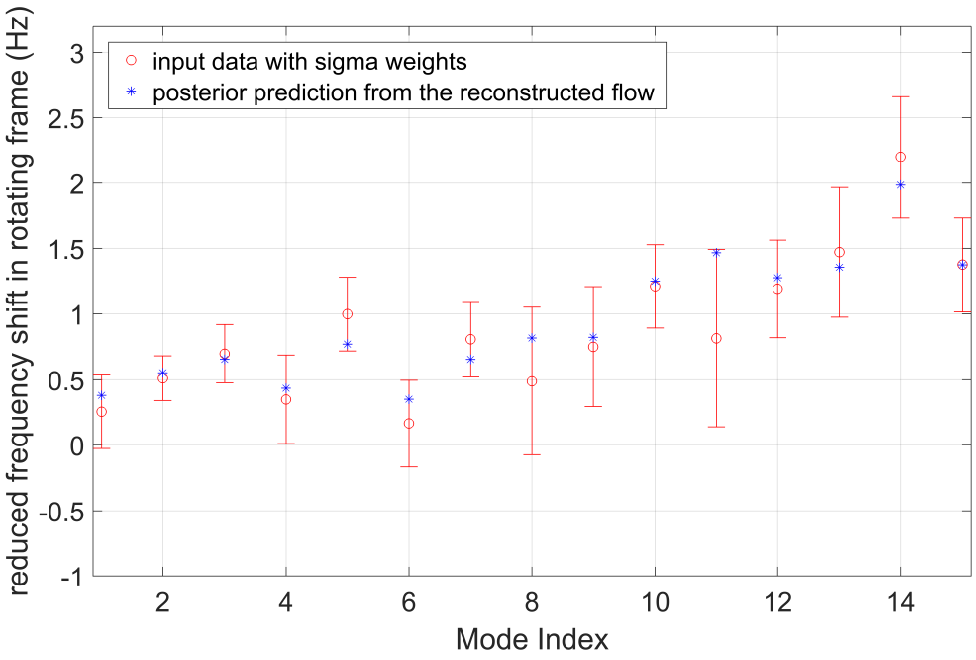

Figure 5.14: Fit of the Inversion shown in Figure 5.13 to the acoustic mode splittings used. The modes used are shown in Table 5.3. Figure credit: Anthony Mautino.

sphere rotation rate. While this is somewhat unusual for generic spherical Couette flows, it is plausible in the 60 cm experiment, given that the shaft above and below the inner sphere spins with the outer sphere, rather than with the inner.

5.6 Prospects for Acoustics in the 3 m Liquid Sodium Experiment

Since the initial impetus of the acoustic experiments in the 60 cm experiment was the implementation of this technique in liquid sodium experiments, we here detail some of the efforts to date to measure acoustic modes in the 3 m experiment. Unlike in the case of the 60 cm gas experiments, even the lowest lying modes are not obviously excited (by the turbulent flow or mechanical noise) for differential rotation in the 3 m liquid sodium experiment. In Figure 5.17, we plot the power spectral

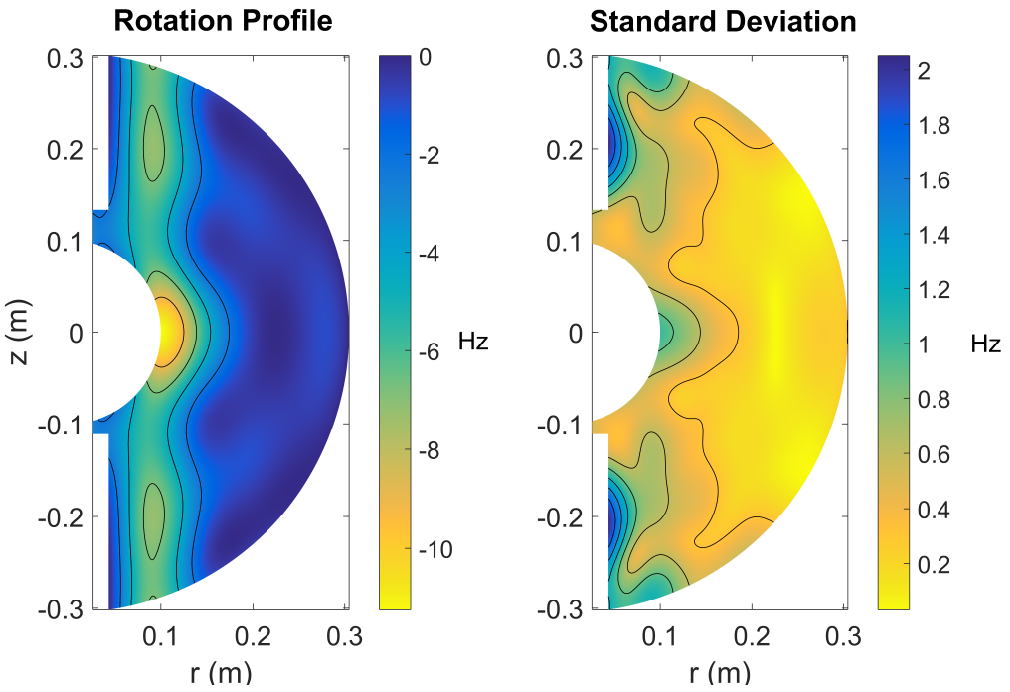

Figure 5.15: Inversion of Acoustic Mode Splittings for Zonal Flow, for the case f_i = -22 Hz, f_o = 6 Hz. On the left is the inferred rotation profile (i.e. rotation rate of the fluid as a function of (r, θ) in Hz in the rotating frame. Thus 0 Hz corresponds to the fluid rotating with the outer sphere. On the right is the standard deviation of the inferred velocity, giving a sense of the uncertainty in the inferred velocities. Figure credit: Anthony Mautino.

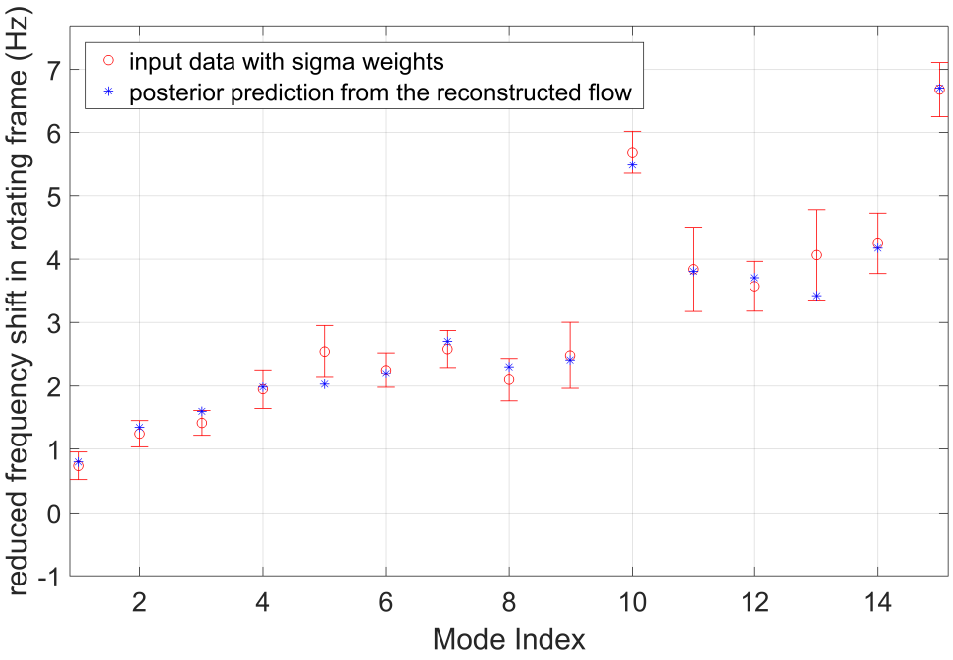

Figure 5.16: Fit of the Inversion shown in Figure 5.15 to the acoustic mode splittings used. The modes used are shown in Table 5.3. Figure credit: Anthony Mautino.

density of the signal from one of the Kistler pressure sensors in the 3 m system (see section 3.2.6). At low frequencies the signature of the broadband turbulence can be seen. The peaks around 400 Hz and 800 Hz are presumably due to belt noise: the outer sphere was rotating at 1 Hz, driven via a belt that meshes with a ring pulley mounted on the outer sphere, which has 400 teeth [32], and thus the belt meshes and unmeshes with the ring pulley teeth at a rate of 400 Hz. While there are lots of other structures present in this spectra, there are not any peaks that can be unambiguously identified as acoustic modes.

Perhaps the overlap between the mechanical noise or turbulent acoustic spectra of the system and the acoustic modes is not as favorable as in the 60 cm gas experiments. The 3 m system is five times larger than the 60 cm system (which would result in five times lower mode frequencies), but the speed of sound in liquid

sodium is about seven times higher than in air (or nitrogen gas), so the net effect is that the expected mode frequencies in 3 m are 1.4 times higher than those in the 60 cm gas system.

Given this, it appears we will need to actively excite acoustic modes in the system. While we have pressure probes that are sensitive in the relevant frequency range, obtaining a "speaker" that works in liquid sodium is more challenging. In order to provide some direct excitation to the system, we installed a piezo-electric shaker in one of the ports. The model used (Wilcoxon Research F7 Piezoelectric vibration generator) is designed for use in vibration testing structures, and can operate in the frequency range 500-20,000Hz and apply accelerations up to 1000g. Minh Doan designed and constructed a device to hold the shaker in one of the instrumentation ports on 3 m, with a rod connected to it that seated into a small depression in the bottom of the port, such that the rod was pressed against the bottom port face (see mechanical drawings in Appendix A). The idea behind the design was that when the shaker was driven, it would in turn vibrate the instrumentation port face, and couple to the liquid sodium on the other side of it.

While signs of the chirp were seen on the pressure probes, especially on the probes located in the same instrumentation port as the shaker, so far there has only been one acoustic mode tentatively identified, and no definitive splitting of it has been measured (see Figures 5.18 and 5.19). We have shown example spectra in Figure 5.18, with a zoomed in version in Figure 5.19. The peak seen in these figures has the frequency predicted by Mautino for the lowest lying mode in the 3 m experiment.

Turning to the properties of the modes themselves, the quality factors of the modes in the 3 m sodium experiment could be lower than those of the 60 cm gas experiment. In Table 5.4, we show the observed quality factors for some of the modes in the 60 cm gas experiment, for differential rotation with no chirp. Here we define the quality factor as the ratio of the frequency of the mode to the full width of its spectral peak at half maximum. For comparison, we also give an estimate of the expected quality factor based on just the viscosity of air, given by $Q = \omega/(\nu k^2)$, where ω is the mode frequency, ν is the kinematic viscosity of air, and k is the wavenumber of the mode, given by $k = (l + 1/2)/r$, where l is the mode's degree and r is the radius of the vessel. As can be seen, all of the acoustic modes have significantly lower quality factors than would be estimated based on viscosity alone. For liquid sodium, which has a kinematic viscosity about twenty times lower than that of air, the quality factor estimates based on viscosity would be even higher. Some other mechanism would be required to lower the quality factors.

One possibly relevant difference between the 60 cm gas system and the 3 m liquid sodium system is found in the values of the acoustic impedance mismatch between the vessel and the fluid. Using the product Z of the density and the speed of sound for the two systems, the mismatch between air and the titanium alloy of the 60 cm vessel is Z_{vessel}/Z_{fluid} =5.24e4, while for liquid sodium in stainless steel this is 10.5. The reflection coefficient (for the case of normal incidence), given by $R = (Z_{vessel} - Z_{fluid})/(Z_{vessel} + Z_{fluid})$, is 0.99996 for 60 cm and 0.826 for 3 m. Thus acoustic modes can be expected to more readily couple to the outer shell in 3 m, but this would only lower the quality factor of the modes if there is some other source

of damping (i.e. the shell modes are strongly damped). Since the 3 m system is surrounded by air, the shell will not readily lose much energy to the environment, though perhaps some energy is dissipated in the oil heating jacket.

There is also a bubble in the 3 m experiment (to allow for thermal expansion of the sodium), resulting in a free surface or (if the bubble is ingested into the flow) bubbles, which could also lead to acoustic modes coupling to other modes of the system (such as free surface waves), but again a further damping mechanism is required to extract energy from the acoustic modes. In addition, the DTS experiment in Grenoble has also not found any readily identifiable acoustic modes when the experiment is filled with liquid sodium (while they have been seen when the system is filled with air), and for this experiment there is no bubble present in the spherical cavity (though there is one in an expansion tank above the vessel).[1] Thus it seems unlikely that the presence of a free surface or bubbles within the fluid can provide the sole explanation for the difficulty in observing acoustic modes in liquid sodium.

If the difficulties with identifying acoustic modes in the 3 m system to date are due to low quality factors for the modes, whatever the cause, then perhaps more intense acoustic excitation could partially overcome this limitation. Since the shaker is attached to a rod that in turn is pressed up against a stainless steel plate 3/8" thick (the bottom of the instrumentation port, which faces the sodium), it is possible that much less power is coupling into the liquid sodium itself than would be the case for more direct excitation. Also, the acoustic modes might not be obviously split, but instead appear to broaden and perhaps change shape in response to the

[1] Personal communication, Henri-Claude Nataf 2016

(n,l,m)	Frequency	Full Width at Half Max	Observed Q	Viscous Q
(0,1,1)	344.8	1.1	313	8.80e5
(0,1,0)	371.3	0.35	1061	9.47e5
(0,2,1)	572.4	1	572	5.26e5
(0,2,0)	620.7	1.55	400	5.70e5
(0,3,1)	778.6	1.07	728	3.65e5
(0,3,2)	810.1	1.1	736	3.80e5
(0,3,0)	850.3	1.13	752	3.98e5
(1,0,0)	946.3	1.6	591	2.17e5
(0,4,1)	978.1	2	489	2.77e5
(0,4,3)	1018.5	1.1	926	2.89e5
(1,1,1)	1056.5	1	1057	2.70e6
(0,4,0)	1073.4	2.5	429	3.04e5
(1,1,0)	1092	2.4	455	2.79e6

Table 5.4: Quality Factors of Acoustic Modes in the 60 cm gas experiments. Comparison of observed quality factors for acoustic modes, using the frequency of the modes divided by their full width at half maximum, with an estimate based on viscous damping. Note that all the observed quality factors are much lower than the estimates, indicating that other factors besides viscosity are important for mode damping.

fluid flow. Perhaps more aggressive acoustic excitation of the system will yield more satisfactory results.

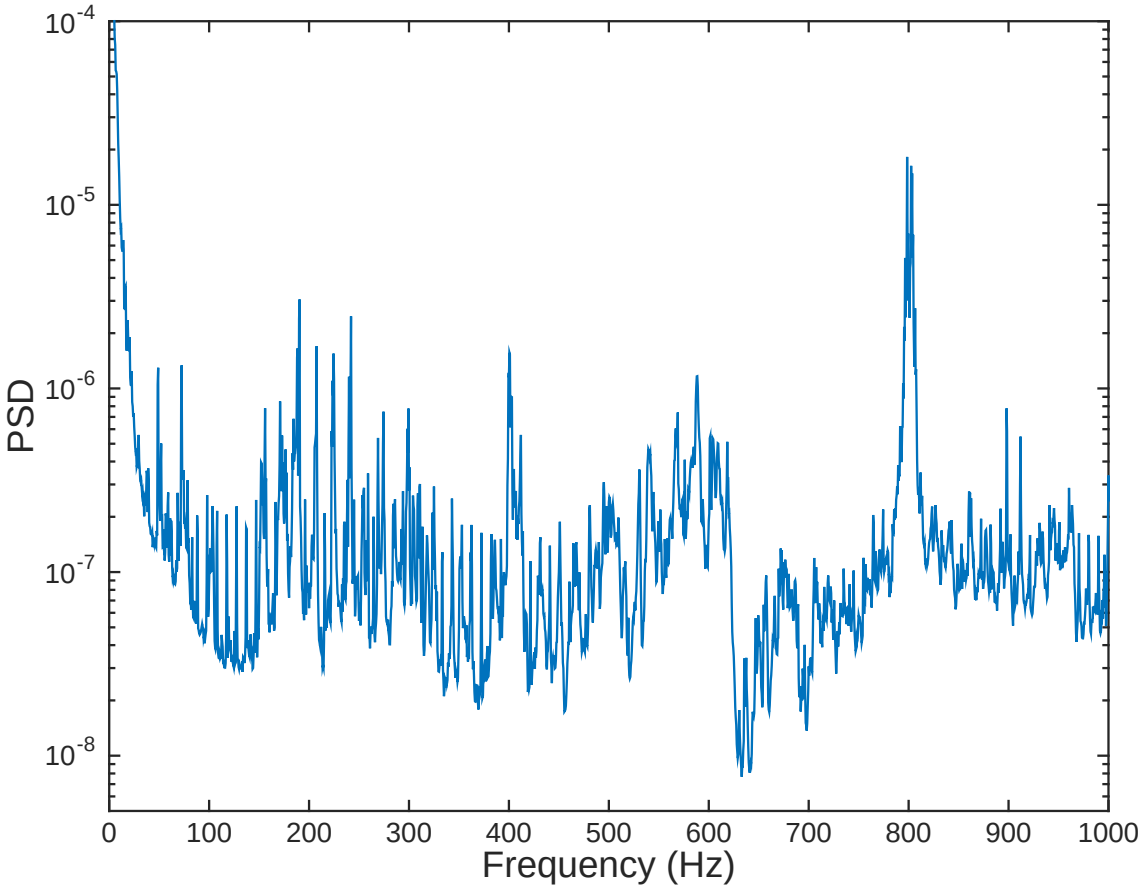

Figure 5.17: Power Spectral Density vs. Frequency of the Pressure Probe Signal in Port 1 of the 3 m Experiment: $f_i = 3.05$ Hz, $f_o = 1$ Hz. Note the large amount of power at low frequencies, a signature of the turbulent flow, and the two peaks near 400 Hz and 800 Hz, probably due to belt noise.

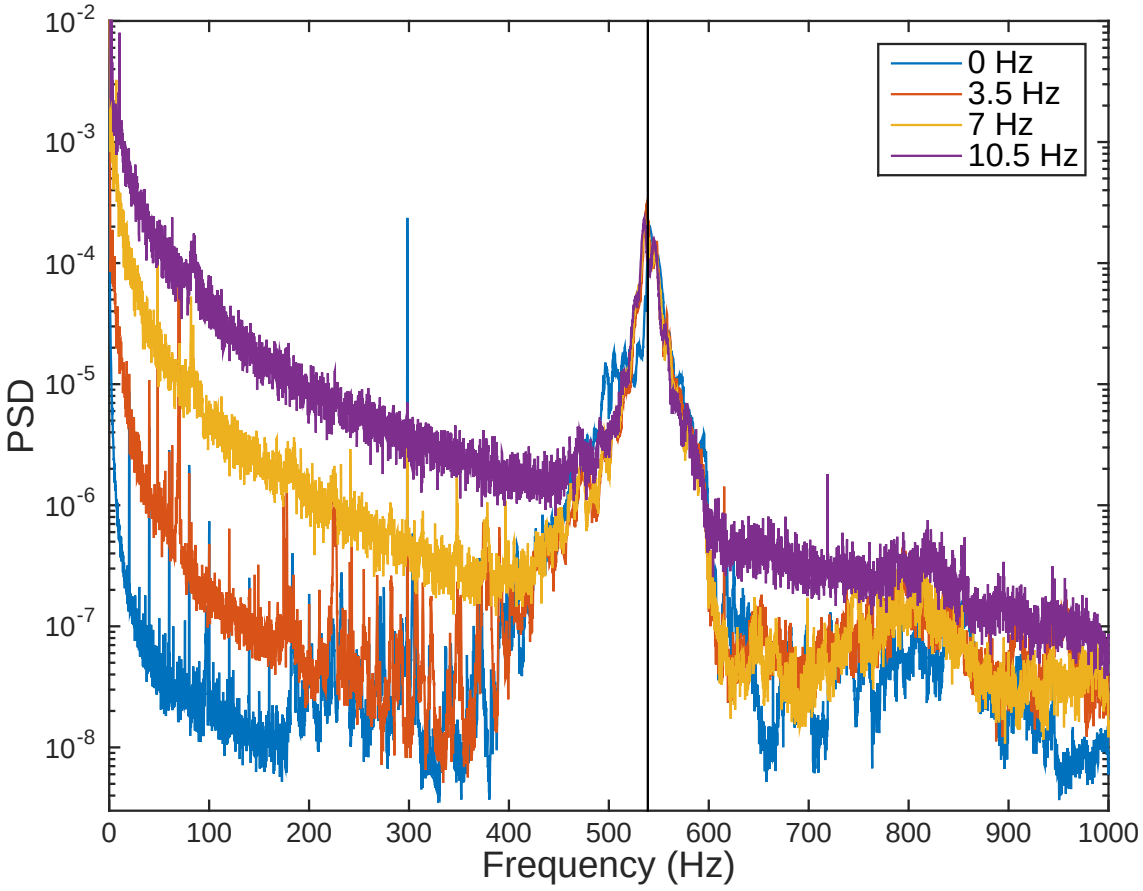

Figure 5.18: Power Spectral Density vs. Frequency of the Pressure Probe Signal in Port 1 of the 3 m Experiment: Inner-only rotation, with a chirp from 400 to 600 Hz, targeting mode $(0, 1, |1|)$, predicted by Mautino to have a frequency of 539 Hz (indicated by vertical black line); note that the $(0, 1, 0)$ is also predicted to lie in this range, with a frequency of 545 Hz.

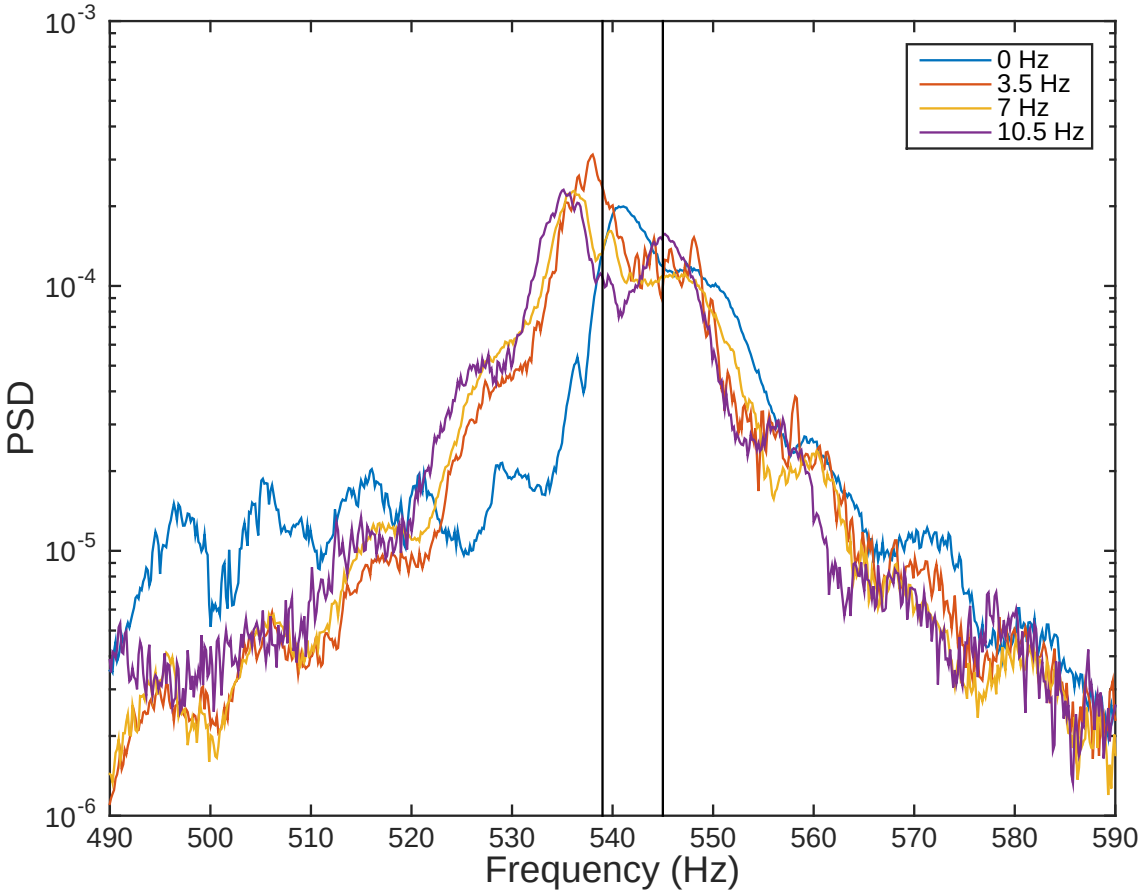

Figure 5.19: Power Spectral Density vs. Frequency of the Pressure Probe Signal in Port 1 of the 3 m Experiment: Inner-only rotation, with a chirp from 400 to 600 Hz, targeting mode $(0, 1, |1|)$, predicted by Mautino to have a frequency of 539 Hz (indicated by a vertical black line); note that the $(0, 1, 0)$ is also predicted to lie in this range, with a frequency of 545 Hz (also indicated by a vertical black line). Same as Figure 5.18 above, but showing a narrower range in frequency.

Chapter 6: Conclusions and Future Directions

In this final chapter, I provide a review of the work presented and offer some suggestions for future investigations.

6.1 Magnetic Results

In chapter 4, I presented an overview of the results of hydromagnetic experiments in the 3 m liquid sodium spherical Couette experiment. In particular, the spectra of Gauss coefficients for a variety of Ro were presented, and used to characterize the different states previously identified in [90]. We applied both dipolar and quadrupolar fields, and ran experiments with the outer at its maximum design speed. We corroborated previous results, and a new behavior was seen in the previously labeled Quiet state, with a broad spectral feature around $2.8f_o$, most prominent in the $m = 1$ Gauss coefficients. Spectral features of other states were also discussed in more detail. We also commented on the velocity inferences that can be made with this magnetic data, noting the possible velocity field patterns responsible for the primary observed induced magnetic field. These velocity inferences are helpful but also have major limitations, motivating the investigation of acoustic modes as a possible route to further flow field metrology.

6.2 Acoustic Results

In chapter 5, I presented the results of acoustic studies in gas with the 60 cm experiment. Acoustic modes of the container are readily identified, with discrimination between modes of similar frequency helped by considerations of spatial symmetry and simultaneous measurement using two microphones in different locations. We obtained excellent agreement between experimental and theoretical frequencies for stationary gas and uniformly rotating gas, as well as performing measurements with a turbulent flow. Many modes are excited by the turbulent flow and/or the mechanical noise of the experiment, obviating the need for direct acoustic excitation using speakers (though this was also done). Using splitting measurements for 15 modes, along with sensitivity kernels for the modes derived from a model of the 60 cm experiment, Anthony Mautino and Ved Lekic inverted this acoustic information for the zonal flow of the fluid $\Omega(r, \theta)$. The results of these inversions are plausible, and imply that further experiments in air would be able to further refine the flow patterns; if acoustic modes can be identified in liquid sodium experiments, such techniques should also allow velocity patterns of hydromagnetic experiments to be inferred.

6.3 Future Directions

One obvious area for further work is in attempting to excite and observe acoustic modes in the 3 m liquid sodium experiment. Of course, since this has

not been demonstrated, here we can only speculate on further investigations that might be fruitful. While there are not any obviously excited ambient modes in the 3 m system, more powerful acoustic excitation of the system may yield results. In particular, so far both excitation methods used (that is, tapping the outside of the experiment with a hammer, and exciting the piezoelectric shaker with a chirp) have put acoustic power into the sodium by first coupling to the outer spherical shell. Directly exciting the sodium, by for instance actuating a surface in contact with the sodium or perhaps using localized electric and magnetic fields to force oscillations in the sodium, has the potential to excite acoustic modes. This involves significantly more development work, and the actuation method perhaps would be better tested in a smaller set-up before attempting to implement it in the 3 m experiment. In particular, such a system would require the construction of a custom instrumentation port, along with the installation of any necessary supporting equipment on the lid.

If acoustic modes can be excited with such a set-up, a next step would be to consider using accelerometers to measure the modes. While initial studies would make use solely of the pressure probes already installed in the instrumentation ports, an advantage of the accelerometers is that, since they are mounted on the exterior of the outer shell, there is much more freedom in their locations, as opposed to the pressure probes which can only be installed in the instrumentation ports. By careful selection of their locations, the accelerometers could allow fine discrimination between various modes by using the spatial structure of the modes (as I achieved for the case of even and odd m and $l-m$ modes in the 60 cm acoustic experiments described in chapter 5). The accelerometers also have their own challenges, since

they will also be sensitive to modes of the shell of the experiment. The modes of the shell, and any coupling of them to the modes of the cavity, will therefore have to be explicitly modeled when making flow inferences from accelerometer measurements. Accelerometers have been tested with air in the DTS experiment at the Université Grenoble-Alpes, in Grenoble, France, and while they were not as sensitive as internally mounted microphones (unsurprisingly), they are capable of detecting acoustic modes. [1]

Assuming acoustic modes can be identified, with a robust method of exciting them and sufficient measurements (pressure probes and perhaps accelerometers) to distinguish between close-lying modes, inversions for the zonal flows could be performed. While meridional flows are expected to be significantly weaker than the zonal flows in the 3 m experiment, and thus a similarly weaker effect on the acoustic modes, it is possible that information regarding the meridional flows could also be extracted. This will require taking into account the coupling between different modes mediated by the meridional flows. There are plans to add baffles to the inner sphere of the 3 m experiment in order to enhance the coupling between the inner sphere and the fluid and drive more vigorous meridional flows. This is motivated by theoretical results that indicate such a modification may improve the chances of dynamo action [65]. If dynamo action is achieved in the 3 m experiment, acoustic mode velocimetry could be particularly useful in characterizing the flow field and possible dynamo mechanism, since magnetic measurements would be more challenging to interpret than in the case of fields only being induced by a weak applied field. Even in the

[1] Personal communication, Henri-Claude Nataf 2016.

absence of dynamo action, hydromagnetic flows with strong applied fields are also of interest, and would also benefit from velocity diagnostics independent of magnetic fields.

This proposed integration of acoustic and magnetic data to further understand strong field hydromagnetic flow, including any dynamo processes that may be present, can be seen more broadly as a move toward integrating a variety of measurements, including torque, pressure, and magnetic field measurements, to build up a more detailed picture of the fluid flow. Another complementary avenue is that of data assimilation, by which estimates of model parameters for the system could be refined using time series data from the 3 m system and techniques developed in the context of weather prediction. In particular, the goal for such models would be to converge on the internal state of the 3 m system (its flow field and internal magnetic field) from time series measurements of the external magnetic field, with the hope that this could inform efforts to do something similar for Earth's core. While data assimilation techniques are commonly used in meteorology, they have only recently been applied to the geodynamo [96, 97]. While both the Earth's atmosphere and the Earth's core are complicated systems obeying nonlinear equations of motion, the timescales or changes that we can measure are very different. Weather systems develop and dissipate on a timescale of weeks, while the geomagnetic field only slowly changes over the course of years. More dramatic changes like field reversals take hundreds or thousands of years to complete, and are separated by hundreds of thousands of years. Since the relevant timescales of the 3 m experiment are much shorter than those of the Earth, data assimilation used with the 3 m experiment

could be a step towards turning geomagnetic studies into a predictive science. By providing information about the flow field present in the 3 m experiment that is not mediated by magnetic field measurements, acoustic velocimetry could make such an approach in 3 m more robust, providing another way of evaluating the effectiveness of the models in estimating the internal state of the system. Lessons learned with 3 m could in turn inform work on estimating the state of Earth's core.

Chapter A: Mechanical Drawings

Here we include technical drawings by Minh Doan of the shaker holder which he designed and built, used in some of the acoustic studies detailed in chapter 5.

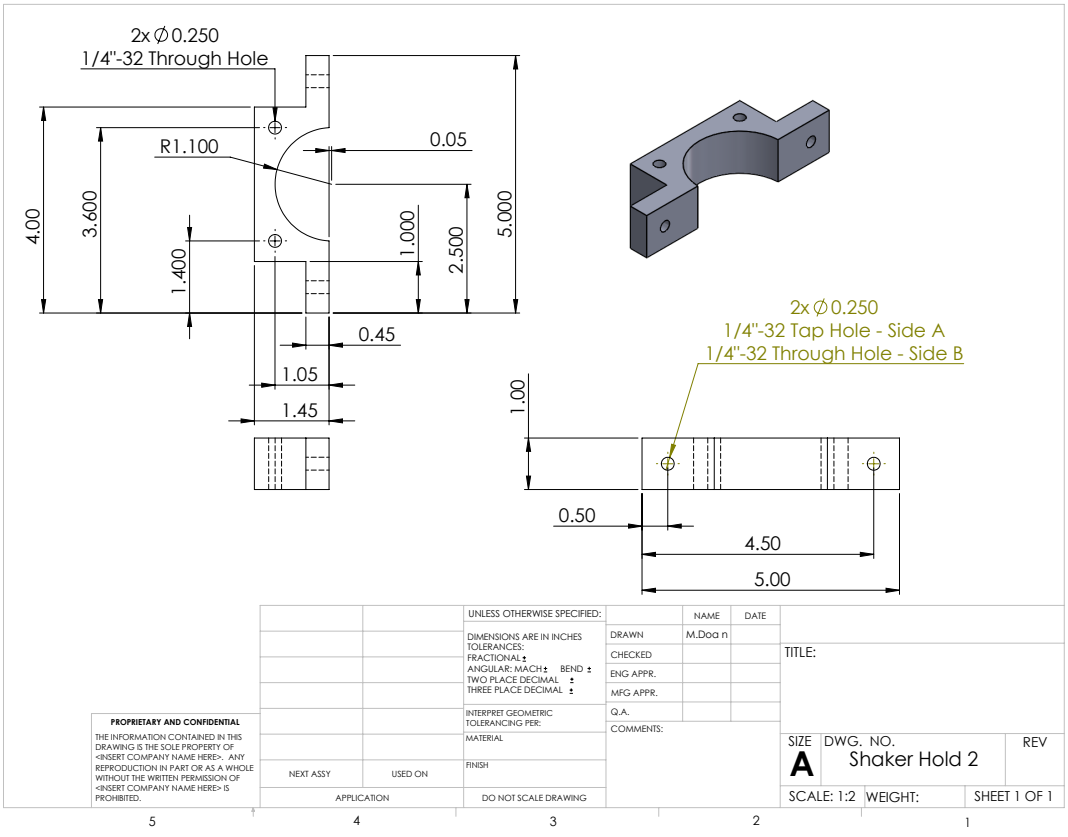
2x ∅0.250
1/4"-32 Through Hole
R1.100
0.05
4.00
3.600
1.400
1.000
2.500
5.000
0.45
1.05
1.45
2x ∅0.250
1/4"-32 Tap Hole - Side A
1/4"-32 Through Hole - Side B
1.00
0.50
4.50
5.00
UNLESS OTHERWISE SPECIFIED:
DIMENSIONS ARE IN INCHES
TOLERANCES:
FRACTIONAL ±
ANGULAR: MACH ± BEND ±
TWO PLACE DECIMAL ±
THREE PLACE DECIMAL ±
INTERPRET GEOMETRIC TOLERANCING PER:
MATERIAL
FINISH
NEXT ASSY
USED ON
APPLICATION
DO NOT SCALE DRAWING
NAME
DATE
DRAWN
M.Doa n
CHECKED
ENG APPR.
MFG APPR.
Q.A.
COMMENTS:
TITLE:
PROPRIETARY AND CONFIDENTIAL
THE INFORMATION CONTAINED IN THIS DRAWING IS THE SOLE PROPERTY OF <INSERT COMPANY NAME HERE>. ANY REPRODUCTION IN PART OR AS A WHOLE WITHOUT THE WRITTEN PERMISSION OF <INSERT COMPANY NAME HERE> IS PROHIBITED.
SIZE
A
DWG. NO.
Shaker Hold 2
REV
SCALE: 1:2
WEIGHT:
SHEET 1 OF 1
5
4
3
2
1

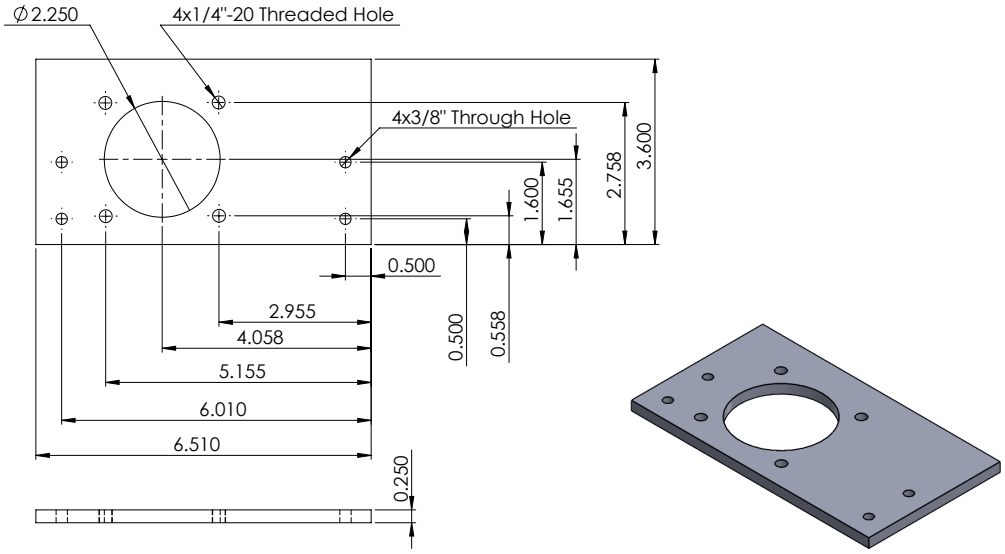

		UNLESS OTHERWISE SPECIFIED:		NAME	DATE
		DIMENSIONS ARE IN INCHES TOLERANCES: FRACTIONAL ± ANGULAR: MACH ± BEND ± TWO PLACE DECIMAL ± THREE PLACE DECIMAL ±	DRAWN	M.Doan	
			CHECKED		
			ENG APPR.		
			MFG APPR.		
		INTERPRET GEOMETRIC TOLERANCING PER:	Q.A.		
		MATERIAL	COMMENTS:		
NEXT ASSY	USED ON	FINISH			
APPLICATION		DO NOT SCALE DRAWING			

TITLE:

SIZE	DWG. NO.	REV
A	Shaker Mount Plate	
SCALE: 1:2	WEIGHT:	SHEET 1 OF 1

PROPRIETARY AND CONFIDENTIAL

THE INFORMATION CONTAINED IN THIS DRAWING IS THE SOLE PROPERTY OF <INSERT COMPANY NAME HERE>. ANY REPRODUCTION IN PART OR AS A WHOLE WITHOUT THE WRITTEN PERMISSION OF <INSERT COMPANY NAME HERE> IS PROHIBITED.

5 4 3 2 1

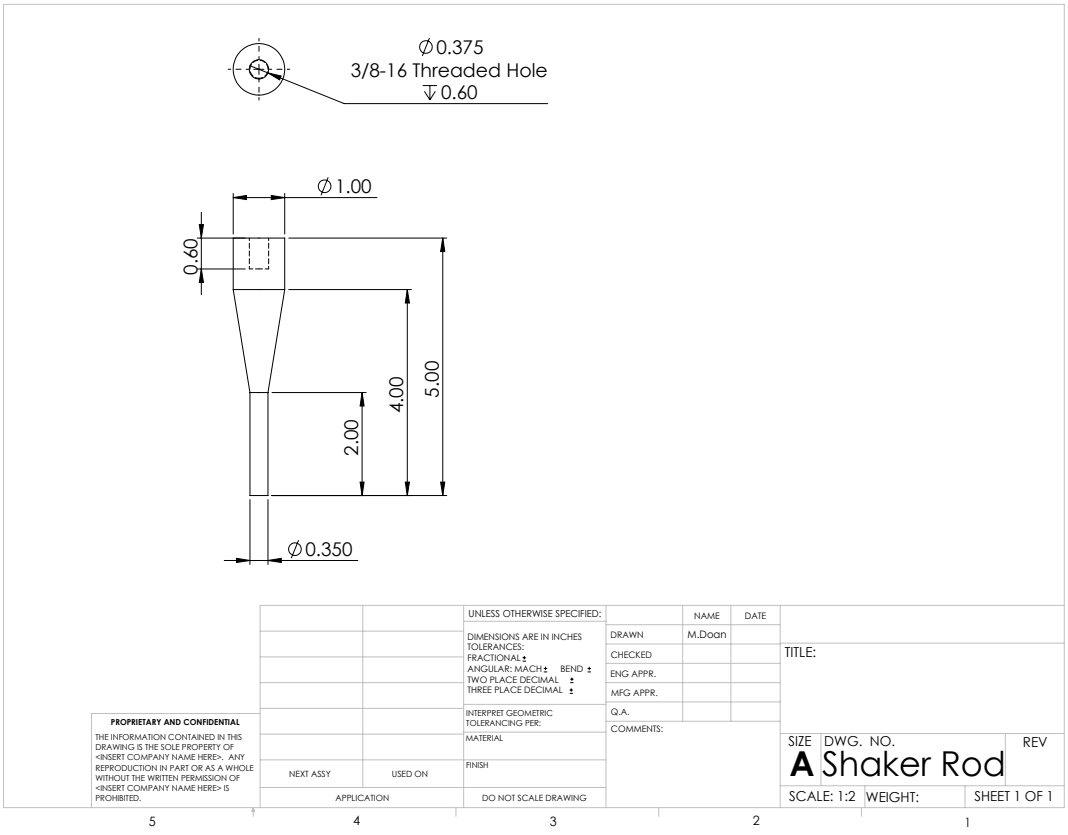

		UNLESS OTHERWISE SPECIFIED:		NAME	DATE
		DIMENSIONS ARE IN INCHES TOLERANCES: FRACTIONAL ± ANGULAR: MACH ± BEND ± TWO PLACE DECIMAL ± THREE PLACE DECIMAL ±	DRAWN	M.Doan	
			CHECKED		
			ENG APPR.		
			MFG APPR.		
		INTERPRET GEOMETRIC TOLERANCING PER:	Q.A.		
		MATERIAL	COMMENTS:		
NEXT ASSY	USED ON	FINISH			
APPLICATION		DO NOT SCALE DRAWING			

PROPRIETARY AND CONFIDENTIAL

THE INFORMATION CONTAINED IN THIS DRAWING IS THE SOLE PROPERTY OF <INSERT COMPANY NAME HERE>. ANY REPRODUCTION IN PART OR AS A WHOLE WITHOUT THE WRITTEN PERMISSION OF <INSERT COMPANY NAME HERE> IS PROHIBITED.

TITLE:

SIZE	DWG. NO.	REV
A	Shaker Rod	
SCALE: 1:2	WEIGHT:	SHEET 1 OF 1

5 4 3 2 1

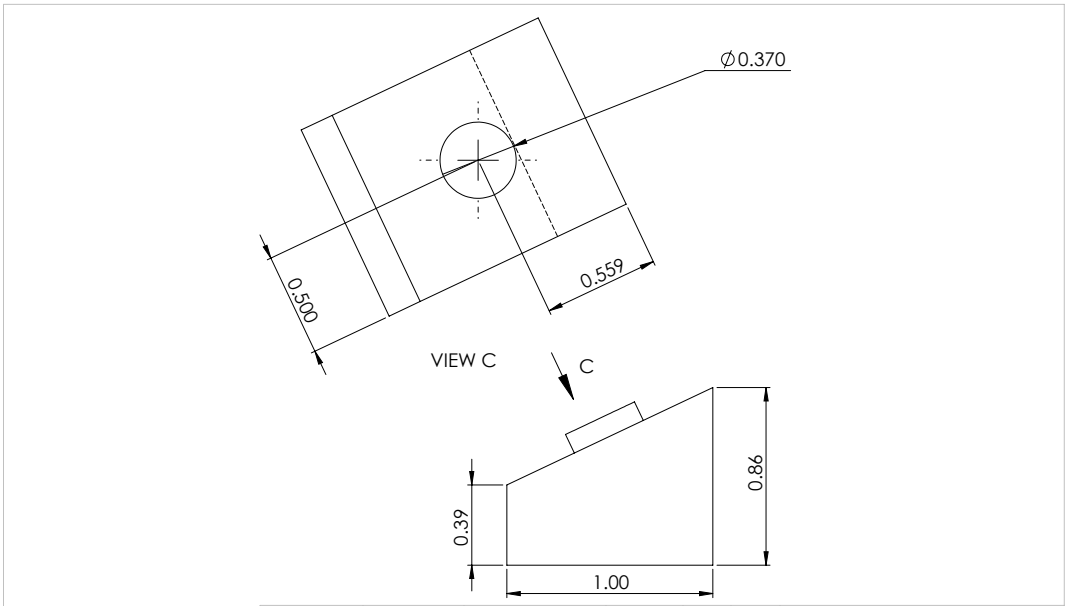

		UNLESS OTHERWISE SPECIFIED:		NAME	DATE	
		DIMENSIONS ARE IN INCHES TOLERANCES: FRACTIONAL ± ANGULAR: MACH ± BEND ± TWO PLACE DECIMAL ± THREE PLACE DECIMAL ±	DRAWN	M.Doan		TITLE:
			CHECKED			
			ENG APPR.			
			MFG APPR.			
		INTERPRET GEOMETRIC TOLERANCING PER:	Q.A.			
		MATERIAL	COMMENTS:			SIZE A / DWG. NO. Surface Contact / REV
NEXT ASSY	USED ON	FINISH				
APPLICATION		DO NOT SCALE DRAWING				SCALE: 2:1 / WEIGHT: / SHEET 2 OF 2

PROPRIETARY AND CONFIDENTIAL

THE INFORMATION CONTAINED IN THIS DRAWING IS THE SOLE PROPERTY OF <INSERT COMPANY NAME HERE>. ANY REPRODUCTION IN PART OR AS A WHOLE WITHOUT THE WRITTEN PERMISSION OF <INSERT COMPANY NAME HERE> IS PROHIBITED.

5 4 3 2 1

Bibliography

[1] J Larmor. How could a rotating body such as the sun become a magnet? *Rep Brit Assoc Adv Sci A*, 87:159–160, 1919.

[2] G Rüdiger and R Hollerbach. *The Magnetic Universe*. Wiley-VCH, Weinheim, 2004.

[3] MG Kivelson, KK Khurana, CT Russel, RJ Walker, J Warnecke, FJ Coroniti, C Polanskey, DJ Southwood, and G Schubert. Discovery of ganymede's magnetic field by the galileo spacecraft. *Nature*, 384:537–541, 1996.

[4] I Garrick-Bethel, B Weiss, D Shuster, and J Buz. Early lunar magnetism. *Science*, 323:356–359, 2009.

[5] MH Acuña, JEP Connerney, NF Ness, RP Lin, D Mitchell, CW Carlson, J McFadden, KA Anderson, H Rème, C Mazelle, D Vignes, P Wasilewski, and P Cloutier. Global distribution of crustal magnetization discovered by the mars global surveyor mag/er experiment. *Science*, 284:790–793, 1999.

[6] P Olson. Experimental dynamos and the dynamics of planetary cores. *Annu Rev Earth Pl Sc*, 41:153–81, 2013.

[7] G Schubert, K Zhang, MG Kivelson, and JD Anderson. The magnetic field and internal structure of ganymede. *Science*, 384:544–545, 1996.

[8] SI Vainshtein and YaB Zeldovich. Review of topical problems: Origin of magnetic fields in astrophysics (turbulent "dynamo" mechanisms). *Soviet Physics Uspekhi*, 15:159–172, 1972.

[9] A Gailitis, O Lielausis, S Dement'ev, E Platacis, A Cifersons, G Gerbeth, T Gundrum, F Stefani, M Christen, H Hänel, and G Will. Detection of a flow induced magnetic field eigenmode in the riga dynamo facility. *Phys Rev Lett*, 84(19):4365–4368, 2000.

[10] A Gailitis, O Lielausis, E Platacis, S Dement'ev, A Cifersons, G Gerbeth, T Gundrum, F Stefani, M Christen, and G Will. Magnetic field saturation in the riga dynamo experiment. *Phys Rev Lett*, 86(14):3024–3027, 2001.

[11] A Gailitis, G Gerbeth, T Gundrum, O Lielausis, E Platacis, and F Stefani. History and results of the riga dynamo experiments. *C R Phys*, 9:721–728, 2008.

[12] R Stieglitz and U Müller. Experimental demonstration of a homogeneous two-scale dynamo. *Phys Fluids*, 13:561–564, 2001.

[13] R Monchaux, M Berhanu, M Bourgoin, M Moulin, Ph Odier, J-F Pinton, R Volk, S Fauve, N Mordant, F Pétrélis, A Chiffaudel, F Daviaud, B Dubrulle, C Gasquet, L Marié, and F Ravelet. Generation of a magnetic field by dynamo action in a turbulent flow of liquid sodium. *Phys Rev Lett*, 98(4):044502–4, 2007.

[14] M Berhanu, R Monchaux, S Fauve, N Mordant, F Pétrélis, A Chiffaudel, F Daviaud, B Dubrulle, L Marié, F Ravelet, M Bourgoin, Ph Odier, J-F Pinton, and R Volk. Magnetic field reversals in an experimental turbulent dynamo. *EPL*, 77(5), 2007.

[15] GA Glatzmaier and PH Roberts. A three-dimensional self-consistent computer simulation of a geomagnetic field reversal. *Nature*, 377:203–209, 1995.

[16] F Takahashi, M Matsushima, and Y Honkura. Simulations of a quasi-taylor state geomagnetic field including polarity reversals on the earth simulator. *Science*, 309:459–461, 2005.

[17] CF Gauss. Allgemeine theorie des erdmagnetismus. In *Resultate aus den Beobachtungen magnetischen Vereins im Jahre 1838*, pages 1–57. 1839.

[18] LV Starukhina and MA Kreslavsky. Radiophysical properties of venusian highlands: Possible role of magnetic effects. *Lunar and Planetary Science Conference Proceedings*, 33(1559), 2002.

[19] F Nimmo. Why does venus lack a magnetic field? *Geology*, 30(11):987–990, 2002.

[20] C Milbury, G Schubert, CA Raymond, SE Smrekar, and B Langlais. The history of mars' dynamo as revealed by modeling magnetic anomalies near tyrrhenus mons and syrtis major. *J Geophys Res*, 117:E10007, 2012.

[21] JA Eddy. Historical and arboreal evidence for a changing sun. In JA Eddy, editor, *The New Solar Physics*. Westview Press, Coulder, Co., 1978.

[22] A Jackson, ART Jonkers, and MR Walker. Four centuries of geomagnetic secular variation from historical records. *Philos T Roy Soc A*, 358:957–990, 2000.

[23] RA Langel. The use of low altitude satellite data bases for modelling of core and crustal fields and the separation of external and internal fields. *Surv Geophys*, 14:31–87, 1993.

[24] BJ Sams, L Golub, and NO Weiss. X-ray observations of sunspot penumbral structure. *Astrophys J*, 399:313–317, 1992.

[25] SA Balbus and JF Hawley. A powerful local shear instability in weakly magnetized disks. i. linear analysis. *Astrophys J*, 376:214–222, 1991.

[26] SA Balbus and JF Hawley. Instability, turbulence, and enhanced transport in accretion disks. *Rev. Mod. Phys.*, 70:1–53, Jan 1998.

[27] E Bullard and H Gellman. Homogeneous dynamos and terrestrial magnetism. *Philos T R Soc S-A*, 247(928):213–278, 1954.

[28] J Christensen-Dalsgaard. Helioseismology. *Rev Mod Phys*, 74:1073–1129, 2002.

[29] B De Pontieu, R Erdélyi, and SP James. Solar chromospheric spicules from the leakage of photospheric oscillations and flows. *Nature*, 430:536–539, 2004.

[30] EA Spiegel and J-P Zahn. The solar tachocline. *Astron Astrophys*, 265:106–114, 1992.

[31] EN Parker. A solar dynamo surface wave at the interface between convection and nonuniform rotation. *Astrophys J*, 408:707–719, 1993.

[32] DS Zimmerman. *Turbulent Shear Flow in a Rapidly Rotating Spherical Annulus*. PhD thesis, University of Maryland, 2010.

[33] K Stewartson. On almost rigid rotations 2. *J Fluid Mech*, 26:131–144, 1966.

[34] R Hollerbach. Instabilities of the Stewartson layer part 1. the dependence on the sign of Ro. *J Fluid Mech*, 492:289–302, 2003.

[35] R Hide and CW Titman. Detached shear layers in a rotating fluid. *J Fluid Mech*, 29:39–60, 1967.

[36] WG Früh and PL Read. Experiments on a barotropic rotating shear layer. part 1. instability and steady vortices. *J Fluid Mech*, 383:143–173, 1999.

[37] FH Busse. Shear flow instabilities in rotating systems. *J Fluid Mech*, 33:577–589, 1968.

[38] R Hollerbach, B Futterer, T More, and C Egbers. Instabilities of the stewartson layer: Part 2. supercritical mode transitions. *Theor Comp Fluid Dyn*, 18:197–204, 2004.

[39] C Guervilly and P Cardin. Numerical simulations of dynamos generated in spherical couette flows. *Geophys Astro Fluid*, 104:221–248, 2010.

[40] J Wicht. Flow instabilities in the wide-gap spherical couette system. *J Fluid Mech*, 738:184–221, 2014.

[41] M Rieutord, SA Triana, DS Zimmerman, and DP Lathrop. Excitation of inertial modes in an experimental spherical couette flow. *Phys Rev E*, 86:026304, 2012.

[42] DR Sisan, N Mujica, WA Tillotson, YM Huang, W Dorland, AB Hassam, TM Antonsen, and DP Lathrop. Experimental observation and characterization of the magnetorotational instability. *Physical Review Letters*, 93(11):114502, 2004.

[43] W Shew and DP Lathrop. Liquid sodium model of geophysical core convection. *Phys Earth Planet In*, 153:136–149, 2005.

[44] DH Kelley, SA Triana, DS Zimmerman, B Brawn, DP Lathrop, and DH Martin. Driven inertial waves in spherical couette flow. *Chaos*, 16:1105, 2006.

[45] DH Kelley, SA Triana, DS Zimmerman, A Tilgner, and DP Lathrop. Inertial waves driven by differential rotation in a planetary geometry. *Geophys Astro Fluid*, 101(5-6):469–487, 2007.

[46] DH Kelley, SA Triana, DS Zimmerman, and DP Lathrop. Selection of inertial modes in spherical couette flow. *Phys Rev E*, 81:026311, 2010.

[47] DS Zimmerman, SA Triana, and DP Lathrop. Bi-stability in turbulent, rotating spherical couette flow. *Phys Fluids*, 23:065104, 2011.

[48] DR Sisan. *Hydromagnetic turbulent instability in liquid sodium experiments*. PhD thesis, University of Maryland, 2004.

[49] SA Triana, DS Zimmerman, and DP Lathrop. Precessional states in a laboratory model of the earth's core. *J Geophys Res*, 117, 2012.

[50] WVR Malkus. Precession of the earth as the cause of geomagnetism. *Science*, 160:259–264, 1968.

[51] X Wei, A Jackson, and R Hollerbach. Kinematic dynamo action in spherical couette flow. *Geophys Astro Fluid*, 106:681–700, 2012.

[52] SV Starchenko. Magnetohydrodynamic flow between insulating shells rotating in strong potential field. *Phys Fluids*, 10:2412–2420, 1998.

[53] E Dormy, P Cardin, and D Jault. Mhd flow in a slightly differentially rotating spherical shell, with conducting inner core, in a dipolar magnetic field. *Earth Planet Sc Lett*, 160:15–30, 1998.

[54] E Dormy, D Jault, and AM Soward. A super-rotating shear layer in magnetohydrodynamic spherical couette flow. *J Fluid Mech*, 452:263–291, 2002.

[55] R Hollerbach. Magnetohydrodynamic flows in spherical shells. In C. Egbers and G. Pfister, editors, *Physics of Rotating Fluids (Lecture Notes in Physics)*. Springer, Heidelberg, 1st edition, 2000.

[56] R Hollerbach and S Skinner. Instabilities of magnetically induced shear layers and jets. *Proc R Soc A*, 457:785–802, 2001.

[57] R Hollerbach, E Canet, and A Fournier. Spherical couette flow in a dipolar magnetic field. *Eur J Mech B-Fluid*, 26:729–737, 2007.

[58] R Hollerbach. Super- and counter-rotating jets and vortices in strongly magnetic spherical couette flow. In P Chossat, D Armbruster, and J Oprea, editors, *Dynamo and dynamics: a mathematical challenge*. Kluwer, Dordrecht, the Netherlands, 2001.

[59] X Wei and R Hollerbach. Instabilities of shercliff and stewartson layers in spherical couette flow. *Phys Rev E*, 78:026309, 2008.

[60] C Gissinger, H Ji, and J Goodman. Instabilities in magnetized spherical couette flow. *Phys Rev E*, 84:026308, 2011.

[61] A Figueroa, N Schaeffer, H-C Nataf, and D Schmitt. Modes and instabilities in magnetized spherical couette flow. *J Fluid Mech*, 716:445–469, 2013.

[62] PA Davidson and A Pothérat. A note on bödewadt-hartmann layers. *Eur J Mech B-Fluid*, 21:545–559, 2002.

[63] N Schaeffer and P Cardin. Quasi-geostrophic kinematic dynamos at low magnetic prandtl number. *Earth Planet Sc Lett*, 245:595–604, 2006.

[64] R Raynaud and E Dormy. Intermittency in spherical couette dynamos. *Phys Rev E*, 87:033011, 2013.

[65] K Finke and A Tilgner. Simulations of the kinematic dynamo onset of spherical couette flows with smooth and rough boundaries. *Phys Rev E*, 86:016310, 2012.

[66] G Rüdiger, LL Kitchatinov, and R Hollerbach. *Magnetic Processes in Astrophysics: Theory, Simulations, Experiments*. Wiley-VCH, Weinheim, 2013.

[67] M Nornberg, E Spence, R Kendrick, C Jacobson, and C Forest. Measurements of the magnetic field induced by a turbulent flow of liquid metal. *Phys Plasmas*, 13:055901, 2006.

[68] H-C Nataf, T Alboussière, D Brito, P Cardin, N Gagnière, D Jault, J-P Masson, and D Schmitt. Experimental study of super-rotation in a magnetostrophic spherical couette flow. *Geophys Astro Fluid*, 100:281–298, 2006.

[69] H-C Nataf, T Alboussière, D Brito, P Cardin, N Gagnière, D Jault, and D Schmitt. Rapidly rotating spherical couette flow in a dipolar magnetic field: An experimental study of the mean axisymmetric flow. *Phys Earth Planet In*, 170:60–72, 2008.

[70] Y Ponomarenko. Theory of the hydromagnetic generator. *J Appl Mech Tech Phy*, 14:775–778, 1973.

[71] GO Roberts. Dynamo action of fluid motions with two-dimensional periodicity. *Philos T R Soc S-A*, 271:411, 1972.

[72] M Nornberg, C Forest, and N Plihon. Soft-iron impellers in the madison sodium dynamo experiment, 2014a.

[73] ML Dudley and RW James. Time-dependent kinematic dynamos with stationary flows. *Proc R Soc Lon Ser-A*, 425:407, 1989.

[74] EJ Spence, MD Nornberg, CM Jacobson, RD Kendrick, and CB Forest. Observation of turbulence-induced large scale magnetic field. *Phys Rev Lett*, 96:055002, 2006.

[75] K Krause and KH Rädler. *Mean-field Magnetohydrodynamics and Dynamo Theory*. Pergamon Press, New York, 1980.

[76] M Steenbeck, IM Kirko, A Gailitis, AP Klyavinya, F Krause, IYa Laumanis, and OA Lielausis. Experimental discovery of the electromotive force along the external magnetic field induced by a flow of liquid metal (α-effect). *Sov Phys Dokl*, 13:443, 1968.

[77] TG Cowling. The stability of gaseous stars. *Mon Not R Astron Soc*, 94:768–782, 1934.

[78] EJ Spence, MD Nornberg, CM Jacobson, CA Parada, NZ Taylor, RD Kendrick, and CB Forest. Turbulent diamagnetism in flowing liquid sodium. *Phys Rev Lett*, 98:164503, 2007.

[79] EJ Kaplan, MM Clark, MD Nornberg, K Rahbarnia, AM Rasmus, NZ Taylor, CB Forest, and EJ Spence. Reducing global turbulent resistivity by eliminating large eddies in a spherical liquid-sodium experiment. *Phys Rev Lett*, 106:254502, 2011.

[80] MD Nornberg, NZ Taylor, CB Forest, K Rahbarnia, and E Kaplan. Optimization of magnetic amplification by flow constraints in turbulent liquid sodium. *Phys Plasmas*, 21:055903, 2014.

[81] P Cardin, D Brito, D Jault, H-C Nataf, and J-P Masson. Towards a rapidly rotating liquid sodium dynamo experiment. *Magnetohydrodynamics*, 38:177–189, 2002.

[82] D Schmitt, P Cardin, P La Rizza, and H-C Nataf. Magneto-coriolis waves in a spherical couette flow experiment. *Eur J Mech B-Fluid*, 37:10–22, 2013.

[83] SI Braginsky. Magnetic waves in the core of the earth. ii. *Geophys Astro Fluid*, 14:189–208, 1979.

[84] CC Finlay and A Jackson. Equatorially dominated magnetic field change at the surface of earth's core. *Science*, 300(5628):2084–2086, 2003.

[85] D Brito, T Alboussière, P Cardin, N Gagnière, D Jault, P La Rizza, J-P Masson, H-C Nataf, and D Schmitt. Zonal shear and super-rotation in a magnetized spherical couette-flow experiment. *Phys Rev E*, 83:066310, 2011.

[86] SV Starchenko. Magnetohydrodynamics of a viscous spherical shear layer rotating in a strong potential field. *J Exp Theor Phys*, 85:1125, 1997.

[87] UR Christensen and J Aubert. Scaling properties of convection-driven dynamos in rotating spherical shells and application to planetary magnetic fields. *Geophys J Int*, 166:97–114, 2006.

[88] S Cabanes, N Schaeffer, and H-C Nataf. Turbulence reduces magnetic diffusivity in a liquid sodium experiment. *Phys Rev Lett*, 113:184501, 2014.

[89] S Cabanes, N Schaeffer, and H-C Nataf. Magnetic induction and diffusion mechanisms in a liquid sodium spherical couette experiment. *Phys Rev E*, 90:043018, 2014.

[90] DS Zimmerman, SA Triana, H-C Nataf, and DP Lathrop. A turbulent, high magnetic reynolds number experimental model of earth's core. *J Geophys Res*, 119:4538–4557, 2014.

[91] DH Kelley. *Rotating, hydromagnetic laboratory experiment modelling planetary cores*. PhD thesis, University of Maryland, 2009.

[92] SA Triana, DS Zimmerman, H-C Nataf, A Thorette, V Lekic, and DP Lathrop. Helioseismology in a bottle: modal acoustic velocimetry. *New J Phys*, 16:113005, 2014.

[93] SA Triana. *Inertial waves in a laboratory model of the Earth's core*. PhD thesis, University of Maryland, 2010.

[94] W Shew. *Liquid Sodium Model of Earth's Outer Core*. PhD thesis, University of Maryland, 2004.

[95] EM Lavely and MH Ritzwoller. The effect of global-scale, steady-state convection and elastic-gravitational asphericities on helioseismic oscillations. *Phil Trans R Soc Lond A*, 339:431–496, 1992.

[96] A Fournier, G Hulot, D Jault, W Kuang, A Tangborn, N Gillet, E Canet, J Aubert, and F Lhuillier. An introduction to data assimilation and predictability in geomagnetism. *Space Sci Rev*, 155:247–291, 2010.

[97] A Tangborn and W Kuang. Geodynamo model and error parameter estimation using geomagnetic data assimilation. *Geophys J Int*, 200:664–675, 2015.